ABSTRACT

Title of Dissertation: ULTRA-FAST OPTICAL SIGNAL PROCESSING FOR DIGITAL COMMUNICATIONS USING ALL-OPTICAL NONLINEAR INTERACTIONS IN SEMICONDUCTOR OPTICAL WAVEGUIDES

Ehab S. Awad, Doctor of Philosophy, 2003

Dissertation directed by: Professor Julius Goldhar

Department of Electrical and Computer Engineering

In optical communications, clock recovery, optical time demultiplexing, and 3R regeneration are known as optical signal processing. Ultra-fast optical signal processing techniques are mandatory in future high-speed network and transmission systems to allow effective use of the large optical fiber bandwidth and the light speed capabilities.

One solution is all-optical signal processing that avoids the bottleneck of slow electronics. All-optical modulation can be achieved through nonlinearties in semiconductor waveguides like EAM or SOA. Those waveguides have fast and strong nonlinearties that are appropriate for ultra-fast processing. In addition, semiconductors require reasonable optical power to operate and they can be integrated with other semiconductor devices.

In this work, we demonstrated a several new techniques for optical signal processing, such as ultrafast optical clock recovery. We use the fast and nonlinear time-dependent loss/gain saturation in EAM/SOA to perform all-optical timing extraction.

This in turn is used for optical clock recovery from data rates up to 160 Gbit/s. Simulation results shows that the technique has a potential to recover optical clock up to 640 Gbit/s.

Also we demonstrated all-optical logic AND gate using nonlinear transmission of EAM. The gate shows successful operation at 10 Gbit/s with a 2^{31} -1 PRBS data and it has potential for higher speeds.

We also demonstrated optical time division demultiplexing from 40 Gbit/s with simultaneous clock recovery using cross-absorption saturation inside a single EAM. The system shows an error free operation using a 2^{31}-1 PRBS. Also, it shows successful operation with burst-mode data propagating in a fiber-optic recirculating loop up to a distance of 10,000 Km.

The optical 3R regeneration is also demonstrated at 10 Gbit/s using a single EAM. The all-optical timing extraction inside EAM is used for retiming, while the nonlinear transmission of EAM is used for reshaping. Meanwhile, wavelength conversion and re-amplification are performed at the same time.

FWM is well known by its ultrafast operation and has been widely investigated by other groups in SOA's and optical fibers. Here, we showed that FWM in EAM has unique characteristics, like wide detuning range and enhancement of conversion efficiency with reverse bias. Also, we demonstrated FWM demultiplexing from 80 Gbit/s with simultaneous clock recovery using co-propagation inside a single EAM.

ULTRA-FAST OPTICAL SIGNAL PROCESSING FOR DIGITAL COMMUNICATIONS USING ALL-OPTICAL NONLINEAR INTERACTIONS IN SEMICONDUCTOR OPTICAL WAVEGUIDES

By

Ehab S. Awad

Dissertation submitted to the Faculty of the Graduate School of the
University of Maryland, College Park in partial fulfillment
of the requirements for the degree of
Doctor of Philosophy
2003

Advisory Committee:

Professor Julius Goldhar, Chair
Professor Amr Baz
Dr. Pak S. Cho
Professor Ping T. Ho
Professor Chi H. Lee
Professor Thomas E. Murphy

DEDICATIONS

To my mother, father, and brothers

ACKNOWLEDGEMENTS

First of all I would like to thank Professor Julius Goldhar for his supervision, inspiration, and guidence throughout all of this work. Also, I thank him for his valuable advices, support, and encouragement.

Special thanks to Pak Cho who helped me in this work. I would like to thank him also for his participation and valuable comments in writing of this dissertation and the published papers.

Also, special thanks to Norman moulton, Chris Richrdson, Paul Petruzzi Shuo-Yen Tseng, Gary Carter, Marshal Sylors, Warren Herman, Chi Lee, Ping-Tong Ho, Kenneth Ritter, Hirsch Mandelberg, Amr Baz, Thomas Murphy, Anthony Lenihan, Gaston Tudury, Victor Yun, Leng Yongzhang, Rohit Grover, Priya Amkhedkar, Jonah Pezeshki, Younggu Kim, Tarek Ibrahim, and Kuldeep Amarnath.

I would like also to thank all the people in the Laboratory for Physical Sciences (LPS). Special thanks to Bernadette Preston, Paul Boudreaux, and Michael Prin. In addition, I would like to thank all the people in the Electrical and Computer Engineering Department at University of Maryland College Park.

TABLE OF CONTENTS

LIST OF FIGURES

LIST OF ABBREVIATIONS

Below is a list of abbreviations used in this dissertation:

3R:	Re-amplification, re-timing, re-shaping
Amp:	Electrical amplifier
ASE:	Amplified spontaneous emission
BER:	Bit-error-ratio
BPF:	Band pass filter
CW:	Continuous wave
DC:	Direct current
E-O:	Electro-optic
EAM:	Electro-absorption modulator
EDFA:	Erbium-doped fiber amplifier
EOM:	Electro-optic intensity modulator
FM:	Frequency modulation
FWHM:	Full-width half-maximum
FWM:	Four-wave mixing
LPF:	Low pass filter
MZI:	Mach-Zehnder interferometer
NOLM:	Nonlinear optical loop mirror
OSA:	Optical spectrum analyzer
OSNR:	Optical signal to noise ratio

OTDM:	Optical time division multiplexing
PG:	Pulse generator
PLL:	Phase-locked loop
PRBS:	Pseudo-random binary sequence
Q:	Quality factor
RB:	Resolution bandwidth
RF:	Radio frequency
R.M.S:	Root mean square
RZ:	Return-to-zero
S:	Slope of error signal
SLALOM:	Semiconductor laser amplifier in loop mirror
SOA:	Semiconductor optical amplifier
VCO:	Voltage-controlled oscillator
XPM:	Cross-phase modulation

Chapter 1

Introduction

In optical communications, the laser light can be used to carry information from one point to another. The optical carrier frequency in the order of few hundreds of THz can allow ultrafast data modulation rates up to hundreds of GHz. Therefore, A great interest has been developed in optical communication field in recent years, especially after the remarkable advances in the technologies of lasers, optical fibers, and semiconductor waveguides. Clock recovery, optical multiplexing, and data regeneration are essential operations in optical digital communications, and they are defined in that area, as optical signal processing. Clock recovery, for example, is one of the most important tasks at network nodes and receivers as it allows synchronous signal processing operations, which usually yield a high performance.

Transmission of data along optical fibers for long distances result in data degradation and distortion due to the optical fiber impairments such as Kerr nonlinearties and chromatic dispersion, in addition to accumulated amplified spontaneous emission (ASE) noise through cascaded optical amplifier stages. Therefore, the use of optical signal repeaters and regenerators at periodic transmission distances is desirable to re-amplify, re-shape, and re-time the transmitted data bits. This way longer transmission distances can be reached with an error free operation. Another

signal processing operation at receivers is time demultiplexing, which is mandatory for OTDM data to separate different data channels.

Currently deployed systems of signal processing use optical-electrical-optical (O-E-O) technology. In this approach, the received optical data is detected and converted into an electrical signal for electronic processing. The processed data is then converted into optical signal using electrical/optical converters in order to retransmit along optical fiber. This conversion process is limited by the speed of electronic components, which represents a bottleneck for high-speed optical processing that supposed to function at high data rates up to 160 Gbit/s or beyond. In order to overcome this bottleneck and make use of the high-speed and the wide bandwidth available in optical fiber systems, an ultra-fast and all-optical signal processing techniques have to be developed [1].

1.1. Review of literature on optical clock recovery

As mentioned earlier, one of the most important operations in optical signal processing systems is optical clock recovery, especially in OTDM systems [2]. Clock recovery allows synchronous operation and thus high quality for the processed signals. A recovered clock with a very low timing jitter < 1ps is required to achieve high speed operations. In phase-locked loop (PLL) circuits [3], which are the conventional approaches for the clock recovery, the operational speed and performance of the

electronic circuits are usually limited by the speed of phase comparators (mixers). Therefore, the development of phase comparators based on photonic technologies may allow these PLL systems to accommodate the high-speed optical communication systems [2].

Several techniques have been already reported in literature for optical clock recovery. For example, clock recovery has been demonstrated up to 80 Gbit/s using electronic RF mixer in electrical PLL configuration [4]. In this technique, the received data is usually detected using a high-speed photo-detector and then mixed using a microwave mixer to extract the fundamental carrier frequency. The recovered clock is a sub-harmonic at 10 GHz. Fig. 1.1 shows the experimental setup. The input data is detected by a high-speed photo-detector with a 12 GHz bandwidth. An RF mixer (8-12 GHz) is then used to mix this signal with the RF output signal (10GHz) of the VCO. The recovered clock timing jitter is < 300 fs, and the system is polarization insensitive. This technique is limited by the speed of the electronic mixer and the requirements of using high-speed multipliers to extract clock at higher bit rates.

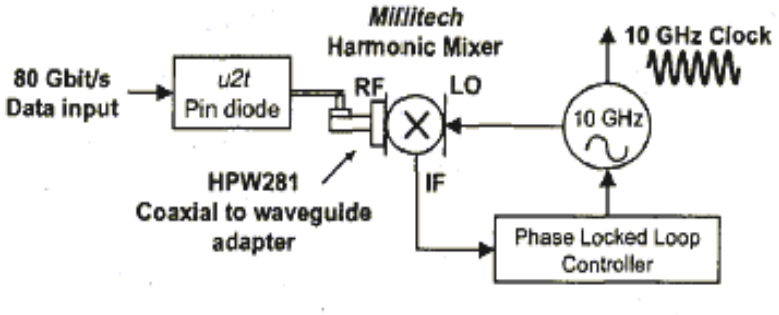

Fig. 1.1: Optical clock recovery using electronic PLL [4].

Another example of clock recovery is based on semiconductor laser amplifier in loop mirror (SLALOM). Fig. 1.2 represents the SLALOM and the clock recovery configuration [5]. The SOA is placed at an offset position from the mid-point of the loop mirror. The input data is split equally in two arms of the fiber loop, each propagates for the same distance and then interferes constructively or destructively when they combine again at the coupler. When a control pulse is injected into one side of the loop, it travels with one of the data arms and saturates the SOA causing changes in its refractive index which in turns impose a 'π' relative phase shift between the two counter-propagating data. Thus, the interference becomes constructive when the two pulses combines again.

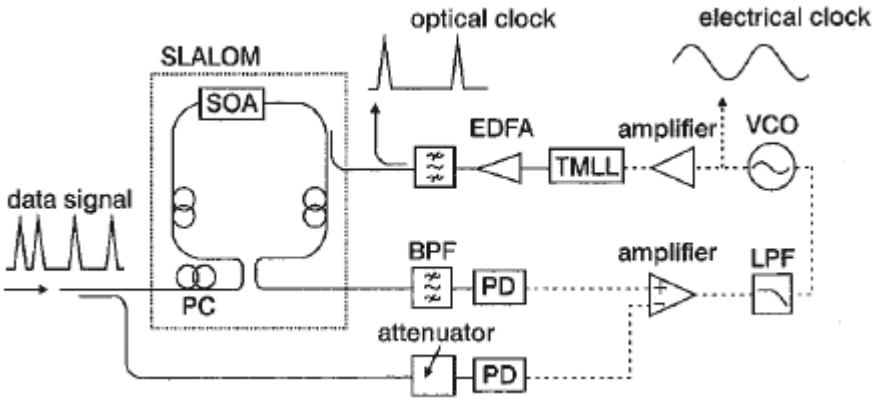

Fig. 1.2: Optical clock recovery using SLALOM. TMLL: Tunable mode-locked laser [5].

In this technique, the data is running at 160 Gbit/s and the clock at 10 GHz. A phase locked loop is used to extract the optical clock. The repetition rate of the tunable mode-locked laser is controlled using a voltage-controlled oscillator (VCO). The output signal of the SLALOM is detected by a photo-detector to produce an electrical signal. This signal controls the repetition rate of the VCO.

The photo-detected output error signal from SLALOM has a single polarity. To introduce additional polarity to this signal, the input data is detected by another slow photo-detector and subtracted electrically from the error signal. The switching window of the SLALOM in this case is about 11 ps. The calculated timing jitter from the recovered clock RF spectrum is < 300 fs.

RF driven electro-absorption modulator (EAM) has been also used for clock recovery [6]. Two EAMs are used to recover the clock from 160 Gbit/s. The EAMs are used in conjunction with an electronic mixer to form a PLL. Fig. 1.3 shows the experimental setup. The first EAM is driven by a 20 GHz RF signal and the second one by a 10 GHz signal.

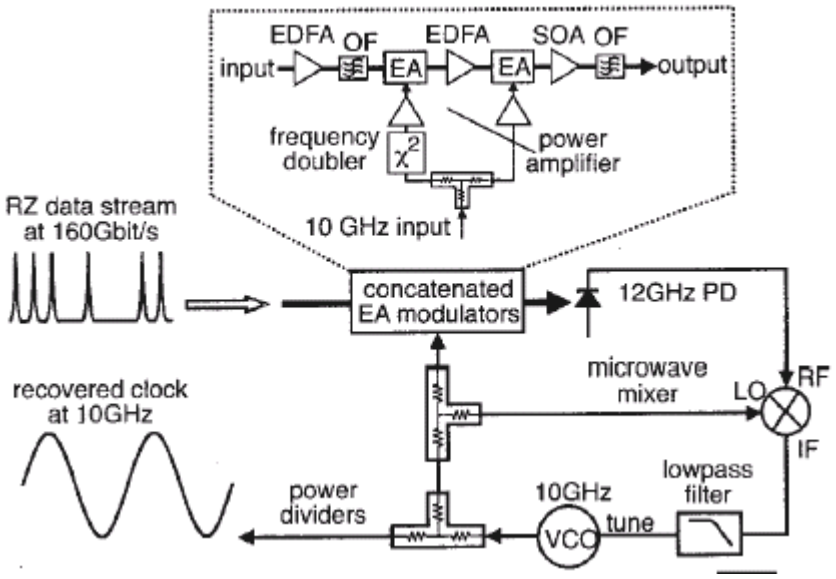

Fig. 1.3: Optical clock recovery using RF-driven EAM [6].

Another clock recovery technique uses a high-Q electronic filter [7]. In this technique the input data is detected by a large bandwidth photo-diode and the RF signal is passed through a high-Q bandwidth filter (Q =1800). The filter extracts the

fundamental base rate of the data signal, which is the recovered clock. Fig. 1.4 shows the set-up for clock recovery. The root mean square (r.m.s) timing jitter is < 600 ps.

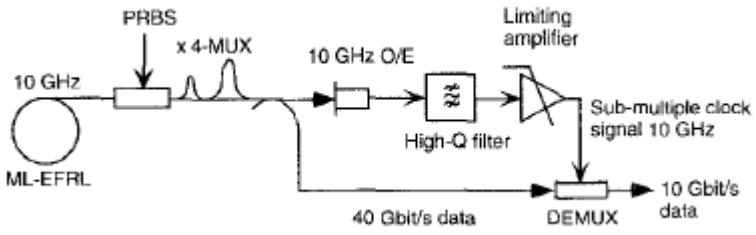

Fig. 1.4: Optical clock recovery using a high-Q filter [7].

Another example of clock recovery is based on optical tank circuits, which utilize a Fabry-Perot interferometer as a tank circuit to extract the fundamental clock frequency component from the received data. However, such techniques can only extract the clock frequency for a fixed data rate, for which the optical tank circuit is designed [8].

Alternatively, injection locking has been used for clock recovery by utilizing specially designed lasers such as self-pulsating distributed feed back laser. The setup is shown in Fig. 1.5. This technique is all-optical and reasonably fast (up to 40Gbit/s), although the bit rate should be very close to the laser self-pulsating frequency in order to achieve locking and get a reasonably low timing jitter for the recovered clock. In addition, self-pulsating lasers are complex to fabricate and requires careful control of the operating parameters [9].

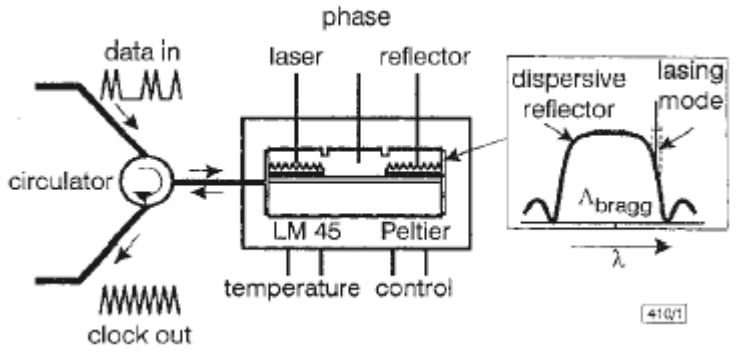

Fig. 1.5: Clock recovery by injection locking into self-pulsating distributed feed back laser [9].

Another method is injection locking in a fiber mode-locked laser. The fiber laser uses a semiconductor optical amplifier (SOA) as the gain medium [10]. Optical data at 40 Gbit/s is injected into the laser to modulate the gain and refractive index of the SOA, so that the lasing mode can be adaptively tuned to lock onto the timing of the input data. The laser output is a sub-harmonic recovered clock at 20 Gbit/s. In order to reduce the pattern effect of the SOA, a comb-like Fabry-Perot optical filter is used to generate a sequence of pulses from the incoming data sequence in place of zeros before injecting into the laser, as shown in Fig. 1.6. The free spectral range of the filter is equal to the data bit rate.

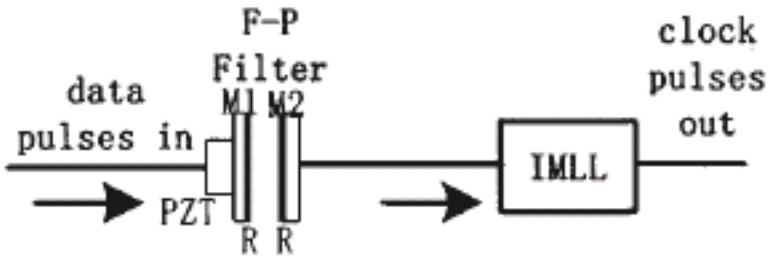

Fig. 1.6: Optical clock recovery using injection locking in a fiber mode locked laser [10].

1.2. Review of literature on optical demultiplexing and 3R regeneration

Optical time demultiplexing is another important signal processing operation. It has been reported using several techniques, For example, nonlinear optical loop mirror (NOLM) and Cross-phase modulation (XPM) using the Kerr effect in optical fibers. In NOLM, the demultiplexing is based on the induced phase shift of the optical pulses in the fiber loop interferometer. It utilizes interference between two counter-propagating light pulses along several kilometers of fiber [11]. Also, XPM in SOA's is used in fiber loop mirrors in a configuration known as SLALOM [12], which overcome the problem of using long fibers in NOLM's because SOAs have a strong nonlinearity that introduce sufficient amount of XPM.

Optical demultiplexing from 80 Gbit/s using Mach-Zehnder interferometer (MZI) with SOA's has been demonstrated in [13]. The technique depends on the SOA

refractive index modulation in the two arms of the MZI by using differential control pulses. Fig. 1.7 shows the setup configuration.

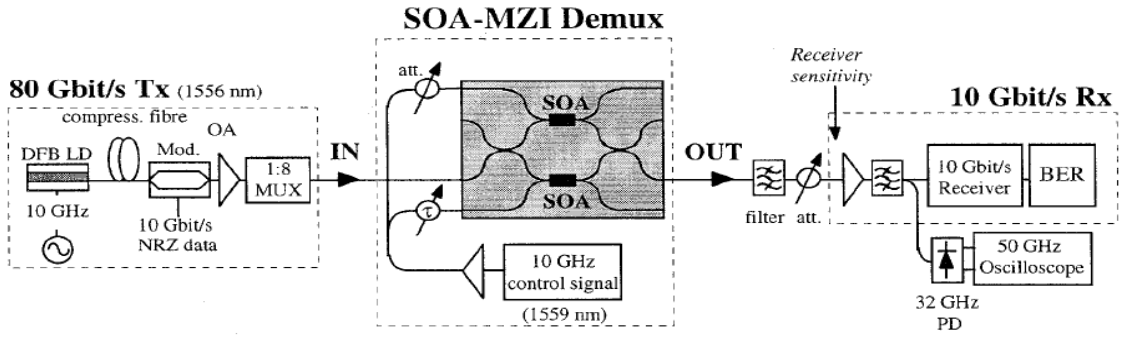

Fig. 1.7: Experimental setup for 80 Gbit/s demultiplexing using SOA-MZI [13].

Also, demultiplexing from 80 Gbit/s has been demonstrated using cross-absorption modulation in EAM with a short switching window [14]. In addition, error-free demultiplexing from 160 Gbit/s to 40 Gbit/s has been demonstrated using four-wave mixing (FWM) in SOA [15]. Fig. 1.8 shows the experimental setup for FWM demultiplexing using SOA. More discussion about FWM in EAMs and SOAs will be presented in chapter 6.

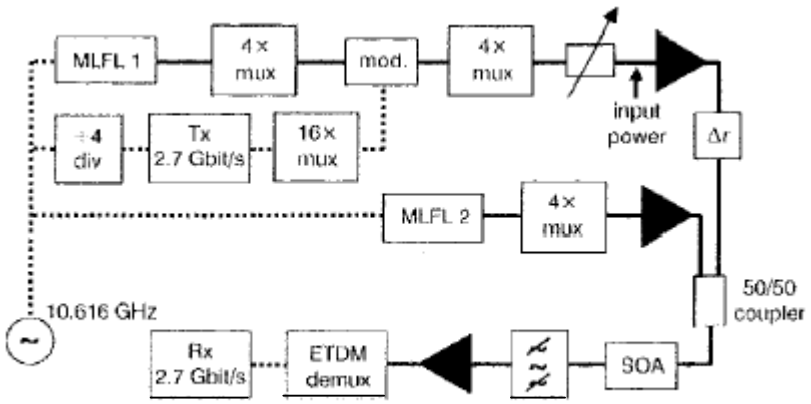

Fig. 1.8: Experimental setup for 160 Gbit/s demultiplexing using FWM in SOA [15].

Optical 3R regeneration has been also reported using different techniques. 3R is an abbreviation for re-amplification, re-shaping, and re-timing. The most common techniques for 3R regeneration are performed using EAMs. The nonlinear transmission of the EAM reshapes the degraded input data by selective absorption of the optical noise. Therefore, increasing the optical signal to noise ratio (OSNR) of the output. The EAM has been used to perform 2R regeneration in [16]. The high absorption at low pump power suppresses noise on zeros. Fig. 1.9 shows the experimental setup.

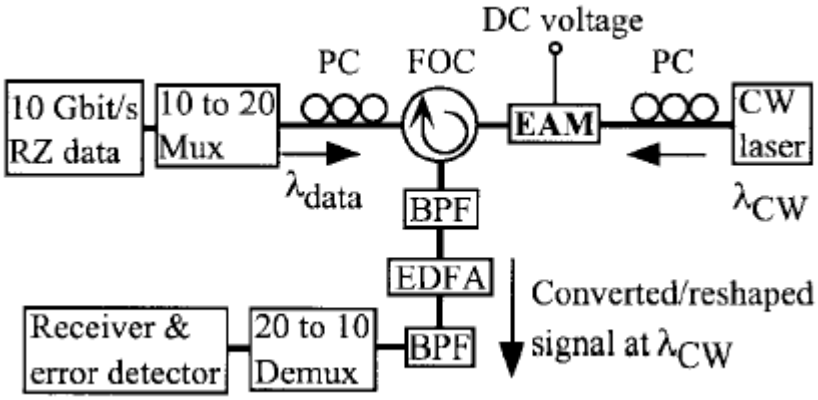

Fig. 1.9: Setup for 2R regeneration at 20 Gbit/s [16].

In addition optical 3R regeneration has been demonstrated at 40 Gbit/s by using three electro-absorption modulators, in a cascaded configuration, with an electrical clock recovery circuit and two wavelength conversion stages [17]. One of these modulators is used for data re-shaping, while another is used in conjunction with the electronic clock recovery circuit to generate the appropriate optical clock pulses, Fig. 1.10.

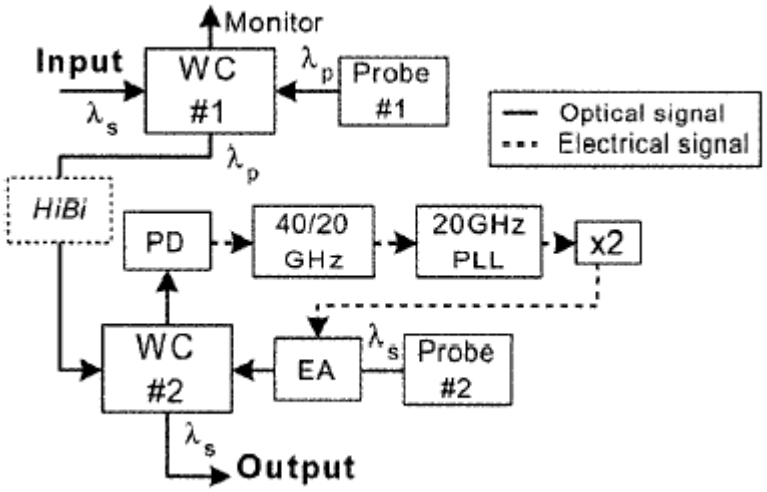

Fig. 1.10: Experimental setup for 40 Gbit/s 3R regeneration using EAM's [17].

Another technique for optical 3R regeneration has been demonstrated using MZI with SOA's in [18]. In this technique two stage of SOA-MZI are used in conjunction with electronic clock recovery, Fig. 1.11. The technique uses cross-phase modulation in SOAs and the nonlinear characteristic in MZI to regenerate the input signal.

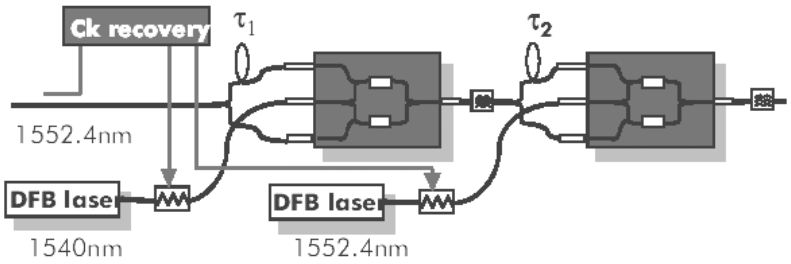

Fig. 1.11: Optical 3R regeneration using SOA-MZI [18].

1.3. Motivation and statement of the problem

As mentioned earlier, ultra-fast signal processing is essential for high-speed optical networks and optical digital communications. All-optical techniques using semiconductor devices are the key solutions for achieving such high speeds. Also, combining two or more signal processing operations in a single semiconductor device is another goal. We choose semiconductor optical waveguides because of their high nonlinearties and operational speed. In addition, they can be integrated with other semiconductor components, thus reducing footprint, cost and power consumption.

In this dissertation, EAM and SOA were used to perform high-speed signal processing operations. The focus will be on the EAM because it has a faster response than SOA and it allows combining different signal processing operations using the same device. The nonlinearties of SOA are also presented in some experiments for the purpose of comparison with EAM performance and verifying the generality of the developed signal processing techniques.

In the following chapters, experimental and modeling results for the developed signal processing techniques are presented. In chapter 2, nonlinear optical semiconductor waveguides such as EAM and SOA, and the all-optical cross absorption or gain modulation in such waveguides will be discussed. In chapter 3, we show how EAM can be used as an all-optical logic AND gate which can have different applications in optical communications such as switching and routing. In chapter 4, we

discuss the all-optical timing extraction process in nonlinear semiconductor waveguides using a new technique. We demonstrate optical clock recovery up to 160 Gbit/s using EAM and verify the technique operation using SOA. Also, a simulation model for the optical clock recovery system is presented. Using this model, feasibility of clock recovery up to 640 Gbit/s is demonstrated.

In chapter 5, we demonstrate other signal processing techniques: optical demultiplexing and 3R regeneration. The optical demultiplexing is performed simultaneously with clock recovery in a synchronous operation. The system utilizes a single EAM to demultiplex 40 Gbit/s input data into 10 Gbit/s with a 10 GHz recovered clock and an error-free operation. In 3R regeneration, we demonstrate re-shaping, re-timing, and re-amplification of degraded input data at 10 Gbit/s. The system recovers the optical clock simultaneously at 10 GHz, and shows negative power penalty for the regenerated data.

In chapter 6, we investigate FWM in EAM and the enhancement of FWM efficiency with reverse bias. We also demonstrate demultiplexing by FWM in EAM with simultaneous clock recovery at 80 Gbit/s. In this clock recovery scheme we use co-propagation between the data and clock pulses instead of the counter propagation that was used in the previous experiments.

In chapter 7, we discuss different signal processing techniques that we have

presented in this dissertation and possible future work. Appendix A contains the simulation model for optical clock recovery system, and appendix B contains a discussion of the timing jitter measurements.

Chapter 2

Nonlinear optical semiconductor waveguides

In this chapter we will discuss all-optical cross gain and absorption modulation in nonlinear optical semiconductor waveguides. All-optical cross-modulation refers to the process in which light modulates light. Semiconductor waveguide materials have optical properties (e.g. gain or absorption) that depend on the optical power. Examples of the nonlinear semiconductor waveguides are EAMs and SOAs. The SOAs have been extensively characterized and discussed by our group in previous dissertations work [19][20]. Furthermore, the commercial SOA utilized here have been completely characterized as an optical amplifier in [21]. In this dissertation our emphasis will be on EAM and its applications in fast optical signal processing.

The conventional application of EAM is RF-optical amplitude modulation, in which the RF power across the EAM electrodes modulates the light power propagating through its waveguide. Usually the EAM is reverse biased with a direct current (DC) voltage, which increases the optical absorption coefficient inside its waveguide as a result of the Franz-Keldysh effect or quantum confined Stark effect in quantum well. Applying the RF power in addition to the DC bias alters the absorption coefficient inside the waveguide as it modulates the voltage across the device electrodes. Different applications such as optical pulse generation and demultiplexing have been reported using this electro-optic (E-O) technique in EAM [22][23][24]. Also, the EAM can be

used to perform all-optical modulation based on the following mechanism. Under DC bias, when an optical pulse with a sufficient peak power travels along the EAM waveguide, it gets absorbed and generates electron-hole pairs inside the wave-guide. These carriers induce screening to the applied electric field [25] as they drift towards the electrodes under the influence of the applied electric field. The screening of the reverse electric field reduces the local electric field, which in turn reduces the optical absorption inside the wave-guide [26]. Thus, a probe optical signal (CW or pulses) going through the wave-guide will experience an increase in transmission. The device basically acts as a fast optical controlled saturable absorber. Different applications for signal processing using all-optical modulation techniques inside EAM have been reported [14][16][17][27].

The EAM utilized in this dissertation is a commercial device from JAE Company in Japan. It is a good commercial device. Fig. 2.1 shows a typical structure of that EAM. It is an InGaAsP based device with multiple quantum wells designed for operation near 1550 nm. The waveguide is ≈ 200 μm long. The packaged device is fiber pigtailed with a built-in thermal electric cooler for temperature control. The detailed structure is similar to that described in [22]. The EAM has a zero-bias fiber-to-fiber insertion loss of ≈ 10 dB at 1555 nm, and a polarization dependent loss of less than 1 dB. The 3 dB RF-bandwidth (electrical-to-optical bandwidth) of the EAM is about 13 GHz.

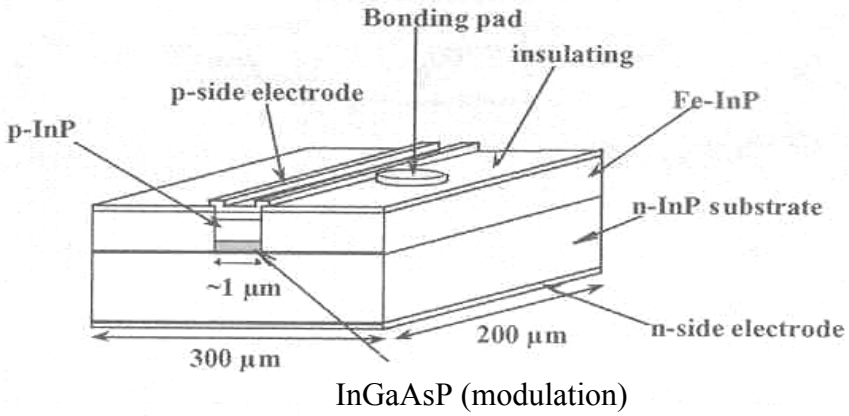

Fig. 2.1: The EAM structure.

We performed the following measurement to characterize the EAM device. The measured back reflection from the device is – 43 dB, which indicates a very small reflection from the device facet to the input optical signal. The optical absorption of the device increases with higher reverse bias as the absorption edge shift towards longer wavelength or lower optical frequencies. For example, the transmission of the EAM can varies from – 6 dB to – 45 dB with a change in reverse bias from 0 to – 6 volts at 1550 nm. The absorption is also wavelength dependent. Fig. 2.2 shows the measured transmission through the EAM as a function of wavelength at different reverse bias voltages using an ASE noise source (optical amplifier) as an input probe signal. The

reverse bias shifts the absorption or bandgap edge to a longer wavelength and thus reduces the EAM transmission.

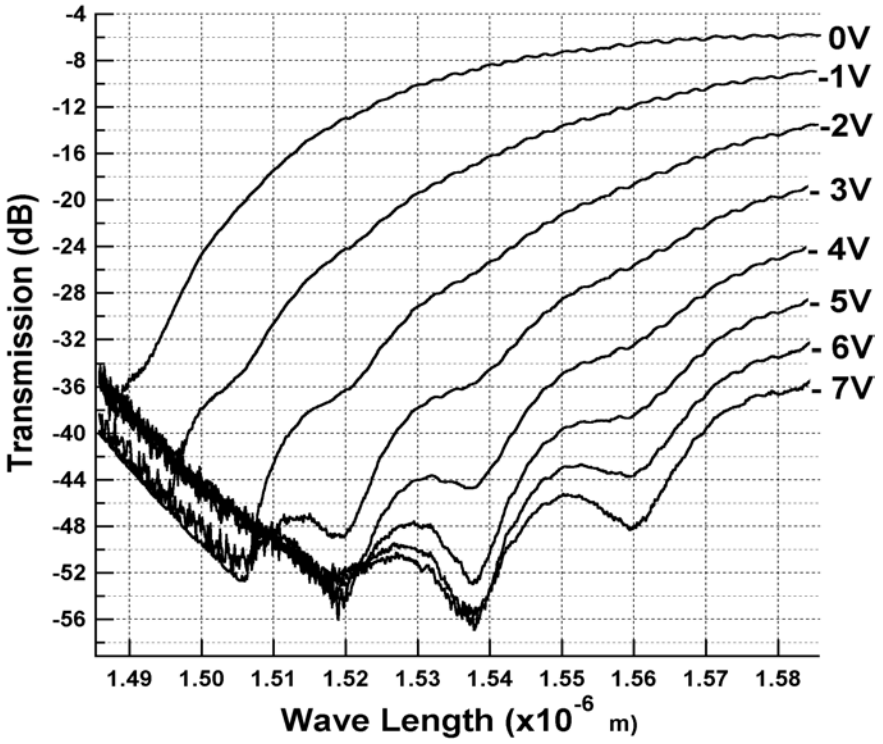

Fig. 2.2: The measured transmission of the EAM versus wavelength at different reverse bias voltages using an ASE source as an input signal.

Fig. 2.3 shows the transmitted peak powers as a function of the input pump powers at different reverse biases. In this measurement, the operating wavelength is 1545 nm and the repetition rate of the pump pulse is 1 GHz with a 3.3 ps pulse width. The transmission is a nonlinear function of the input pulse (pump) power. In other

words the transmission is a function of the optical pulse energy, which corresponds to the pump average power. For example, the 0dBm (1 mW) input average power corresponds to 1 pJ (1 mW/1 GHz) of energy per pulse. The pump can cross modulate the probe signal and thus any data (amplitude information) on the pump pulses can be transcribed onto the probe signal.

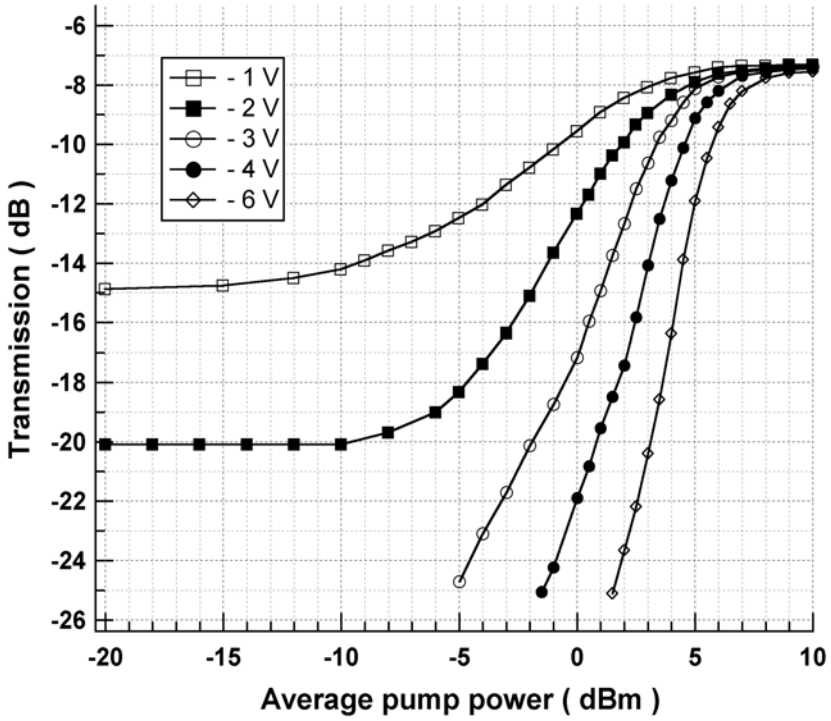

Fig. 2.3: The measured nonlinear transmission of EAM using pump-probe technique. The repetition rate is 1 GHz and the pulse width is 3.3 ps.

The transmission of EAM has a nonlinear dependence on the input optical pump power. Fig. 2.4, curve (a), shows the probe pulse transmission as a function of time, after arrival of the pump pulse inside the EAM wave-guide. A fast increase (≈10 ps) in the transmission occurs, followed by a slow recovery time that depends on the carrier sweep-out dynamics inside the wave-guide [26]. As can be seen from curve (a), the transmission window is estimated to be 25 ps measured at the full-width half-maximum (FWHM). We observed that the recovery time depends on the pump pulse energy. For example, reducing the pump power results in a reduction of the recovery time and the transmission window width, as shown in Fig. 2.4, traces (a,c-f).

We also observed that the transmission is function of the relative arrival time between the counter-propagating input pulses. Fig. 2.4 shows the response time of the EAM as a function of the delay between the counter-propagating pulses inside EAM. It is measured by monitoring the output peak power of a probe signal while varying the optical delay of one of the input pulse trains. Curve (a) corresponds to the transmitted probe at 10 pJ of total input pulse energy and curve (b) corresponds to the counter-propagating case at the same energy. Note that the optimal timing (for maximum peak power) is different for the two directions. For the maximum transmitted power in one direction, the other pulse must arrive at the EAM earlier (≈ 7.5 ps) and experience higher absorption.

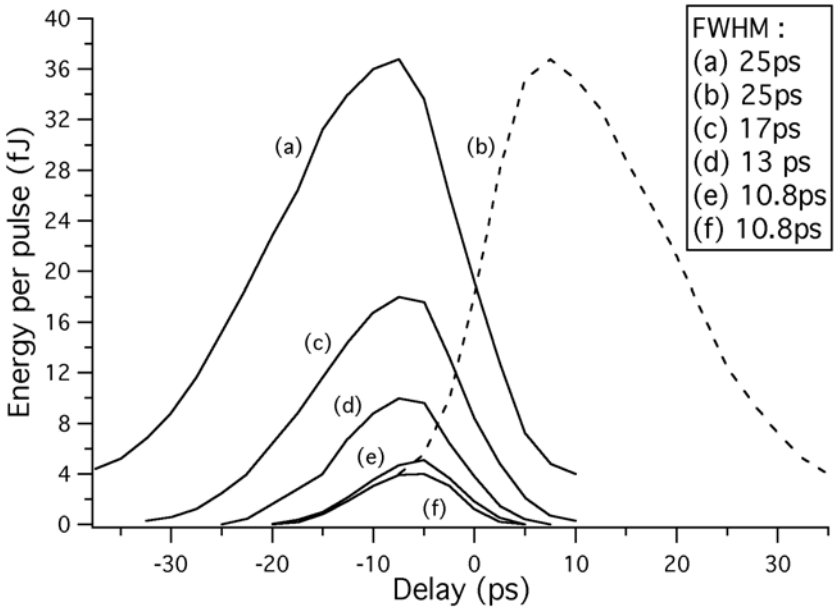

Fig. 2.4: Output peak power vs. the delay between the two counter-propagating pulse trains; one input is fixed at 5pJ (energy per pulse). The other input has pulse energy: (a) 5pJ, (b) 5pJ - output is taken from transmitted counter-propagating pulses, (c) 2.5pJ, (d) 1.6pJ, (e) 1pJ, (f) 0.8pJ. The data was taken using 45GHz detector and 50 GHz oscilloscope.

The separation between the two peaks corresponds to the time it takes to reach the maximum transmission and it is due to the transit time (~5ps) across the device and the time required for screening of the electric field [25]. The closing of the transmission window is due to carrier sweep-out dynamics [26].

The measured FWHM of switching transmission window for case (a) in Fig. 2.4 was 25 ps. We could reduce the duration of the switching window for the pulses down to ~10 ps, by lowering the energy of one of the input pulse train, as can be seen in traces (c-f).

Fig. 2.5 shows the measured FWHM for the EAM switching window under different reverse bias voltages and input pump powers, using pump-probe technique at 1GHz repetition rate. Under appropriate pump power and reverse bias, the transmission window can be less than 25ps, which is suitable for signal processing at 40Gbit/s.

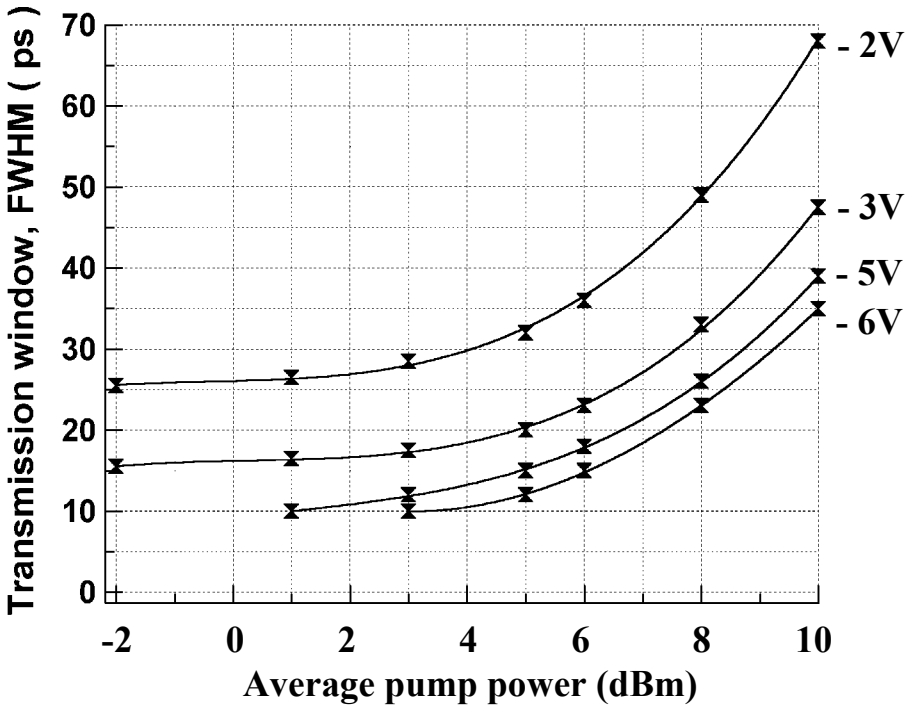

Fig. 2.5: The measured FWHM of switching window at different input average powers and reverse biases. Measurements are made at 1GHz, 1545nm, using a 3.3 ps pulse width.

Chapter 3

High-speed all-optical AND gate using nonlinear transmission of Electro-Absorption Modulator

The logical operation 'AND' has applications in optical communications for routing and switching. We investigate an all-optical logic AND operation at 10 Gbit/s using nonlinear transmission of electro-absorption modulator pumped with two counter-propagating data streams. The transmitted pump itself was used as the output of the optical gate to obtain high extinction ratio, and high output peak powers. The gate has been tested using a 2^{31}-1 long pseudo-random binary sequence (PRBS). The logical output of the gate has an extinction ratio of more than 10dB with good eye opening. Our measurements of the gate transmission window show that all-optical logic operation up to 100Gb/s is feasible.

Recently, significant number of experiments was reported on high bit rate all-optical signal processing using electro-absorption modulators [28][29][30]. For example, wavelength converter and regenerator based on the EAM have been demonstrated up to 40 Gbit/s [29]. Typically, a weak CW input signal is used to probe the modulated transmission of EAM, which is induced by intense input pulses [16], however the high residual absorption in EAM results in a very weak output. In this chapter, we investigate bit-wise logical AND operation using the EAM with input optical pulses. We injected two input data streams into the EAM in a counter-

propagating configuration. We found that with proper timing between the two counter-propagating input data pulses, either one of the stream can be used as the output with performance significantly better than that with the CW probe only. The output of the AND gate shows an error-free operation at 10Gb/s with a clear eye opening. The measured transmission window time can be reduced down to ~10 ps by attenuating the input power in one of the pulse streams, so that operation at 100Gb/s is feasible for such a gate.

Fig. 3.1 shows the experimental setup used to test the AND gate operation. Pump pulses were generated at a repetition rate of 10GHz by a semiconductor hybrid mode-locked laser operating at 1544.6 nm. The laser pulse duration, after two 1.5-nm band-pass filters, was ~ 3ps. The mode locked pulse train is modulated by using a Mach-Zehnder $LiNbO_3$ electro-optic intensity modulator (EOM) driven by a bit pattern pulse generator (PG), to obtain the desired sequences of data pulses. After amplification in an erbium-doped fiber amplifier (EDFA), the data pulses were divided by a 50/50 fiber coupler into two counter propagating data channels and injected into the two ports of the EAM. Relative delay between the two input data streams was adjusted with a variable optical delay line. Output pulses from one of the modulator arms was split off by a 20-80 coupler and used as the output of the AND gate.

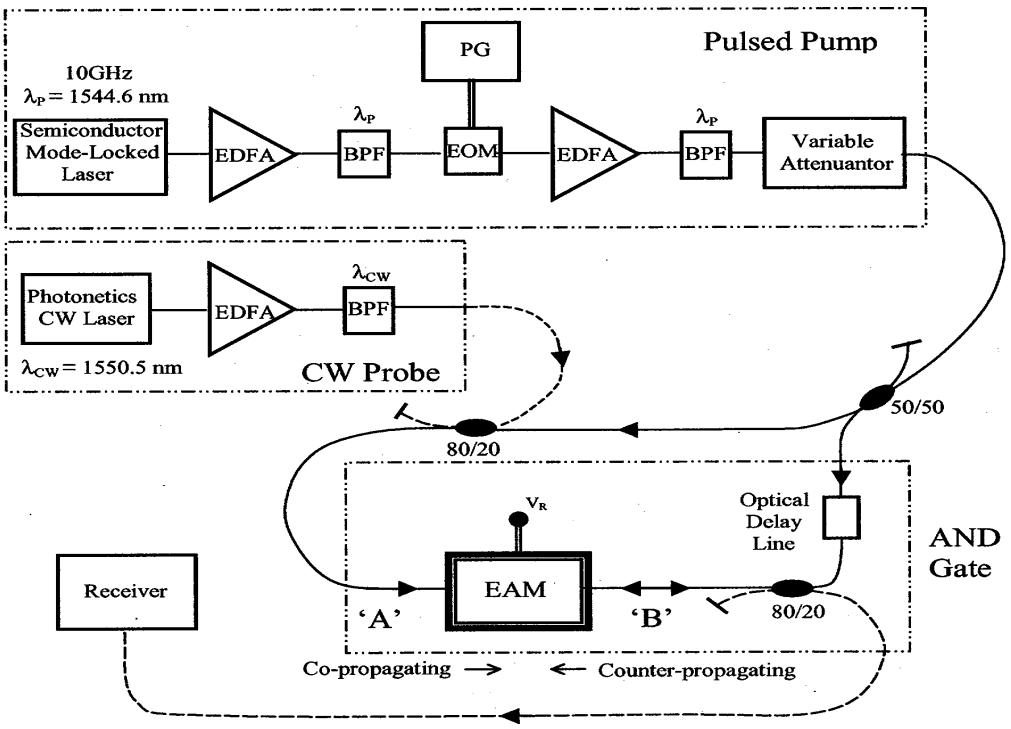

Fig. 3.1: Experimental setup for optical logical AND gate using the EAM in a counter propagation configuration. PG: Pulse generator, EOM: Mach-Zehnder Electro-optic Modulator, BPF: Band Pass Filter

A CW signal (probe) was used to monitor and characterize the EAM transmission with each pump channel separately, and together during the AND gate operation. After the EAM, the probe signal at λ_{CW} was separated from the pump signals using a band pass filter (BPF). The probe signal was then amplified in an EDFA and filtered by another BPF to reduce the ASE from the EDFA. Counter-propagation of pump pulses reduces the possibility of device damage as compared to injection of full

optical power from one side only. Also this configuration provides two separate input ports for an AND gate.

As mentioned earlier, our EAM has a zero-bias insertion loss of ~ 10 dB at 1555 nm, and a polarization dependent loss of < 1 dB. The back reflected pulses from the device were measured to be –43 dB below the input pulse. At the reverse bias of V_R equal to 6 V and temperature stabilized at 8^{o}C the small signal absorption at the pump and the probe wavelengths increases by approximately 40 dB. When a sufficiently intense pulse propagates through the EAM, photo-generated carriers screen out the electric field inside the wave-guide as the electron-hole pairs drift away from each other and hence reduces the absorption. As shown earlier in Fig. 2.3, the transmission of peak power depends on the input pump power. The relative delay of the two counter propagating pulse trains was adjusted for maximum transmission. Both pumps contribute to increase of transmission. The curves were taken for a 1GHz pump repetition rate by selecting one pulse out of every 10 pulses from a 10 GHz pulse stream to reduce the duty cycle of the pump. This was done in order to avoid undesirable thermal run-away effects that can lead to catastrophic facet damage at the highest input optical power. This can be attributed to thermal induced bandgap reduction causing more absorption, which leads to even more heat dissipation near the facet induced by the photocurrent. At 6 volts reverse bias the transmission can change by more than 26 dB at an input optical power of 7dBm.

The two pumps can be considered as the inputs to the logical AND gate, and the signal at the probe wavelength acts as the output. The probe signal is useful for characterization of the device operation, however it is very weak (< -40 dBm). In order to detect it we needed to use an EDFA to amplify the signal that also added substantial amount of ASE noise to the signal. However, we found that with an appropriate time delay, either one of the pump pulses could be used as the output of the logical gate. The advantage of this scheme is higher transmission with larger signals (EDFA and the band pass filter are not required) and therefore higher signal to noise ratio . Also, the AND gate's inputs and outputs are at the same wavelength, which is important for cascading a large number of gates. Operating at the highest peak powers we observe the variation of the output between $(1 \bullet 1)$ and $(1 \bullet 0)$ inputs was close to 10 dB. Lowering of the input power resulted in increase of the contrast ratio and decrease of the output.

The response time of the gate is shown in the previous chapter (Fig. 2.4). The transmission for case (f) is an order of magnitude lower than that of case (a). We also observed that the transmission recovery time of the strong counter-propagating pulse , trace 'b' (5pJ), did not change significantly.

The extinction ratio of the gate is defined as the ratio of the transmission at the optimal timing to that without the input counter-propagating pulse. We observed that the extinction ratio increases as the input power is reduced. The extinction ratio at 5pJ in each input was ~10dB. The extinction ratio increases up to ~15 dB for the weakest

pulses used (case f). This behavior can be attributed to the reduction in output zeros amplitude with less input power.

The operation of the AND gate was tested using a PRBS of 2^{31}-1 long at 10 Gbit/s. Fig. 3.2 shows typical patterns illustrating the AND gate operation. Traces (I) and (II) show the input sequences which were transcribed onto the CW probe with each pump channel turned on separately. Trace (III) shows the output (A•B) that was produced by the co-propagating transmitted pump (without using EDFA). The small fluctuation in the output peaks is comparable to the fluctuation of the input.

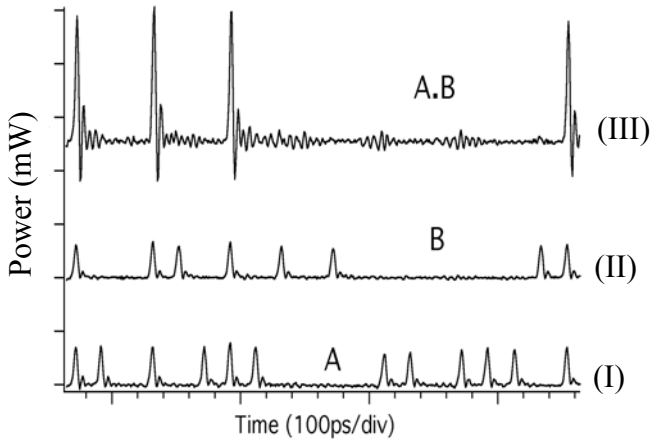

(a)

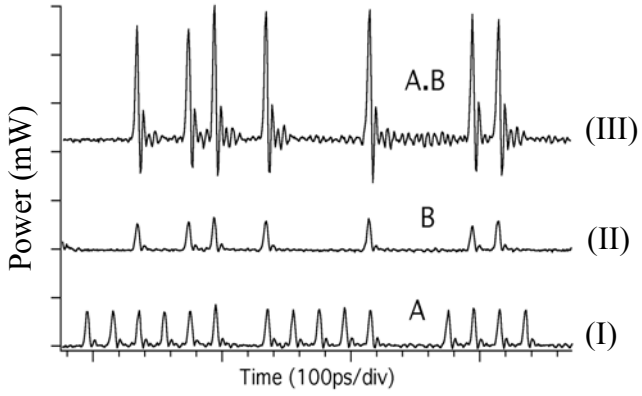

(b)

Fig. 3.2: AND gate operation at 10 GHz using PRBS for two arbitrary selected input bit sequences in figures (a) &(b). "A"& "B" are the two pump inputs transcribed by probe signal; "A•B" is the output read from the transmitted co-propagating pump pulses.

More careful comparison of the input and output signals quality can be made by observing the eye pattern in Fig. 3.3. The output has an eye opening comparable to that of the input. Also as expected, there are fewer marks than zeros as compared with the

input. This can be seen in the gray color density difference between mark and zero levels Fig. 3.3.b.

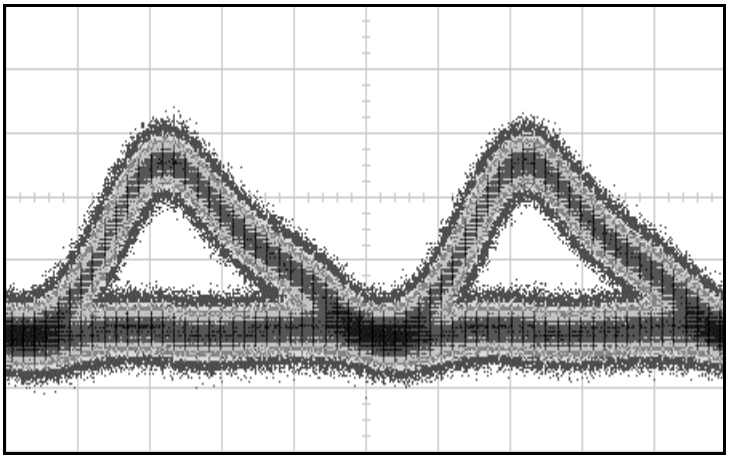

20ps /div **(a)**

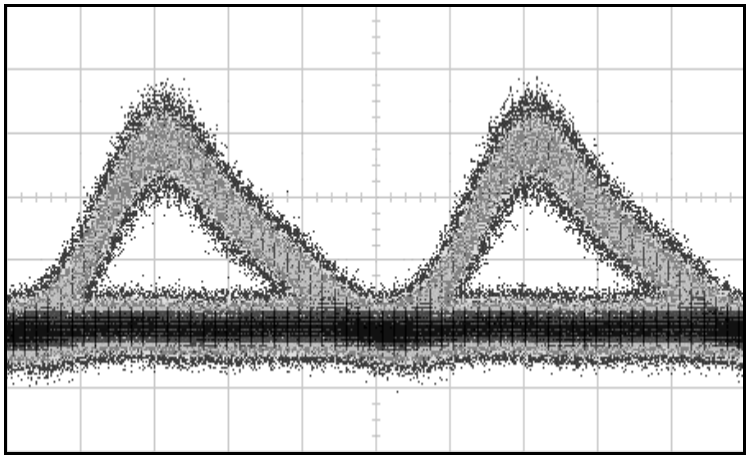

20ps /div **(b)**

Fig. 3.3: Measured eye diagrams, PRBS: 2^{31}-1, RZ data, 10GHz: (a) One of the inputs just before the EAM, (b) Output of AND gate read from the transmitted co-propagating pulses. (20GHz detector followed by an electronic low-pass filter).

In summary, we have demonstrated that the nonlinear transmission of the EAM can be used to implement a fast all-optical logic AND gate with two counter propagating data streams so that the output can be transcribed to either one of the data streams. We showed that by reducing input power in one of the data streams, the recovery time of the gate approaches 10 ps, which implies feasibility of 100Gbit/s operations. The gate inputs and output have the same wavelength that is crucial for cascading optical logic gates. However, it is also possible to use different wavelengths for the inputs. A high output contrast ratio up to 15 dB was achieved. The operation of the optical gate has less than 1dB polarization dependence. Also, it is possible to choose one of the two outputs based on the optimum delay adjustment. The required input optical power could be further reduced by utilizing the phase modulation as a result of the refractive index change associated with the absorption change in the EAM using interferometric techniques [31].

Chapter 4

All-optical timing extraction and clock recovery

In this section the technique for all optical timing extraction and clock recovery is presented. The technique is based on nonlinear all-optical cross-modulation inside semiconductor waveguides (SOA or EAM).

This technique pertains to a method and apparatus for all-optical timing extraction and optical clock recovery for high-speed return-to-zero (RZ) binary optical data streams with data rate up to 160 Gbit/s. In general, clock recovery is required at receivers to perform synchronous operations such as time-division demultiplexing and 3R optical regeneration. Transmission of data over long fiber links results in timing jitter, which is one of the major signal degradation problems. The timing jitter refers to a random variation of pulses arrival time at the receiver, and it can be in an order of magnitude of the pulse width. One example is the Gordon-Haus timing jitter in soliton propagation, which is a major limiting factor in ultra-long distance transmission. There is also a slow variation in the propagation time of the transmitted data caused by accumulative change in the fiber refractive index due to temperature variation and mechanical disturbance. The jitter may cause slight changes in the repetition rate of the data at the receiver. In packet switching systems, the arrival time of the data packets is relatively random. Therefore, at a node or a receiver the timing of the data needs to be

extracted and synchronized with a local clock that in turn drives a data processing device, which can perform other signal processing operations.

In this technique, the all-optical timing extraction determines the timing difference between two counter-propagating optical pulses using the nonlinear optical wave-guides. The extracted timing information is used in conjunction with a balanced photo-detector to generate an electrical error signal. This error signal is used in a phase-locked loop configuration to perform optical clock recovery.

4.1. Optical clock recovery using an EAM

In the following section we discuss in details the optical clock recovery technique using EAM as a nonlinear waveguide for all-optical timing extraction. All optical timing extraction in nonlinear waveguides will be presented followed by a discussion on error signal generation. In subsequent sections we will discuss the clock recovery system, its performance, and recovering the clock from a 160 Gbit/s data stream. We will then discuss the optical clock recovery operation using SOA followed by discussion on a simulation model for clock recovery in EAM and SOA.

4.1.1. All-optical timing extraction

Timing extraction is the process in which the arrival time of individual data bits is estimated and used subsequently to recover the phase and repetition rate of the optical clock. In this section we show how that can be achieved all-optically by using EAM nonlinear modulation.

Let us consider the case in which two counter-propagating pump pulses arrive at different times inside the nonlinear wave-guide. Both pulses contribute to the EAM transmission saturation. The leading pulse will saturate the absorption, which in turn effects the transmission of the following arriving counter-propagating pulse. Therefore, a pulse sees a high transmission if it is preceded directly by a sufficient intense counter-propagating pulse that allows pre-saturation to the medium absorption. Given that the nonlinear device has two possible outputs, one for each counter-propagating pulse steam, as shown in Fig. 4.1.a, a delay-dependent peak power transmission for each output as shown in Fig. 4.1.b is measured for the case of the EAM device.

Fig. 4.1.b illustrates the transmitted peak power versus the relative arrival time delay between the two counter-propagating pulses. Each of the two curves represents one output from each side of the EAM. We note that the highest transmission at one side occurs if the preceding counter-propagating pulse arrives ~7.5 ps earlier. The steep rising slopes of the curves have very short time duration in an order of few picoseconds. This short time duration shows how much delay can be

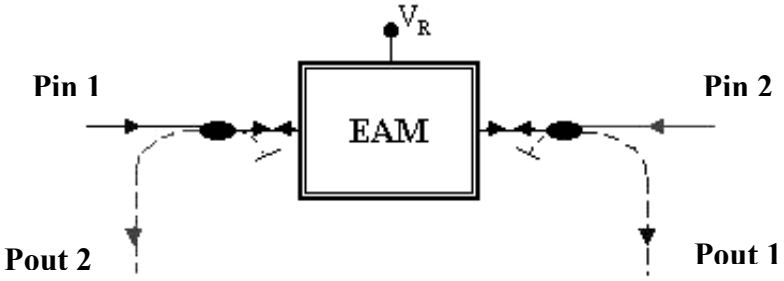

(a)

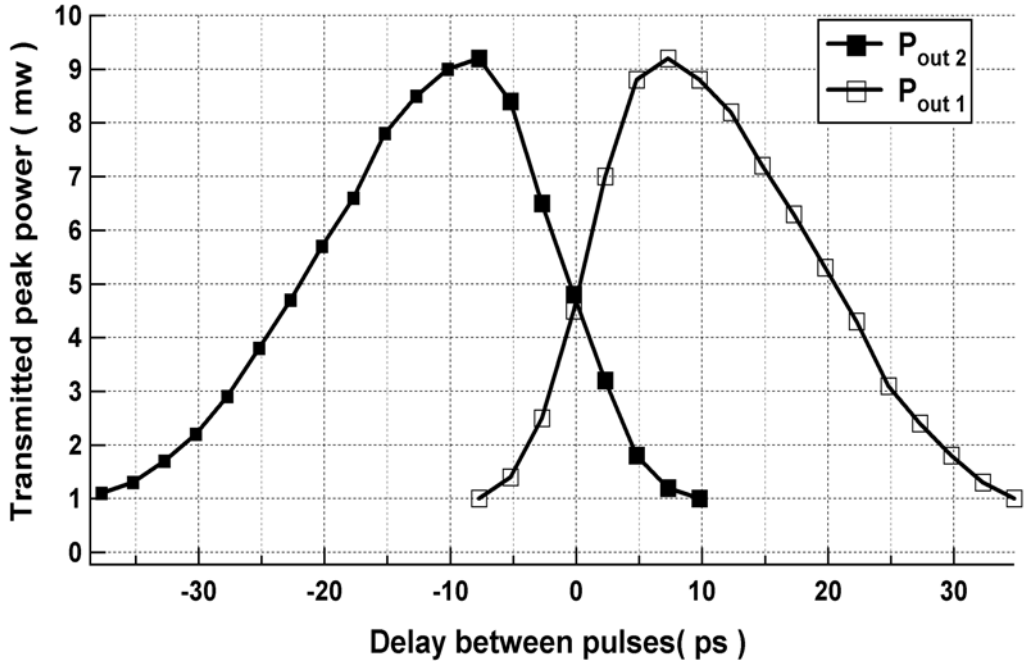

(b)

Fig. 4.1: a) Schematic configuration of all-optical timing extraction technique using counter-propagation in EAM nonlinear optical waveguide; b) The EAM measured transmitted peak power from each output as a function of timing delay between the two pulses inside the wave-guide. Zero delay corresponds to the moment at which the two pulses arrive simultaneously inside the wave-guide.

resolved between the two counter-propagating pulses using this technique. Therefore, these two curves provide timing information about the two counter-propagating pulse streams.

Based on this principle, two optical beams with the same or different wavelengths or polarizations are launched simultaneously into a fiber-pigtailed EAM in a counter-propagating configuration. Each of the two counter-propagating streams can be considered as a pump and a probe at the same time. The first beam (referred to as data) is a pulse train encoded with binary digital information using amplitude shift keying. The second beam (referred to as clock) is a stable pulse train produced by an optical pulse source with a repetition frequency close to that of the data and has a relatively low timing jitter. The amount of transmission change, however, depends on the relative delay between the data and clock signals inside the device. Therefore, the transmitted power of the data and clock signal depends critically on the relative arrival timing of the two pulses inside the wave-guide.

4.1.2. Error signal generation

In principle, the error signal provides complete information on the timing error between the data and clock pulses. This timing error can be compensated by proper tuning of the repetition frequency and phase of the optical pulse source. Here, we generate the error signal by using a balanced photo-detector, shown in Fig. 4.2.a. The

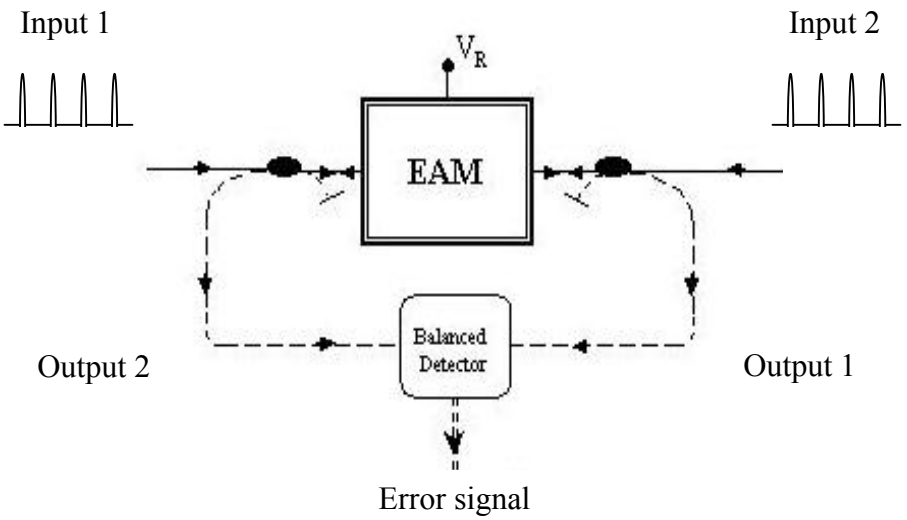

(a)

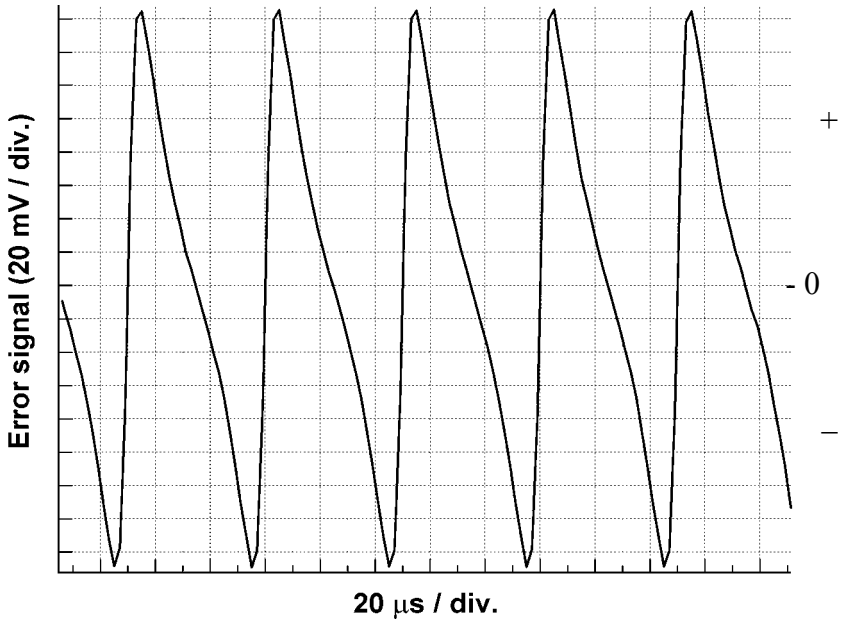

(b)

Fig. 4.2: (a) Schematic for error signal generation using the EAM two outputs and a balance detector. (b) The measured error signal generated from the system with an open loop feedback. The frequency difference between the data and clock is 10 kHz, LPF Bandwidth ≅ 15 kHz.

EAM has two outputs; each goes to one of the detector inputs. The balanced photo-detector takes the difference between its two detected electrical signals and produces an electrical error signal at its output. The output is zero if the two inputs are identical. Fig. 4.2.b shows a typical error signal. The polarity of the generated error signal indicates which pulse stream is ahead of the other, while the amplitude of the error signal indicates the amount of the delay between the two pulse streams.

We note also that the magnitude of the reverse bias and input optical power affect the error signal shape. Fig. 4.3 shows the generated error signals for different EAM input power after the balance detector (≈15 KHz bandwidth). The error signal amplitude increases with higher input power, because of more absorption saturation that allows higher transmission. Fig. 4.4 shows the generated error signals for different EAM reverse bias after the balance detector. The amplitude drops with higher reverse bias because of absorption coefficient increase inside the optical waveguide.

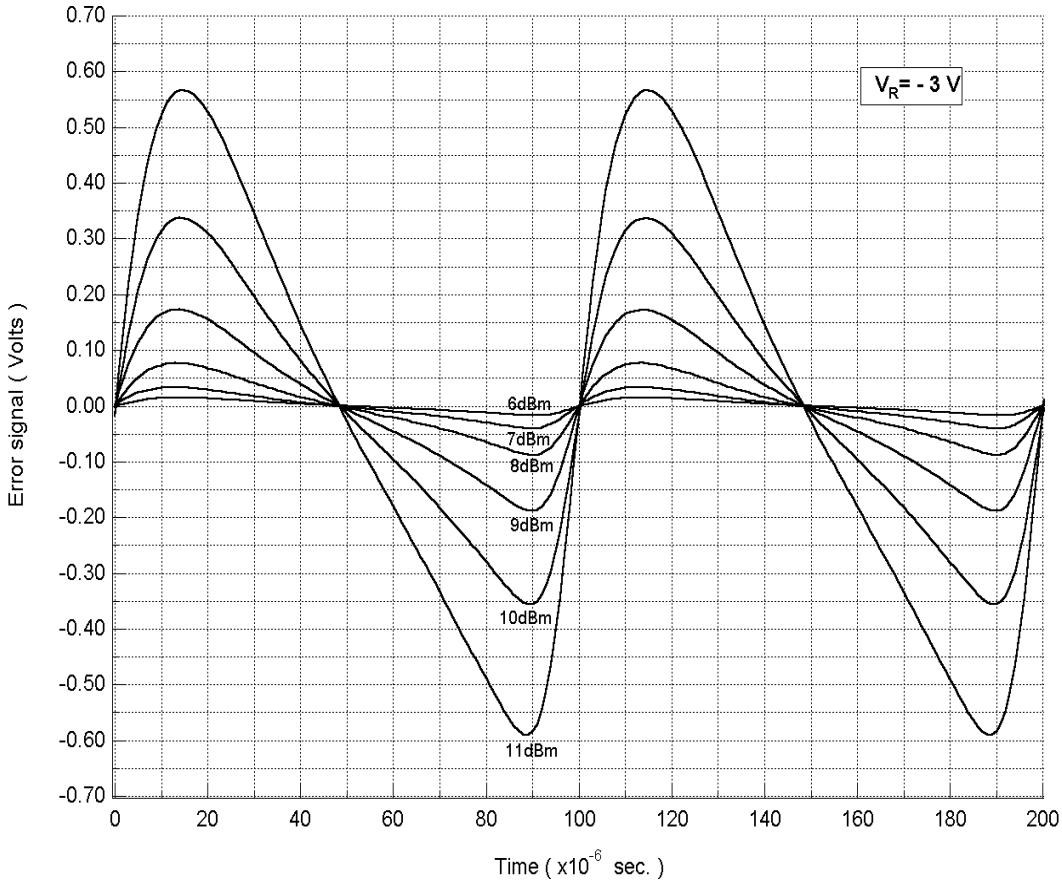

Fig. 4.3: The effect of input power on the error signal generated by using EAM at constant applied reverse bias.

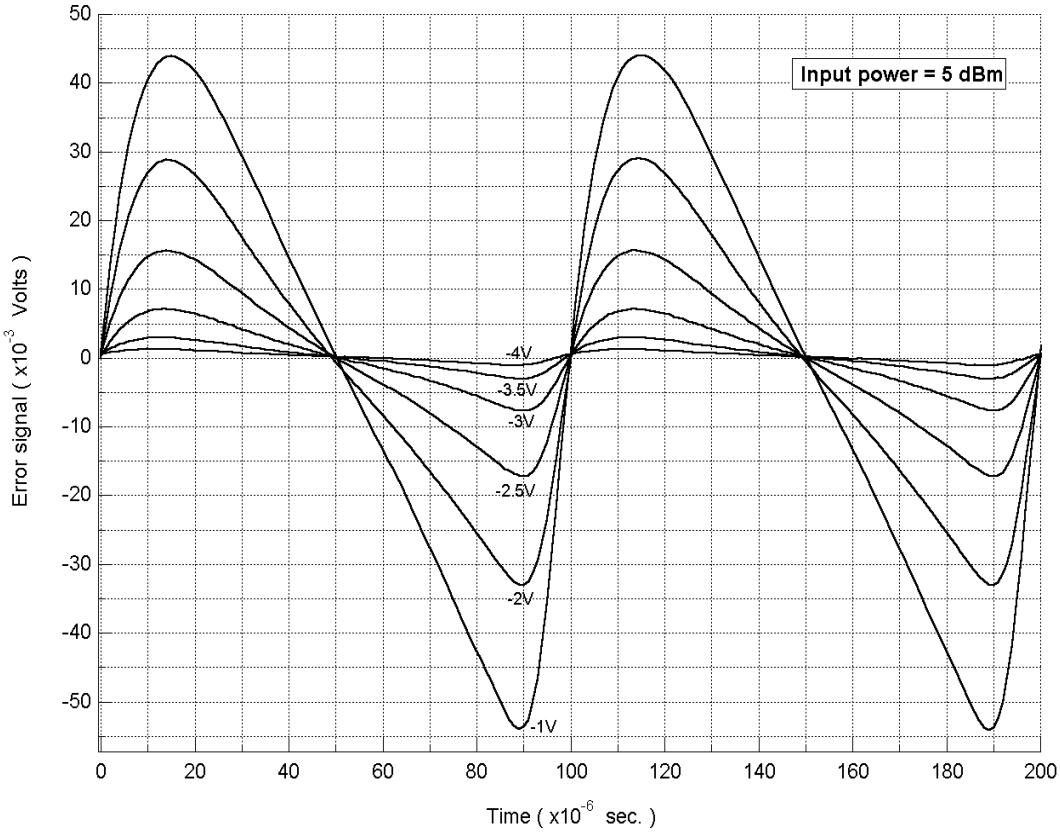

Fig. 4.4: The effect of reverse bias on the error signal generated by using EAM at constant input power.

4.1.3. Optical clock recovery system

The all-optical timing extraction technique using counter-propagation pulses gives information about the amount of delay between the two pulses and which of the two pulses arrives first. This kind of information is important for optical clock recovery. Assuming that one of the two counter-propagating pulse streams is the data while the

other is the clock, the all-optical timing extraction can be used to generate a timing error signal that in turn can be used to perform optical clock recovery.

Fig. 4.5 shows a typical configuration for the optical clock recovery system. The clock signal was derived from an optical pulse source, such as a semiconductor mode-locked diode laser, produces a stable optical pulse train. The data signal is an RZ bit stream that counter-propagates with respect to the clock signal inside the nonlinear wave-guide. The transmitted clock and data through the device are then split off and detected by a balanced photo-detector to produce the electrical error signal. This error signal is fed back through an electronic amplifier to the VCO input to adjust its repetition rate. The VCO in turn drives the optical pulse source to adjust its repetition frequency. The repetition rate and phase of the optical pulse source stabilizes only when the clock and the data are synchronized.

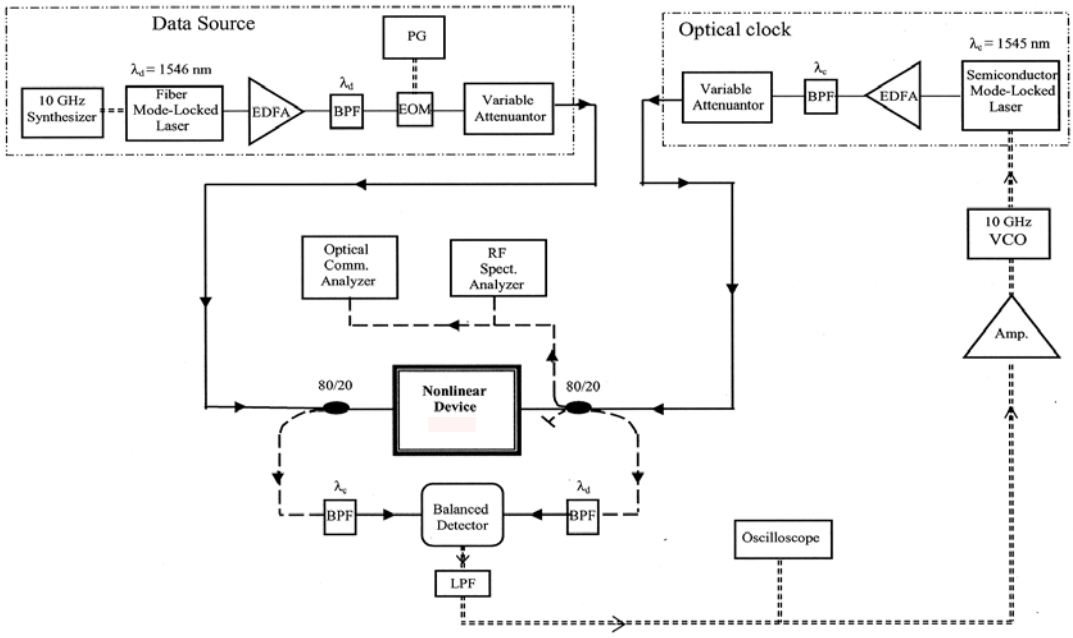

Fig. 4.5: Experimental setup for the optical clock recovery system, the nonlinear device is EAM in this case. PG: Pattern Generator, EOM: Electro-Optic Modulator, BPF: Band Pass Filter, LPF: Low Pass Filter, VCO: Voltage-Controlled Oscillator, Amp: Electrical Amplifier, EDFA: Erbium Doped Fiber Amplifier.

In the experimental setup shown in Fig. 4.5, the optical clock source is a hybrid mode locked semiconductor laser producing 3.3 ps pulses at 1545nm, with a variable repetition rate of 10GHz ± Δf, which is determined by a VCO. The data source consists of an actively mode-locked fiber laser running at 1546 nm and has a repetition rate of 10 GHz. A pattern generator and an electro-optic modulator are used to transcribe the desired RZ data patterns onto the optical pulse stream. The equally powered data and

clock pulse streams are injected into the EAM from opposite sides. The EAM has a bias voltage equals to -3 volts. The two outputs are taken from opposite sides of the device using 80/20 couplers. A balanced photo-detector (New Focus 1617) is used to generate the electrical error signal. The slow detector acts as a low pass filter (LPF) with a bandwidth of 15 kHz. Fig. 4.2 shows a sample of a generated error signal for the EAM case. The error signal is then amplified with a variable gain amplifier and fed back to the VCO (HP 83650A) that drives the hybrid mode locked laser. A portion of the recovered clock is split off by 80/20 coupler before the EAM, such that the input clock pulses can be measured. The error feedback signal is constantly monitored on a digital oscilloscope. The average input power to the device of the clock and data are both ~ 6 dBm.

In Fig. 4.2, the fundamental frequency of the error signal (10 KHz) equals to Δf and one full period of the error signal corresponds to a drift of 100 ps between the data and clock pulses. The fast slope represents the interval during which the two pulses arrive almost simultaneously inside the nonlinear wave-guide, while the slow slope represents the arrival of the two pulses far apart. The polarity of the feedback signal determines which slope that the PLL locks onto.

In order to characterize the timing jitter of the recovered clock and mode-locked laser, we measured the clock RF spectrum. The timing jitter is calculated by integrating over the spectrum phase noise pedestal [32]; see appendix B. Fig. 4.6 shows the measured RF spectrum for three different cases. Case (a) represents the free running

optical clock source by itself. It has a center frequency of 10 GHz + 10 kHz, and the calculated r.m.s timing jitter from that spectrum is ≤ 60 fs [32]. Case (b) is for a locked clock using the fast slope of the error signal. The clock central frequency shifts back to 10 GHz, which equals the received data bit rate. The calculated r.m.s timing jitter in this case is ≤ 120 fs. Case (b) has a higher timing jitter than case (a) due to the added jitter from the data itself.

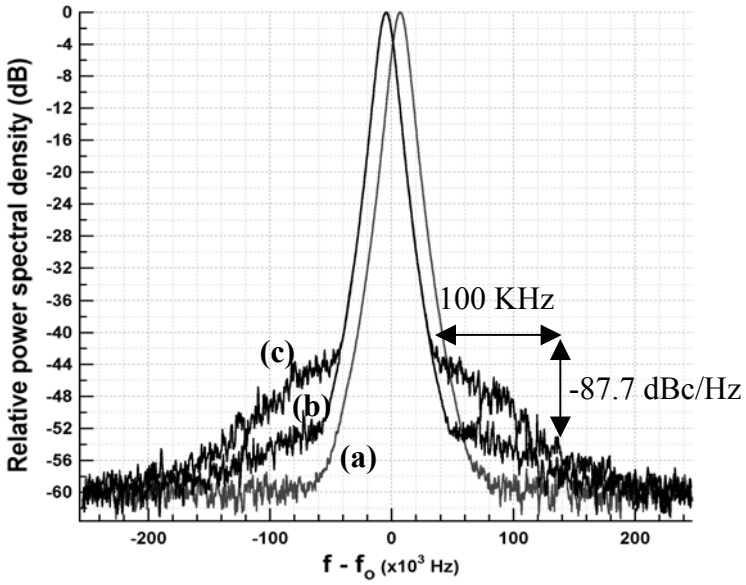

Fig. 4.6: The measured RF spectrum of the recovered clock in case of EAM: (a) Free running optical clock source, (b) Locked clock on the fast slope of error signal, (c) Locked clock on the slow slope of error signal. Resolution bandwidth = 10 kHz, f_o = 10 GHz. The shift in central frequency between lock/unlock conditions equals to 10 KHz.

Case (c) represents locking condition using the slow slope of the error signal. It has also a center frequency of 10 GHz. But the phase noise is larger than that in case (b), representing more timing jitter. For example the phase noise in case (c) equals -87.7 dBc/Hz at a frequency offset of 100 kHz, while in case (b), it is only -95 dBc/Hz at 130 kHz frequency offset. The calculated r.m.s timing jitter in case (c) was ≤ 240 fs.

The bit-error-rate measurement using the recovered clock to drive the bit error rate tester at 10 GHz and using 2^{32}-1 long PRBS data revealed an error-free operation. Fig. 4.7 shows the optical recovered clock in time domain using a 45 GHz photo-detector and a digital sampling oscilloscope.

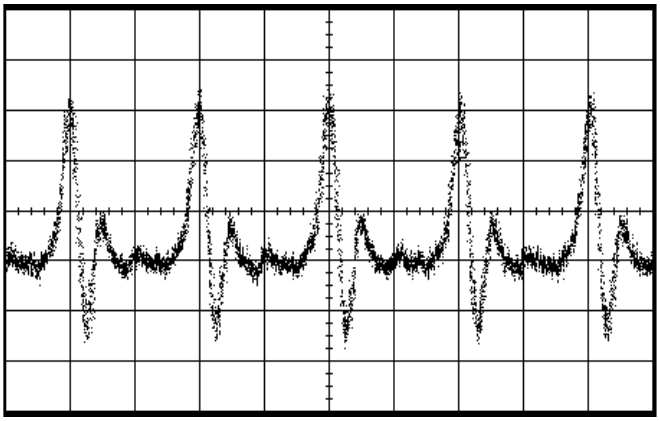

50 ps/div.

Fig. 4.7: The recovered optical clock on digital sampling oscilloscope using a 45 GHz Photo-detector.

4.1.4. 160 Gbit/s optical clock recovery using time-dependent loss saturation inside a single Electro Absorption Modulator

Sub-harmonic clock recovery at network nodes or receivers is important to allow synchronous signal processing operations on individual channels. The semiconductor-based phase-comparator is attractive due to its reasonable switching power, compactness, and possibility for integration. Here, we demonstrated ultra-high speed optical clock recovery for data rates up to 160 Gbit/s using a single EAM. The EAM acts as an all-optical phase-comparator without a need for special interferometric configurations or electronic mixers. The extracted timing is capable to resolve a sub-picosecond timing error between the data and clock pulses due to the fast loss-saturation inside the EAM, which is essential for optical clock recovery from ultra-high speed data. Also we will demonstrate that the technique is bit-rate flexible by experimentally performing optical clock recovery at different input data bit rates up to 160 Gbit/s.

As already mentioned, the transmission of the EAM is time-dependent on the delay in arrival between the two counter propagating pulses. As shown in Fig. 4.1, The EAM has a fast loss saturation, it takes few picoseconds (< 10 ps) for the loss to saturate, but the recovery time is comparatively longer. The pulse width in this experiment is about 3.3 ps with a 7 dBm input average power. The recovery time depends on the EAM reverse bias and the input optical power. For a fixed input average power and with more reverse bias the recovery time becomes shorter. The switching window in this case is ≈ 20 ps. The steep slopes in Fig. 4.1 can resolve less than 1 ps

timing delay in arrival between the two counter propagating pulses. The EAM has a slow recovery time that results in incomplete loss recovery between bits in case of ultra-high speed data, which in turn reduces the output extinction-ratio. However, the loss saturation is fast and sufficient to produce the proper feedback error signal.

By subtracting both output powers we can obtain the error signal with a fast slope as shown in Fig. 4.8. The polarity of this signal indicates which of the counter-propagating pulses arrives first, and the amplitude is proportional to the amount of delay between those pulses.

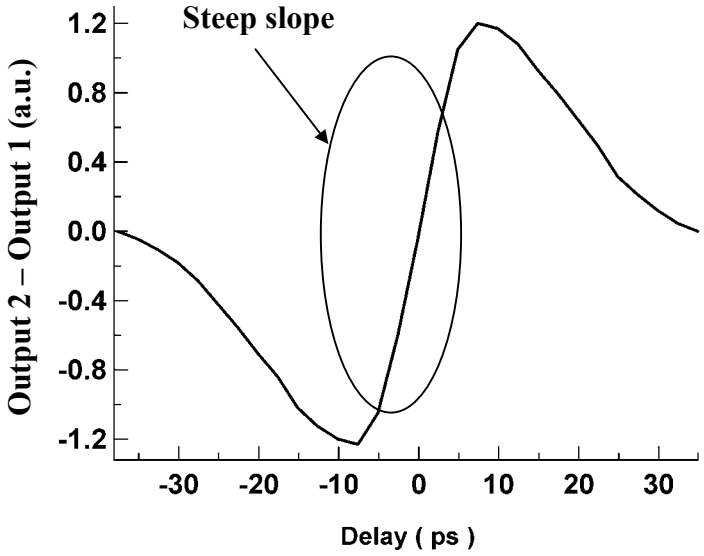

Fig. 4.8: The subtracted two outputs of the EAM.

Fig. 4.9 shows the experimental set-up for 160 Gbit/s optical clock recovery.

The RZ data pulses with a wavelength of 1550 nm and 2 ps FWHM are running at 10 Gbit/s with 2^7-1 or 2^{31}-1 PRBS. The data pulses have extinction ratio of more than 30 dB. The 10 Gbit/s is multiplexed using a multi-stage passive fiber delay line to obtain an aggregate bit rate of 160 Gbit/s, Fig. 4.10. The RZ optical clock pulses with a wavelength of 1545 nm and 2 ps FWHM pulse width, are generated using a mode-locked semiconductor laser driven by a VCO, which is running close to 10 GHz repetition rate. The input data average power is set to 6 dBm and the input clock average power is set to 4 dBm. The EAM is reverse biased at -3 volts.

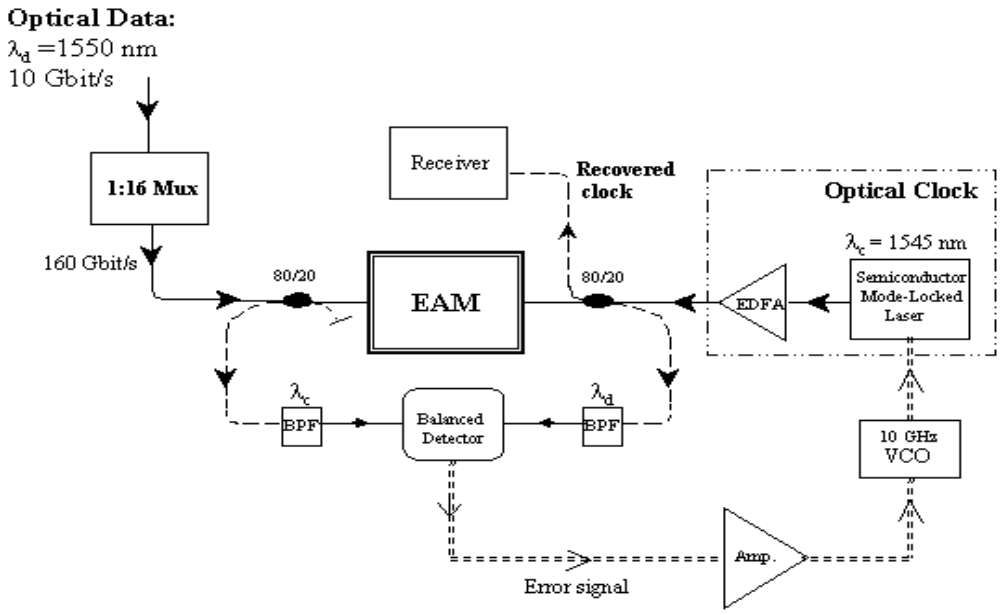

Fig. 4.9: The experimental set-up for 160 Gbit/s clock recovery. Mux: Multistage fiber-delay Multiplexer. Amp: Electrical Amplifier, VCO: Voltage-Controlled Oscillator, BPF: Band Pass Filter, EDFA: Erbium Doped Fiber Amplifier.

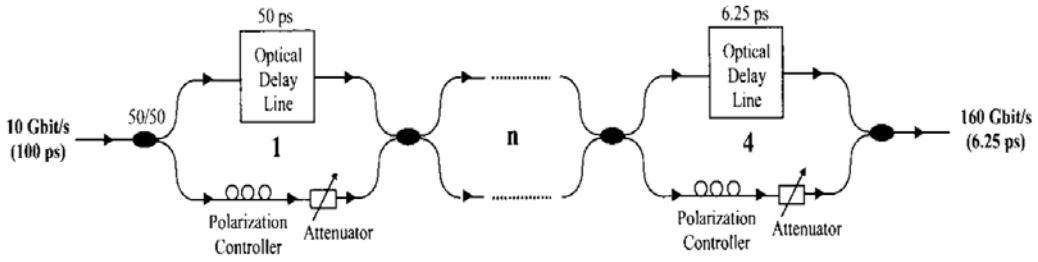

Fig. 4.10: Four stages optical fiber multiplexer for 160 Gbit/s generation.

The estimated EAM switching window at -3 volts reverse bias and the input optical power is ≈ 20 ps. Here, the balanced photo-detector bandwidth is 1 MHz. It detects the two optical outputs of the EAM and generates a low-pass filtered electrical error signal. The error signal is fed back into a phase-locked loop to control the repetition rate of the semiconductor mode-locked laser (clock source) until it locks to one of the incoming data channels. The steep slope of the error signal in this experiment has a sensitivity of ≈ 200 mV/ps, therefore it can resolve and correct for sub-picosecond timing errors between the clock and the data pulses.

Fig. 4.11 shows the measured autocorrelation trace of the 160 Gbit/s data. The deconvolved pulse width, assuming a Gaussian pulse shape, is 2 ps FWHM, and the pulses separation is 6.25 ps. The spike in the middle of the trace is typical for data autocorrelations in general. The spike occurs when the delay between the two arms of autocorrelation becomes zero, therefore each bit in the data pattern auto correlates with

itself. At different delays, a data bit (0 or 1) auto correlates with a different data bit that might be 1 or 0, thus autocorrelation amplitude drops by a factor of two. For the case of all-ones the autocorrelation amplitudes should be equal.

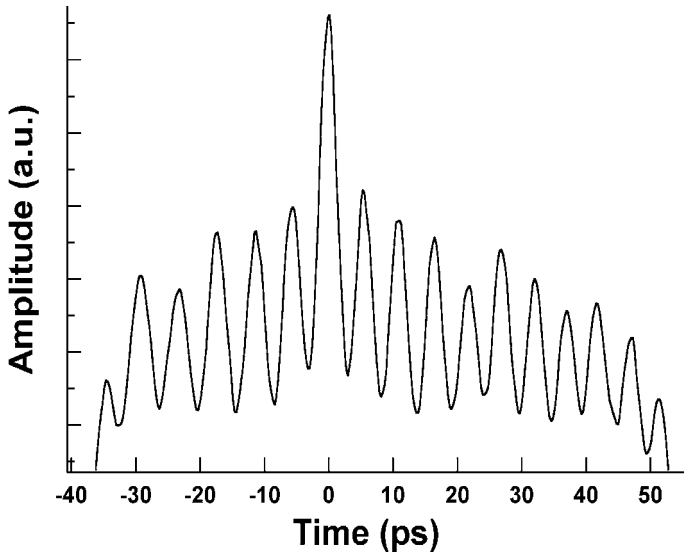

Fig. 4.11: The auto-correlation trace of the 160 Gbit/s data.

To view the error signal during the system operation, a digital oscilloscope was connected to the electrical amplifier output. Fig. 4.12 shows the error signal with a feedback loop open (unlocked) and when the feedback loop is closed (locked). The random fluctuations in the error signal amplitude, before locking, correspond to the random phase shift between the data and clock pulses. When the loop is closed the error signal turns into almost a DC voltage. The acquisition time was measured during the transition between unlock to lock conditions, and it reveals about 10 μsec of transient

time. The DC voltage maintains the clock repetition rate (10GHz) equals to the data base-rate, which is equivalent to the repetition rate of one of the incoming data channels.

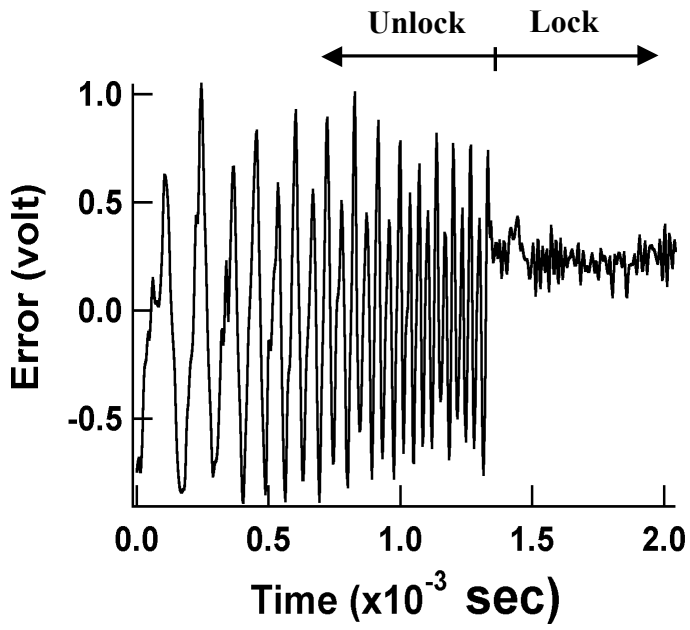

Fig. 4.12: The measured error signal transient-response at the balanced detector output during transition between unlock to lock period.

We used the RF spectrum of the clock, Fig. 4.13, to measure the timing jitter of the recovered clock as mentioned before. For 160 Gbit/s, the calculated r.m.s timing jitter of the recovered clock is ≤ 340 fs, and the measured phase noise is – 88 dBc/Hz at a 100 KHz frequency offset from the carrier.

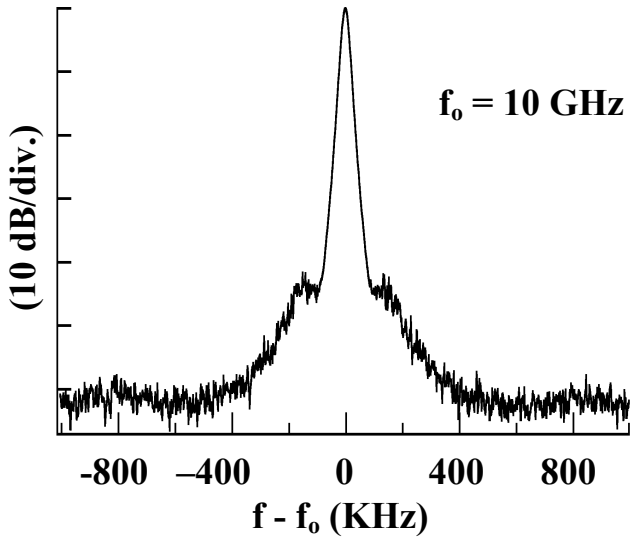

Fig. 4.13: The RF spectrum of the recovered clock at 10 GHz from 160 Gbit/s input data.

The clock recovery system was also tested at different bit rates, beside 160 Gbit/s, to check the performance. It was tested at 80, 40, 20, and 10 Gbit/s and then the timing jitter was calculated. The system shows a good locking in each case. In case of 10 Gbit/s input data, we obtain the lowest r.m.s timing jitter, which is ≤ 120 fs. The measured timing jitter of the extracted sub-harmonic clock at different bit rates is shown in Fig. 4.14. In general, this system can recover a sub-harmonic clock from the incoming data with an optical clock source running at the data base-rate. Here, we utilized a semiconductor mode-locked laser (clock) that can lock at 10 GHz and it has a free-running r.m.s timing jitter ≤ 80 fs.

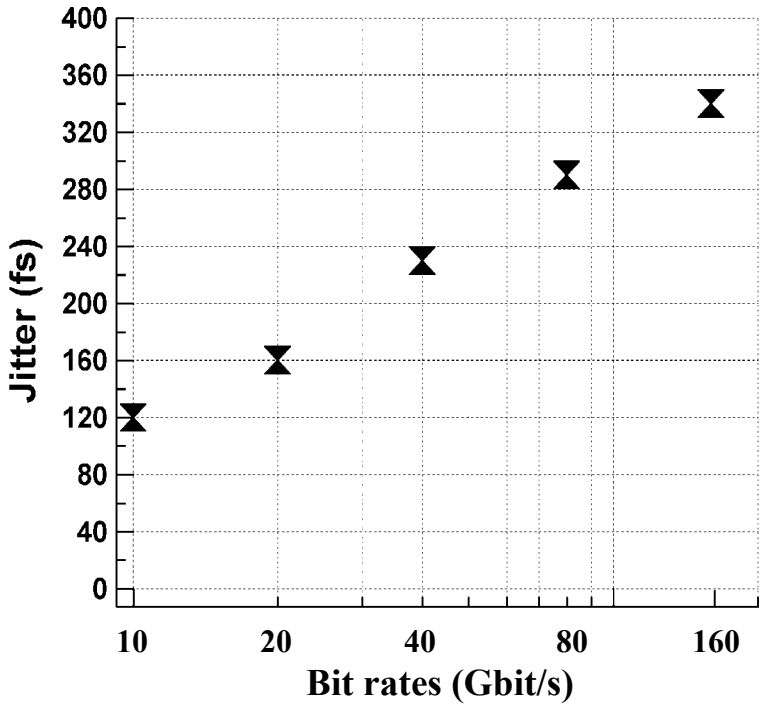

Fig. 4.14: The measured r.m.s timing jitter of the recovered clock at different data rates (semi-log scale).

In order to compare the quality of the recovered clock and the original clock used to generate the data, Bit-Error-Ratio (BER) measurements were performed. The recovered clock at 10 GHz from 160 Gbit/s data was used to drive the error detector electrical clock input, while part of the input data to the multiplexer (10 Gbit/s, 2^7 –1 or 2^{31} –1 PRBS) was split off and optically-to-electrically converted using a PIN photo-receiver to drive the error detector data input. Fig. 4.15 illustrates the BER measurements using each of the 160 Gbit/s recovered clock and the back-to-back error detector clock. In each case, The BER shows an error-free operation (BER $\leq 10^{-9}$) with

negligible receiver sensitivity penalty between the recovered and the back-to-back clock.

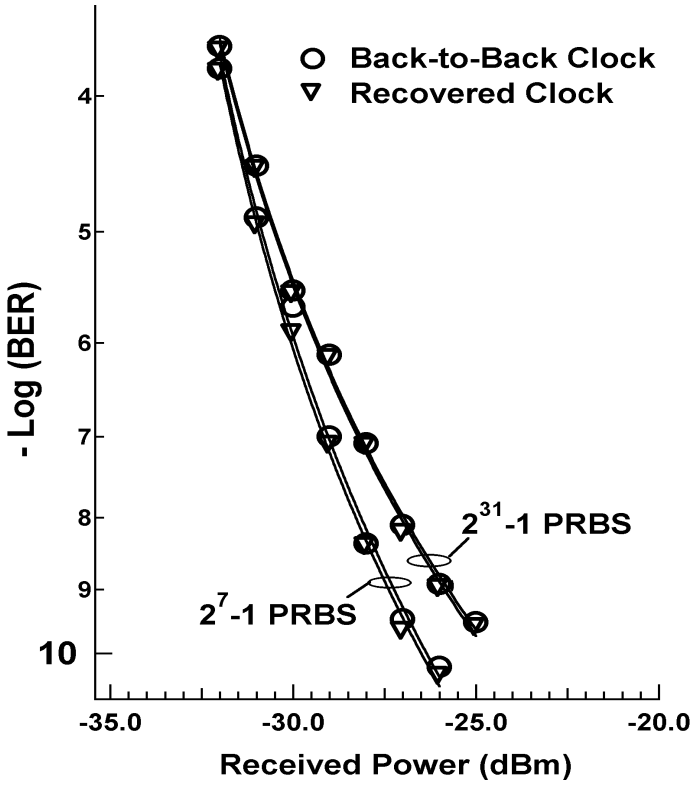

Fig. 4.15: The bit-error-ratio measurements using each of the 160 Gbit/s recovered clock and the error detector back-to-back clock.

In summary, ultra-fast optical timing extraction and clock recovery are demonstrated using a single EAM as a phase-comparator. Although operating in a regime where the EAM switching window is larger than the data bit period, the loss saturation inside the EAM is sufficient and fast to perform timing extraction. The clock

recovery system is polarization-insensitive and bit-rate flexible. Furthermore, the use of semiconductor-based components, such as EAM all-optical phase comparator, in the system allows for monolithic integration.

4.2. Optical clock recovery using an SOA

Using an SOA instead of the EAM in the same setup (Fig. 4.5) the all-optical timing extraction can be performed using gain saturation. In general an input pulse in nonlinear waveguides such as SOA causes saturation of gain through stimulation emission and thus reduces the optical gain. The carrier excitation and relaxation dynamics occur on a finite time scale that is determined by the material and structure of the waveguide. Similar to EAM, two counter-propagating pulses that can both act as the pump and the probe can be used to shorten the effective carrier dynamic time, thus allowing slow devices to operate at high speeds. The behavior in case of the equally powered counter-propagating pulses is determined by the timing difference between them, because the leading pulse will affect the transmission of the second. Since the change in peak power transmission depends on the relative delay between the two pulses inside the device. When the two pulses arrive simultaneously, both will be equally amplified and the balanced detector output is zero. When the two pulses arrive with a half bit period apart the output is also zero, owing to the symmetry in arrival and gain saturation. Only when the arrival times are not symmetric does the photo-detector output a signal whose sign and amplitude depend on the timing of the two pulses.

In the optical clock recovery experiment using SOA, the optical clock source is a hybrid mode locked semiconductor laser producing 3.3 ps pulses at 1545nm, with a variable repetition rate of 10GHz ± Δf that is determined by a VCO. The data source consists of an actively mode-locked fiber laser running at 1546nm and a repetition rate of 10GHz. A pattern generator and an electro-optic modulator are used to transcribe the desired RZ data patterns onto the optical pulse stream. The equally powered data and clock pulse streams are injected into the SOA from opposite sides. The SOA is driven with 120 mA of bias current introducing a small signal gain of ~20dB. The two outputs are taken from the opposite sides of the device using 80/20 couplers. A balanced photo-detector is used to generate the error signal. The slow photo-detector acts as a LPF with a bandwidth of 15 kHz, in this case. The error signal is then amplified with a variable gain amplifier and fed back to a VCO that drives the hybrid mode locked laser. A portion of the recovered clock is split off by the 80/20 coupler before the SOA such that the input clock source can be measured. The feedback error signal is constantly monitored using a digital oscilloscope.

The error signal for the case of SOA is expected to switch sign compared to the case of EAM shown before in Fig. 4.2, assuming same feedback polarity. This is because it is gain saturation in case of SOA and absorption saturation in case of EAM. Also the magnitude of the error signal in case of SOA is larger because of its gain. Fig. 4.16 shows the error signal for the case where the frequency difference between data and clock repetition rates (Δf) is set to 10 kHz and the feedback loop is open. The

average input power to the device of the clock and data are both ~ -7 dBm. The fundamental frequency of the error signal equals Δf and one full period of the error signal corresponds to a drift of 100 ps between the data and clock pulses. The fast slope represents the interval during which the two pulses arrive almost simultaneously inside the nonlinear waveguide, while the slow slope represents the arrival of the two pulses far apart.

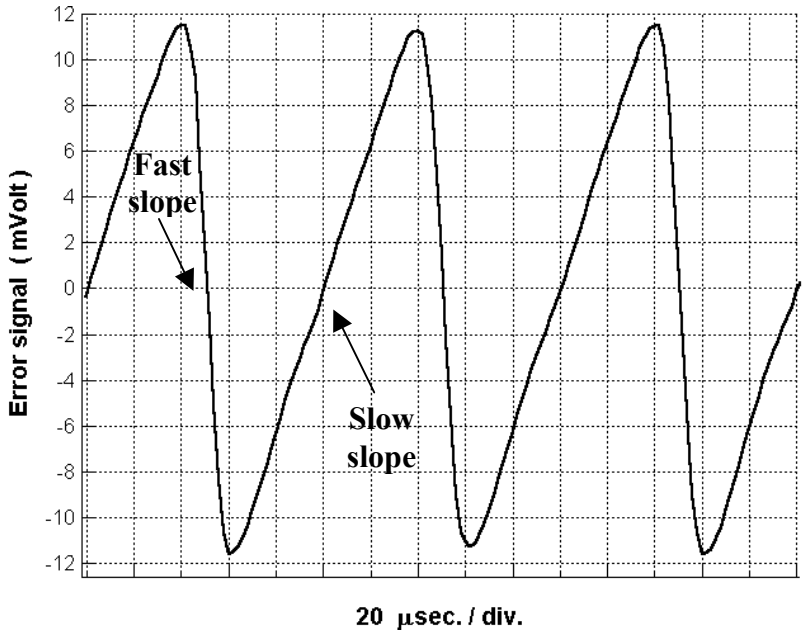

Fig. 4.16: Error signal generated from the system using SOA with open loop feedback. The frequency difference between the data and clock is 10 kHz, LPF Bandwidth ≅ 15 kHz.

The polarity of the feedback signal determines which slope that the PLL locks onto. Fig. 4.17 represents the transient time response of the error signal during

switching from the unlocked to locked condition. In this case the data repetition rate is 10 GHz, while the clock repetition rate was adjusted at 10GHz+10 kHz.

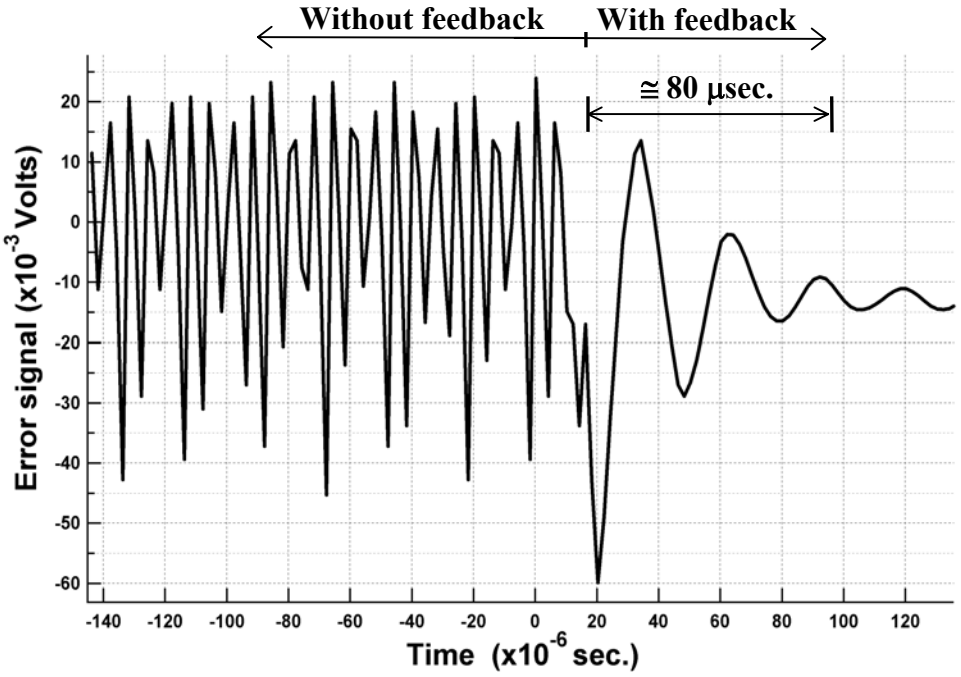

Fig. 4.17: The measured error signal transient-time during transition between unlock to lock conditions for SOA case.

Before locking (without feedback) the error signal has large oscillations indicating large error. Closing the feedback loop results in a transient behavior with 80 μs settling time (15 KHz LPF bandwidth), after which the error signal approaches the lock condition with almost a DC error voltage indicating the offset voltage applied to the VCO, which is needed to set $\Delta f = 0$. We found that the settling time becomes

shorter with a larger LPF bandwidth. For example, using a detector with a 100kHz bandwidth produces a 40 μs settling time.

Fig. 4.18 shows the measured RF spectrum for three different cases Case (a) represents the free running optical clock source by itself. It has a center frequency of 10 GHz + 10 kHz, and the calculated r.m.s timing jitter [32] from that spectrum is ≤ 84 fs. Case (b) is for a locked clock using the fast slope of the error signal. The clock central frequency shifts back to 10 GHz, which equals to the received data bit rate.

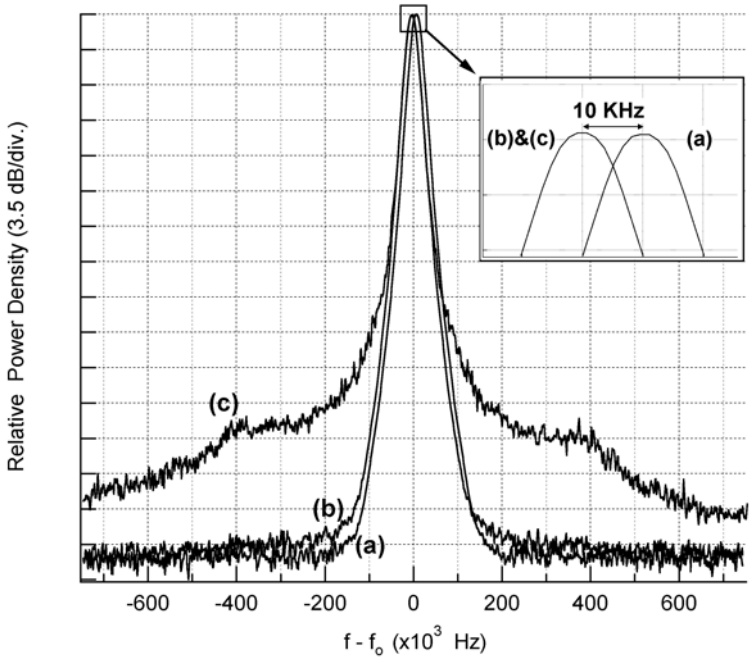

Fig. 4.18: The measured RF spectrum of the recovered optical clock in case of SOA: (a) Free running optical clock source, (b) Locked clock on the fast slope of error signal, (c) Locked clock on the slow slope of error signal. Resolution bandwidth = 21.5 kHz, f_o = 10 GHz. The inset shows the shift in the central frequency.

The calculated r.m.s timing jitter is ≤ 100 fs. It has a slightly higher timing jitter than case (a) due to the added jitter from the data itself. Case (c) represents locking condition using the slow slope of the error signal. It has also a center frequency of 10 GHz. But the phase noise is larger than that in case (b), representing more timing jitter. For example the phase noise in case (c) equals -82 dBc/Hz at a frequency offset of 100 kHz, while in case (b), it is -92 dBc/Hz at 130 kHz frequency offset. The calculated r.m.s timing jitter in case (c) is ≤ 430 fs.

The bit error rate measurement for the system using the optical recovered clock to drive the error detector at 10 GHz, and with back to back electrical data input to the error detector, using a 2^{32} -1 PRBS, revealed an error free operation (BER $<10^{-12}$). Comparing to the EAM case, the required input saturation power in case of SOA is less than that of EAM by about 10 dB. However, the SOA adds some ASE noise to the generated error signal that can increase timing jitter, assuming same operating conditions as EAM case.

4.3. Optical clock recovery modeling

In this section we present a model for optical clock recovery system using EAM and SOA. The model is based on nonlinear optical pulse propagation inside gain [19][33] or absorptive medium. For the case of amplifiers such as SOA, the basic equations that govern the pulse propagation and saturation analysis are:

Propagation along '+ z' direction: $$\left(\frac{\partial}{\partial z}+\frac{n}{c}\frac{\partial}{\partial t}\right)P_1(z,t)=g(z,t)P_1(z,t) \quad (1)$$

Propagation along '– z' direction: $$\left(\frac{-\partial}{\partial z}+\frac{n}{c}\frac{\partial}{\partial t}\right)P_2(z,t)=g(z,t)P_2(z,t) \quad (2)$$

Gain/Loss saturation and relaxation: $$\frac{\partial}{\partial t}g(z,t)=\frac{g_o-g(z,t)}{\tau_r}-\frac{g(z,t)P_{total}}{E_{sat}} \quad (3)$$

Where 'n' is the medium refractive index, 'c' is the speed of light in vacuum, P(z,t) is the optical power at point 'z' and time 't', g(z,t) is the gain coefficient, 'τ_r' is the recovery time, and 'E_{sat}' is the saturation energy for the gain medium.

The above three equations are difficult to solve analytically; therefore, we solved them numerically. A Matlab program developed for this purpose is presented in appendix A. We assumed the EAM or SOA is divided into 'N' sections along the device length, as shown in Fig. 4.20, to model the gain/loss spatial effect on propagating pulses

along the device. The output of each section becomes the input to the following section. For a single section with a small length 'Δz', with a small error, the two counter-propagating pulses can be considered to be co-propagating [20].

For each time step in numerical simulation, we can find the saturated gain of each segment using same procedures as [33]. The output power $P_{out1}(t)$ can be written as a function of input power $P_{in1}(t)$:

$$P_{out\,1}(t) = G(t) \times P_{in\,1}(t) \qquad (4)$$

Similarly, $$P_{out\,2}(t) = G(t) \times P_{in\,2}(t) \qquad (5)$$

Where $G(t) = \exp[g(t)]$ is the time-varying partially saturated gain:

$$G(t) = \ln\left\{\frac{G_o}{G_o - (G_o - 1)\exp\left[-\left(P_{in\,1}(t) + P_{in\,2}(t)\right)/E_{sat}\right]}\right\} \qquad (6)$$

Eq. (6) expresses the gain saturation with time as a function of total input power ($P_{total}(t)=P_{in1}(t) + P_{in2}(t)$). This equation does not take into account the gain recovery time. However, at each time step, the saturated gain recovers to its initial value 'G_o' with a recovery time 'τ_r' according to eq.(7).

$$\frac{\partial}{\partial t} g(z,t) = \frac{g_o - g(z,t)}{\tau_r} \qquad (7)$$

In the case of EAM, the model follows the same principles. However the gain coefficient (g) is replaced with absorption coefficient (a = - g), which gives the total saturated absorption as a function of time A(t) = Exp[a]. The experimental values of the absorption coefficient is a function of the reverse bias as shown earlier in Fig. 2.3 & Fig. 2.5. The recovery time in EAM depends on the input power and the carrier sweep out dynamics inside the waveguide under the influence of the applied electric field. We have used the experimental data, shown in Fig. 2.5, to include the carrier recovery time in the model. The recovery time dependence on input power and reverse bias has been taken from this data and entered numerically into the model.

Fig. 4.19 shows the simulated transmission of EAM as a function of input pump power and different reverse bias. It has a good agreement with the experimental data shown earlier in Fig. 2.3.

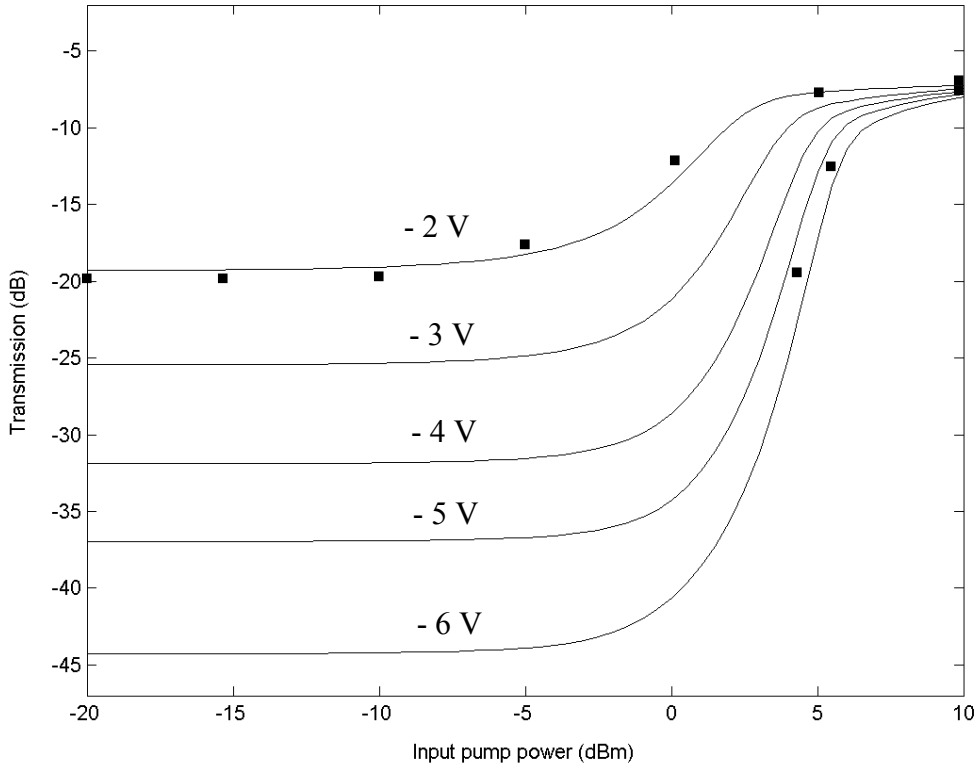

Fig. 4.19: The solid lines show simulation of EAM transmission functions for different input pump power and reverse bias. The dots show some experimental points at –2 and –6 volts.

The clock recovery model (Appendix A) includes a device model for EAM or SOA as described above. We find out that three sections are enough for a good approximation. Fig. 4.20 shows a schematic configuration of the PLL open feedback loop.

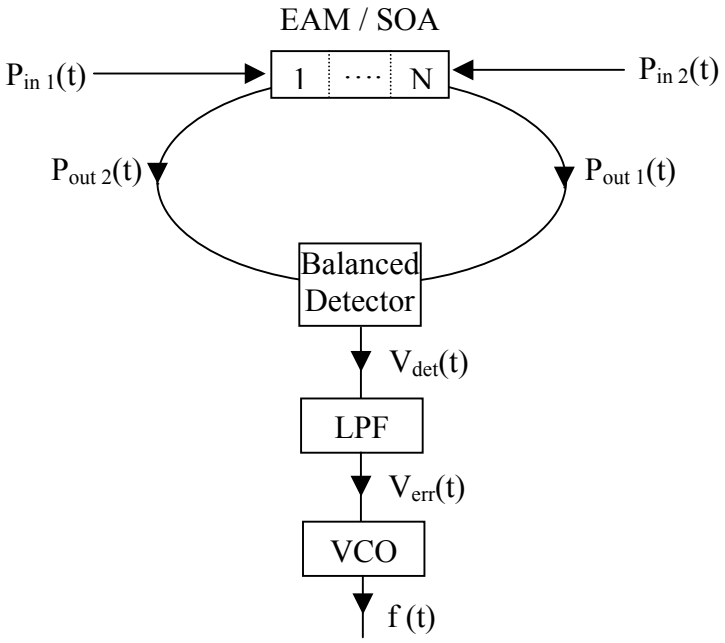

Fig. 4.20: Schematic configuration of the PLL open feedback loop.

Using eq. (4) & (5), the balanced photo-detector output voltage can be expressed as:

$$V_{det}(t) = f(\varphi) = \left[P_{out\,1}(t) - P_{out\,2}(t)\right] \cdot \frac{\eta e}{\hbar w} \cdot Z_L \qquad (8)$$

Where 'η' is the photo-detector quantum efficiency, 'e' is the electron charge, '$\hbar$' is Planck's constant, 'w' is the optical frequency in radian/sec., 'Z_L' is the photo-detector load impedance.

The balanced photo-detector output voltage $V_{det}(t)$ is a function of the time delay between the two input counter-propagating pulses, or the phase difference 'ϕ' between

the RF of signal and clock. The f(ϕ) can be found by numerically solving for $P_{in\,1}(t)$ and $P_{in\,2}(t)$ as described above, a Matlab program is included in appendix A.

The signal from the balanced photo-detector goes through a low pass filter (LPF). The output of LPF is the error signal [$V_{err}(t)$] which is obtained by solving:

$$\frac{dV_{err}(t)}{dt} = V_{det}(t) - \frac{V_{err}(t)}{\tau_f} \qquad (9)$$

Where 'τ_f' is the LPF time constant. This error signal is multiplied by the feedback gain factor, and then used to control the repetition frequency of the optical clock pulses, which is controlled by the VCO.

The VCO instantaneous repetition frequency $\nu(t)$ is given by:

$$2\pi \cdot \nu(t) = \frac{d\varphi}{dt} = K_1 \cdot V_{err}(t) \qquad (10)$$

Where $K_1 = 2\pi \cdot G_e K_{VCO}$ & $\Delta\varphi = 2\pi \cdot \frac{\Delta t}{T}$

'G_e' is the feedback voltage gain, 'K_{VCO}' is the VCO coefficient (Hz/V), and 'T' is the pulses repetition period.

If we assume that the phase variation between the counter-propagating pulses after locking is small, we can derive an analytical solution for transient response. The photo-detector output voltage in eq. (8) can be approximated by simple linear relation:

$$V_{det}(t) \approx K_2 \varphi \qquad (11)$$

Where 'K_2' is a constant.

Substituting eq. (9)&(11) into eq.(10):

$$\therefore \quad \frac{d^2\varphi}{dt^2} = K_1\left[K_2\varphi - \frac{1}{K_1\tau_f}\frac{d\varphi}{dt}\right] \qquad (12)$$

$$\therefore \quad \frac{d^2\varphi}{dt^2} + \frac{1}{\tau_f}\cdot\frac{d\varphi}{dt} - K_1K_2\varphi = 0 \qquad (13)$$

Eq. (13) is a second order differential equation, which has a solution in the form of $\exp[s\cdot t]$, where 's' is given by:

$$s = \frac{-1}{2\tau_f} \pm \frac{1}{2}\sqrt{\frac{1}{\tau_f^2} + 4K_1K_2} \qquad (14)$$

The solution for 's' depends on the sign of the product K_1K_2, which depends on the polarity of the feedback loop. Thus, we can have one of the following possible cases:

Case (1): $K_1K_2 > 0$, hence 's' is pure imaginary and the solution is growing up (unstable solution) or exponentially decaying.

Case (2): $K_1K_2 < 0$ & $|K_1K_2| < \frac{1}{4\tau_f^2}$, hence 's' is also pure imaginary and the solution is similar to that in case (1).

Case (3): $K_1K_2 < 0$ & $|K_1K_2| > \frac{1}{4\tau_f^2}$, hence the solution will be in the form $\exp\left[\frac{-1}{2\tau_f}\cdot t\right]\cdot\exp\left[\mp i\sqrt{|K_1K_2|-\frac{1}{4\tau_f^2}}\cdot t\right]$. Which is oscillatory and exponentially decaying (stable solution). This solution matches our experimental results of the error signal transient response behavior, such as the one in Fig. 4.17. In this case the exponential decay time constant is ($2\tau_f$), and the acquisition time $\approx 2/\tau_f$. The calculated acquisition time is 8 μsec, which is very close to the experimental value of 10 μsec using a LPF with 1MHz bandwidth.

The holding range and capture range have been extensively investigated in general in PLLs. The holding range of the PLL is defined as the range in which a PLL is able to maintain lock statically [34]. The capture range is defined as the frequency range within which a PLL is able to lock to the incoming signal frequency, assuming it starts from a complete unlock condition.

The holding range of the PLL can be estimated from the error signal. The edge of the holding range is reached at the point where the slope of the error signal changes sign [3]. According to our experiment a typical value for the peak-to-peak amplitude of

the error signal after the LPF is about 1 volt, and the VCO sensitivity is 1 MHz/V. Assuming the loop locks at the mid-point of error signal slope, thus the calculated holding range is Δf_{Hold}= 0.5 volt x 1 MHz/V = 500 KHz.

Usually the capture range is difficult to calculate analytically, however it can be approximated by the following formula [3]:

$$\Delta f_{capture} = f_{LPF} \cdot \left[\frac{1}{2} \cdot \left(-1 + \sqrt{1 + \left(\frac{2K_{PD} G_e K_{VCO}}{f_{LPF}} \right)^2} \right) \right]^{1/2} \qquad (15)$$

Where 'K_{PD}' is the phase detector coefficient ≈ 0.53 V/rad., K_{VCO}= 1MHz/V, and f_{LPF} = 1MHz. Thus the calculated capture range is about 470 KHz.

Fig. 4.21 shows the simulated error signal using the EAM at different input pulse energy. As expected the error signal amplitude increases with higher input power. In this case, the frequency offset between the data and clock repetition rates is set to 200 MHz.

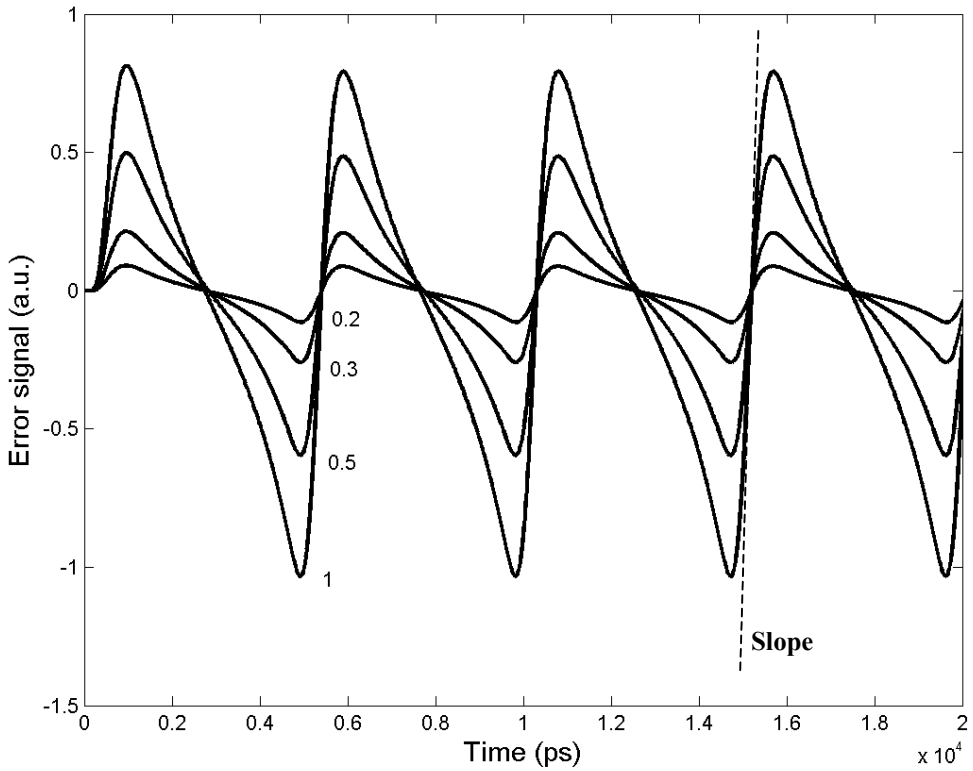

Fig. 4.21: Simulated error signal versus time using EAM at different input pulse energy normalized with respect to E_{sat}. Δf =200MHz.

Unlike the EAM case, the generated error signal with SOA has the opposite polarity and larger amplitude because of the SOA gain, Fig. 4.22.

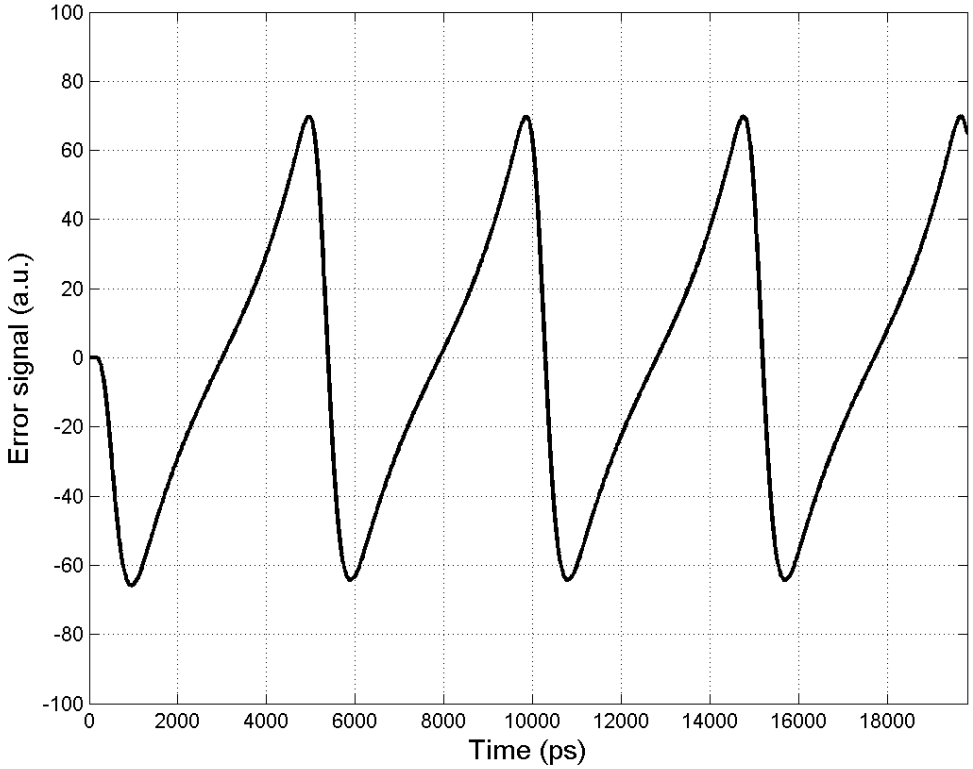

Fig. 4.22: Simulated error signal using an SOA, with unsaturated gain coefficient=2, E_{sat}=1, and recovery time =100ps, Δf =200MHz.

Also, the simulation results show a successful lock operation up to 640 Gbit/s using EAM. Fig. 4.23 shows the transient response of the error signal amplitude and the delay (Δt) between the clock and data versus time for the EAM case. Case (c) has more noise than case (a) and (b) due to some quantization error caused by the LPF approximation.

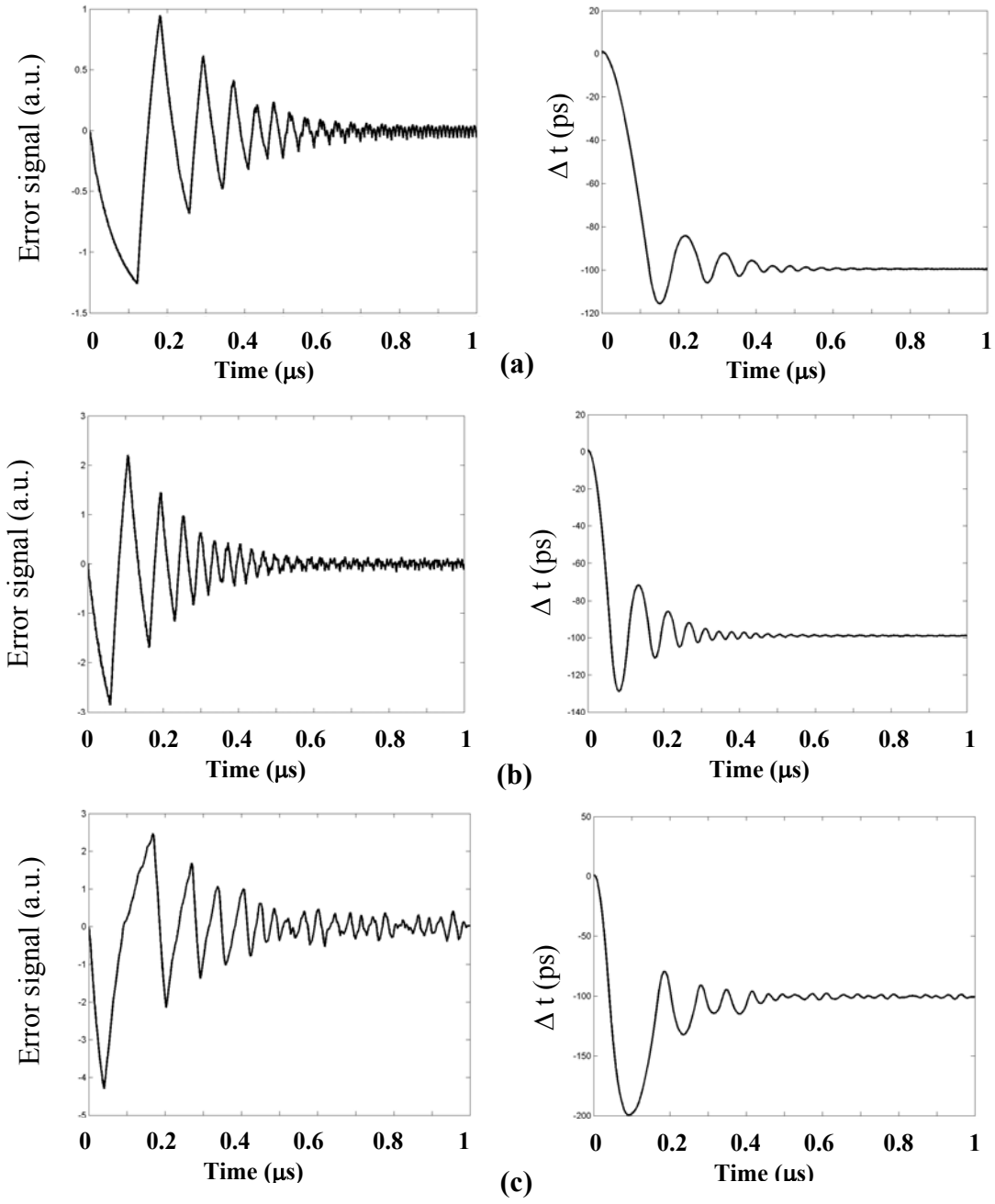

Fig. 4.23: The simulated transient response of the error signal using EAM with a 2^7-1 PRBS data, running at: (a) 640 Gbit/s, (b) 160 Gbit/s, (c) 10 Gbit/s. LPF BW ≈ 100MHz, Δf= 1MHZ.

Also, a similar behavior has been verified for the SOA case. Fig. 4.24 shows the transient response in SOA case at 10 Gbit/s with inverted polarity for the error and delay signals.

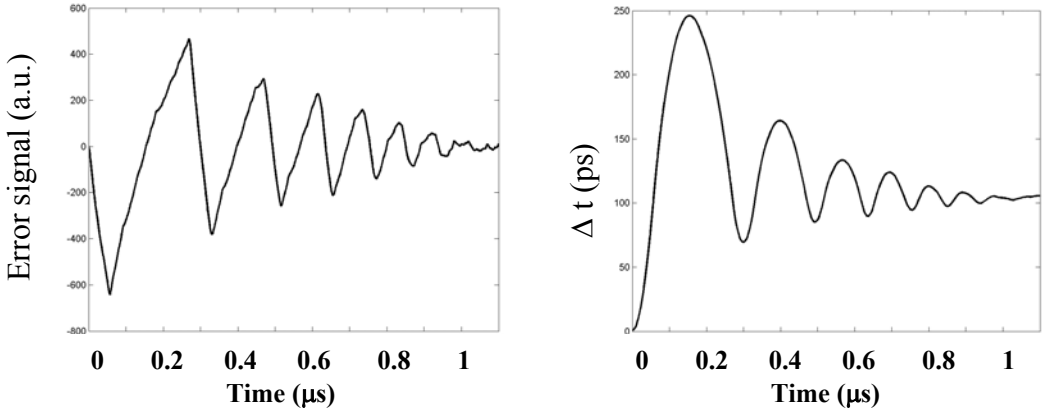

Fig. 4.24: The simulated transient response of the error signal using SOA with a 10 Gbit/s, 2^7-1 PRBS data. Unsaturated gain coefficient =2, recovery time =100 ps, LPF BW ≈14MHz, Δf= 1MHZ.

From the model, we observed that the timing jitter is related to the error signal slope 'S' which is defined as:

$$S = \frac{dV_{err}(t)}{d(\Delta t)} \qquad (16)$$

Where 'Δt' is the time of the error signal slope, and '$V_{err}(t)$' is the error signal voltage.

In the following we discuss the effect of error signal slope on the timing jitter. The slope of the error signal can be measured experimentally from the error signal when the clock is unlocked, as shown in Fig. 4.21. As discussed earlier, one full period of the error signal corresponds to a drift equal to one repetition time period between the data and clock pulses (e.g. 100 ps). Therefore, the error signal time is proportional to the time delay between the data and clock pulses. Over large interval the slope is approximately constant, and it can be calculated from the data.

After locking, the same calculated slope can be used to estimate the timing jitter between the data and clock. In that case, 'Δt' corresponds to the timing jitter between the data and clock pulses, and '$V_{err}(t)$' is the fluctuation of the error signal amplitude after locking, which is proportional to the system noise. Assuming this noise is almost constant at different bit rates, the timing jitter is inversely proportional to the error signal slope. Fig. 4.25 shows the simulation of the slope inverse (1/slope) at different input pulse energy, which is proportional to input data rate. The slope inverse increases with higher input energy and it eventually saturates. Therefore, the timing jitter is expected to increase with higher bit rates as the data input peak power and energy reduces and also the error signal fast slope reduces. Assuming a fixed input peak power at all data rates in the model, the jitter should stay approximately constant. This case is shown by simulation in Fig. 4.26.

Also, the model has been used to calculate the timing jitter in the EAM case at different bit rates, which has been already measured in the experiment (Fig. 4.14). Fig.

4.27 shows the r.m.s timing jitter in (fs) at different data bit rates up to 160 Gbit/s, which has a good agreement with the experimental results.

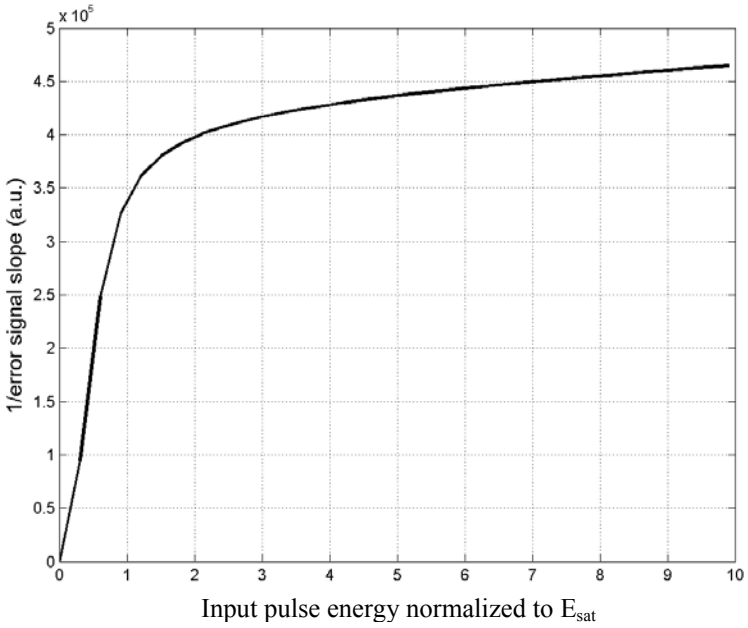

Fig. 4.25: The slope inverse as a function of input pulse energy, at 10 Gbit/s.

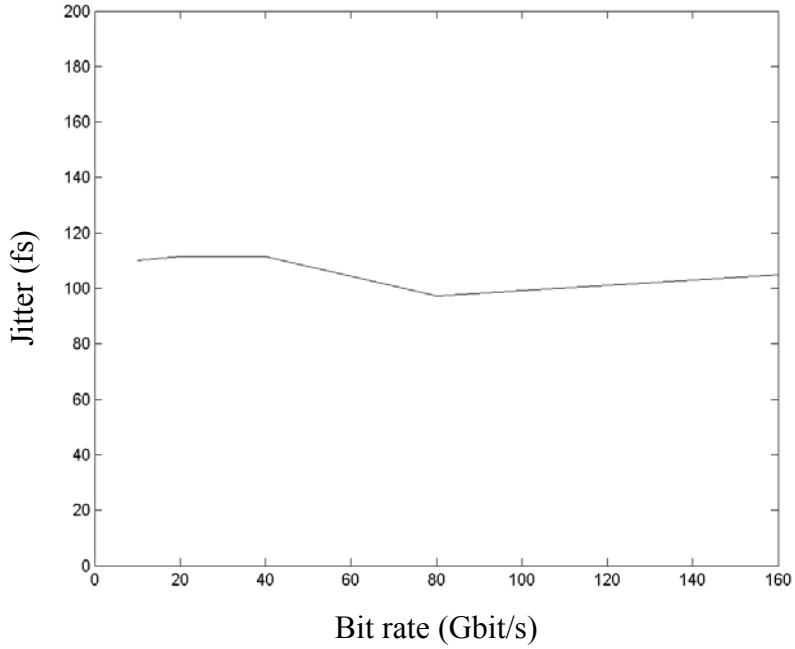

Fig. 4.26: The simulated timing jitter versus data bit rates, assuming constant data peak power.

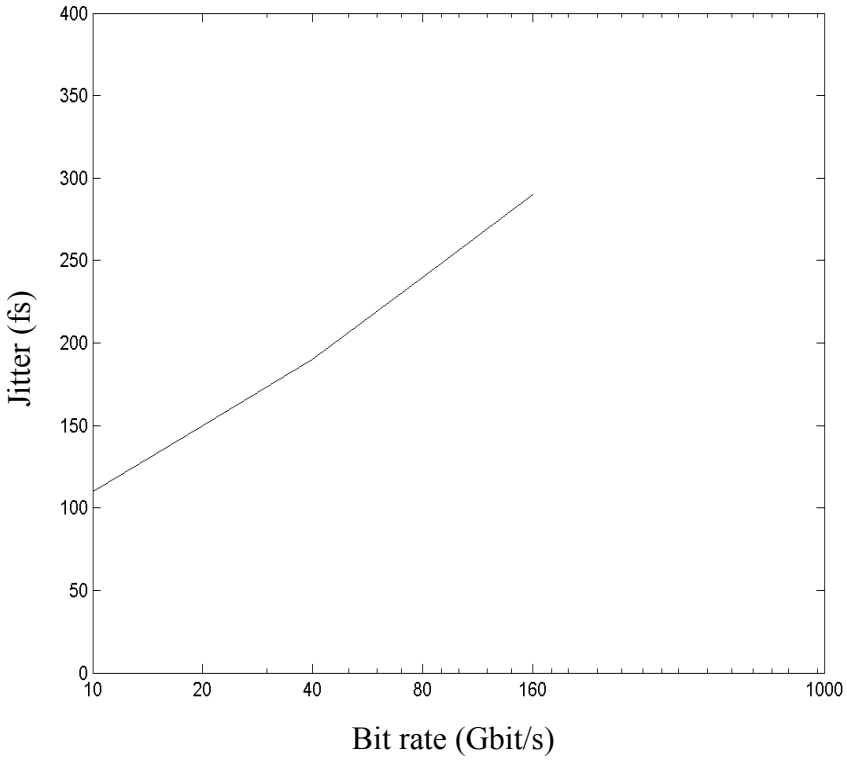

Fig. 4.27: The simulated timing jitter as function of different data bit rates.

Chapter 5

Optical demultiplexing & 3R regeneration using a single EAM

5.1. All-optical timing extraction with simultaneous optical demultiplexing from 40 Gbit/s using a single Electro-Absorption Modulator

Optical demultiplexing and clock recovery are mandatory for the future optical time division multiplexing (OTDM) systems. The clock recovery is essential for synchronization with the incoming data in order to control the demultiplexer-switching window [35]. Optical demultiplexing has been demonstrated using different techniques. For example, SOA-based nonlinear optical loop mirrors [36], electro-absorption modulators [37], and Mach-Zehnder integrated interferometers [38].

In this section we are going to describe a technique that utilizes a single EAM to perform all-optical timing extraction with simultaneous optical demultiplexing. As mentioned in the previous chapter, the counter-propagation between the clock and the data pulses inside the EAM is used to perform all-optical timing extraction and clock recovery. The demultiplexing technique here is based on modulating the transmission of the EAM optically, using a counter-propagation scheme between the data and clock optical pulses. The recovered clock pulses control the switching window of the EAM in order to demultiplex one of the incoming data channels. Unlike the conventional

demultiplexing techniques that are based on electrically controlled EAM, here we use all-optical modulation for optical demultiplexing and simultaneous timing extraction inside a single EAM.

Fig. 5.1 shows the experimental setup for optical demultiplexing with simultaneous clock recovery from 40 Gbit/s. The data source has an actively mode-locked fiber laser that produces RZ pulses at 10GHz repetition rate with a 1545nm wavelength and a 3.3ps pulse width. The pulses extinction ratio is more than 30 dB. A pattern generator and an electro-optic modulator are used to transcribe a 2^{31}-1 PRBS data onto the optical pulse stream. The 40 Gbit/s data stream (4x10Gbit/s) is generated using a passive fiber multiplexer similar to that in Fig. 4.10.

The optical clock pulses (RZ) were generated using a hybrid active-passive mode locked semiconductor laser driven by a VCO running at 10GHz ± Δf. The clock pulses have a 3.3 ps pulse width with a wavelength of 1550 nm. The two optical sources are completely independent and not synchronized, so that when the feedback loop is open, both sources encounter a random shift in repetition rate and timing jitter with respect to each other. The input data average power to the EAM is set to 7 dBm while the clock average power is set to 11 dBm. The EAM reverse bias in this case is -3.5 volts. Under these operating conditions, the EAM switching window contrast is 20 dB, and the switching window width is 18 ps. The polarization dependent loss of the EAM as mentioned before, is < 1 dB. Each of the two outputs of the EAM was split off using an 80/20 coupler and then applied to the balanced detector inputs. The recovered clock

was split off using an 80/20 coupler, while the output counter-propagating demultiplexed channel was split off using another 80/20 coupler. The measured back reflection from the fiber pigtailed EAM is approximately -40dB, thus with the help of a band-pass filter the back reflected clock pulses does not interfere with the output counter-propagating demultiplexed channel.

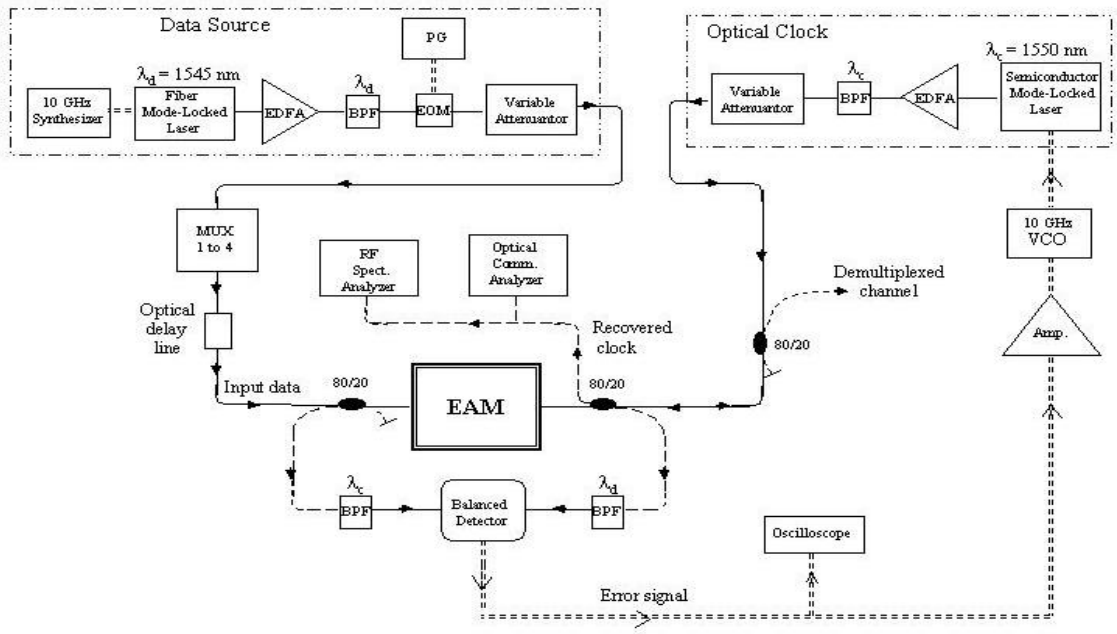

Fig. 5.1: The experimental setup for 40 Gbit/s optical demultiplexing with simultaneous clock recovery. PG: Pattern generator, BPF: Band pass filter, Amp: Electrical amplifier, MUX: Passive optical fiber multiplexer, EDFA: Erbium Doped Fiber Amplifier, EOM: Electro-optic Mach-Zehnder modulator, VCO: Voltage-Controlled Oscillator.

Fig. 5.2 is an illustrative example of the generated error signal at the output of the slow balanced detector that has a bandwidth of 100 KHz in this case. In this example the feedback loop is open, and the difference between the sources repetition frequency (Δf) (before multiplexing) is adjusted to be 10 KHz. Therefore, the repetition frequency of the error signal is 4x10 KHz.

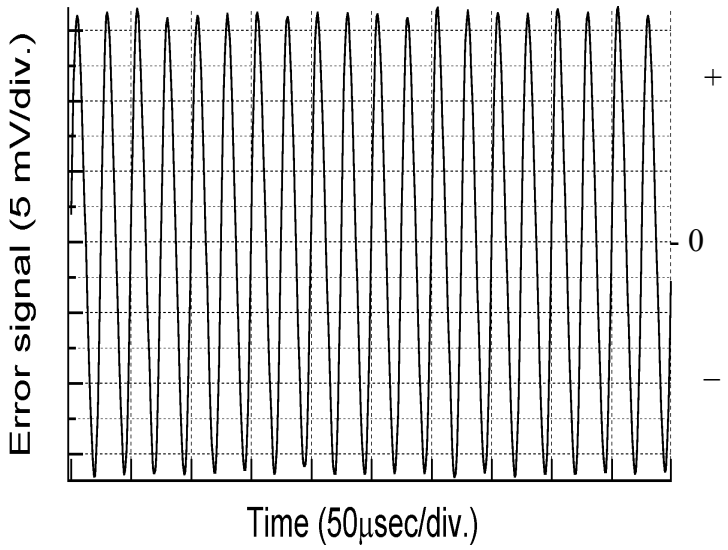

Fig. 5.2: The generated error signal at the output of the balance detector (Bandwidth = 100KHz) with an open feedback loop, Δf = 10 KHz.

The error signal is utilized in a configuration similar to conventional phase-locked loop to drive a VCO, which in turn drives an RF mode-locked laser (clock pulses). The error signal controls the repetition rate of the clock pulses until it becomes equal to that of the counter-propagating pulse stream (data).

Once the two repetition rates becomes equal, the error signal turns into almost a DC voltage, which keeps the two repetition rates the same and maintains the timing delay between the two pulse streams at some fixed value (lock condition). This delay value can be slightly tuned by varying the electrical gain in the electrical feedback path until the clock pulses overlaps with the EAM switching window. Using an optical delay line, the delay between the incoming data and the clock can be adjusted to select the desired demultiplexed channel. The demultiplexing operation can be performed at the same time with optical clock recovery. As the leading pulse (clock) saturates the loss inside the wave-guide the following incoming counter-propagating pulse (data bit) will see high transmission and propagate to the output. Given that the data rate is higher than that of the clock and the recovery time of the device under reverse bias is fast enough, the data pulse that is not preceded by a clock intense pulse will be absorbed inside the wave guide allowing demultiplexing for the selected channel only.

Fig. 5.3.a shows the eye diagram of the 40Gbit/s four multiplexed channels (10Gbit/s, 2^{31}-1 PRBS). Fig. 5.3.b is the eye diagram of one of the arbitrary selected output demultiplexed channel (25ps/div). Fig. 5.3.c is the recovered clock (10 GHz) associated with the demultiplexed channel.

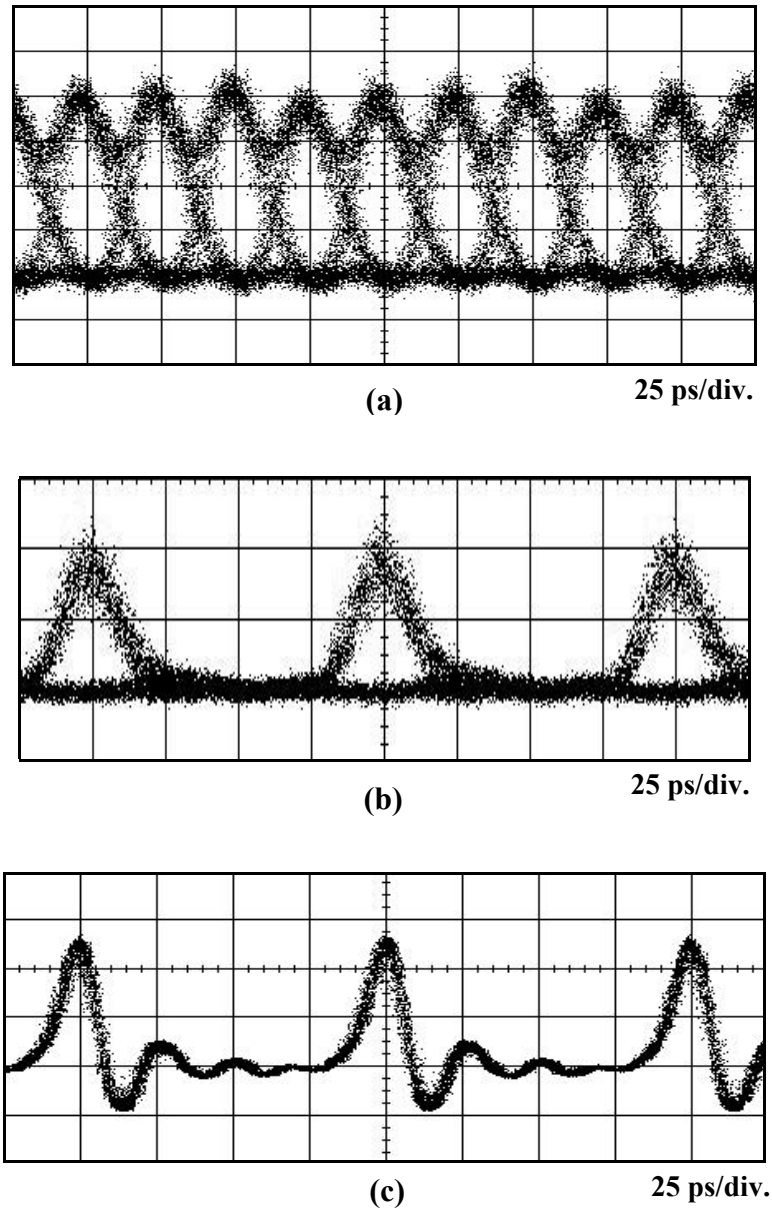

Fig. 5.3: (a) The eye diagram of the OTDM data at 40 Gbit/s. (b) The eye diagram of demultiplexed channel at 10Gbit/s (c) The optical recovered clock (10 GHz), using a 45GHz detector. The eye diagrams were taken using a 20 GHz detector.

Fig. 5.4 shows the RF spectrum of the recovered clock. It has a center frequency

at 10 GHz. The calculated phase noise is – 94.5 dBc/Hz at 250 KHz frequency offset. The r.m.s timing jitter calculated for the recovered clock using the clock RF spectrum is ≤ 200 fs.

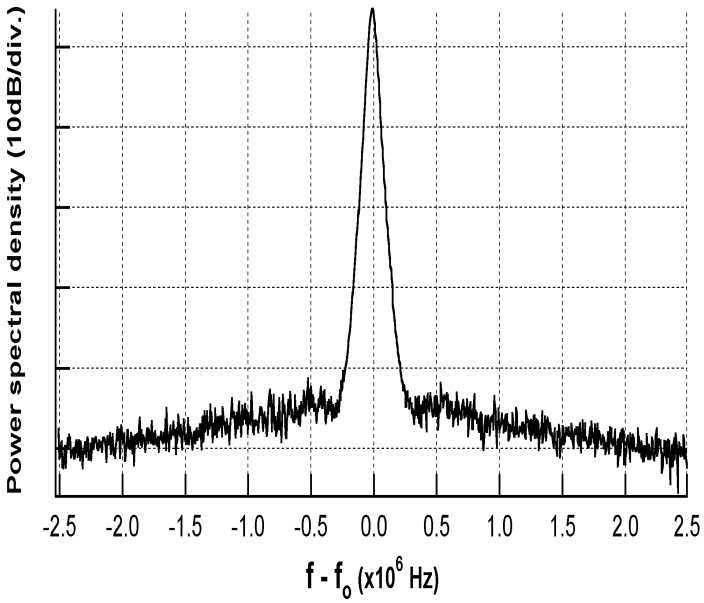

Fig. 5.4: The RF spectrum of the recovered optical clock, Resolution bandwidth = 50 kHz, f_o = 10 GHz.

Measurement of the BER versus received power of the 10 Gbit/s data is shown in Fig. 5.5. The data pattern is a 2^{31}-1 long PRBS. The measured receiver sensitivity is – 19.3 dBm at 10^{-9} BER as shown in the back-to-back case. The recovered clock was used to drive the error detector while measuring the demultiplexing BER. The demultiplexed 10 Gbit/s data showed an error free operation with a power penalty of 3.2 dB.

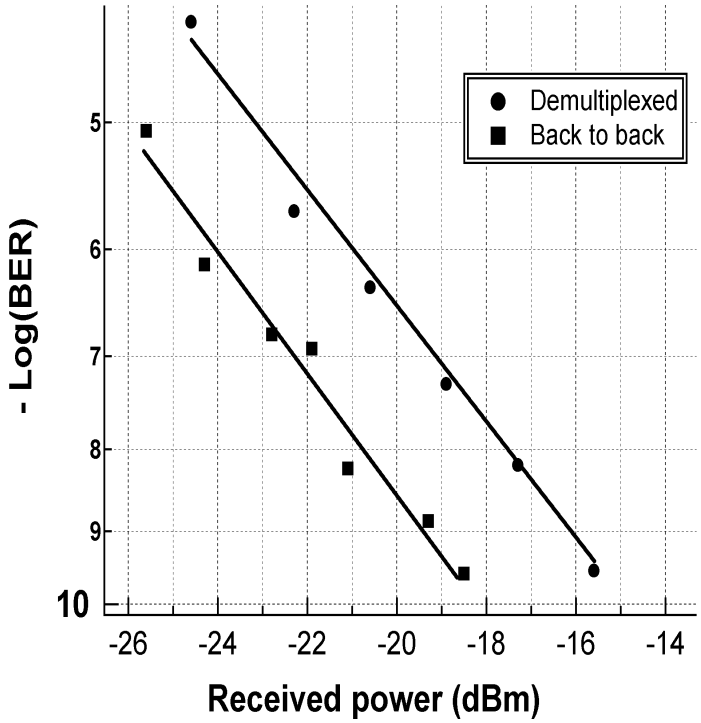

Fig. 5.5: The Bit-error- ratio measurement for optical demultiplexing from 40 Gbit/s down to 10 Gbit/s with simultaneous clock recovery.

In summary, we have demonstrated a technique for optical time demultiplexing with simultaneous all-optical timing extraction using a single EAM. The technique is based on counter-propagation between the clock and data optical pulses inside a single EAM. The system showed an error free operation and a small timing jitter (≤ 200 fs) for the recovered clock. The bit-error-ratio measurement for demultiplexing from 40 Gbit/s (2^{31}-1 PRBS) to 10 Gbit/s showed an error free operation with a 3.2 dB power penalty.

5.2 Optical 3R regeneration using a single EAM for all-optical timing extraction with simultaneous re-shaping and wavelength conversion

3R regeneration is considered a key-function for future long haul all-optical networks. It preserves data quality and allows for longer transmission distances [39], thus enhancing the transparency, scalability, and flexibility of optical networks [40]. Moreover, wavelength conversion is important to avoid wavelength blocking at optical networks nodes [40].

In this section we present a technique that utilizes a single EAM to perform simultaneous all-optical timing extraction, re-shaping, and wavelength conversion. As mentioned in chapter 4, the extracted timing is used to generate an error signal that is used to recover the optical clock. The same EAM is used to encode the incoming data onto the re-timed clock pulses in order to perform 3R regeneration and wavelength conversion. Conventional 3R regeneration techniques require at least two cascaded stages, one to perform timing extraction in order to recover the clock and the other to function as a nonlinear decision element [41].

Here in this technique the nonlinear optical transmission characteristic of the EAM under reverse bias allows for re-shaping of the degraded data, and at the same time all-optical timing extraction. Using the input data pulses as the control optical pump for the EAM, the input data pattern is encoded onto the clean, well-shaped, and

re-timed optical clock pulses, which already have a wavelength different than that of the data.

A counter propagation scheme between the clock and the data pulses inside the EAM is used to perform reshaping and timing extraction. Fig. 5.6 shows the measured nonlinear transmission of the EAM versus average input pump power, using a pump-probe technique at 1GHz repetition rate. The low optical transmission at small pump power allows noise suppression on zeros [16], while the transmission leveling off at high pump powers and small reverse bias (-2 v) reduces the amplitude noise on ones [42]. As mentioned earlier, the switching window of the EAM depends on the reverse bias and input power, as shown earlier in Fig. 2.5. For regeneration, the transmission window should be larger than the clock pulse width and smaller than the bit repetition period. Thus the data timing jitter, up to a certain level, is not transferred to the clock pulses and the shape of regenerated pulse will be the same as that of the clock pulse [43].

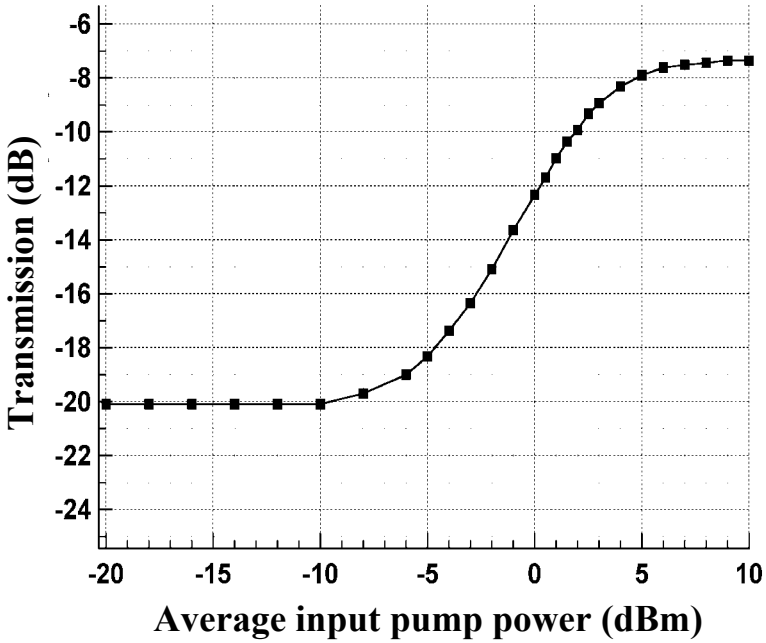

Fig. 5.6: The measured EAM transmission versus input average pump power at 2v reverse bias.

The all-optical timing extraction is performed using the time-dependent transmission characteristic of the EAM. As shown earlier in Fig. 4.1, the transmitted power from each side of the EAM is a function of the delay in arrival between two input counter-propagating pulse streams. Each pulse causes a fast saturation of the loss inside the EAM followed by a slow recovery time, hence, affecting the transmitted power of the next incoming counter propagating pulse based on its arrival time. Monitoring the optical outputs from both sides gives information about the amount of delay between the pulses and their precedence in arrival. Using a balanced detector, both output signals

are differential combined producing an electrical error signal, Fig. 4.2, which gives complete information about the timing error between the two counter-propagating pulse streams. As mentioned in section 5.1, The error signal controls the repetition rate of the clock pulses until it becomes equal to that of the counter-propagating pulse stream (data), and it maintains the timing delay between the two pulse streams at some fixed value (lock condition).

To achieve simultaneous 3R regeneration, the fixed delay value between the two-locked pulse streams can be slightly tuned by varying the electrical gain in the electrical feedback path until the clock pulses overlaps with the EAM transmission window that is produced by the data pulses. Thus, the data can be encoded onto the clock pulses during the lock condition and 3R regeneration is achieved.

Fig. 5.7 shows the experimental setup for optical 3R regeneration experiment. The data source has an actively mode-locked fiber laser producing RZ pulses at 10 GHz repetition rate with a 1545nm wavelength and a 3.3ps pulse width. A pattern generator and an electro-optic modulator are used to transcribe a 2^{31}-1 PRBS data onto the optical pulse stream. The optical clock pulses (RZ) were generated using an active-passive mode-locked semiconductor laser driven by a VCO running at 10GHz ± Δf. The clock pulses have a 3.3 ps pulse width with a wavelength of 1550 nm and an approximately 39 dB optical SNR as measured on an optical spectrum analyzer (OSA) with a 0.1 nm resolution bandwidth (RB). The two optical sources are completely independent and not

synchronized, so that when the feedback loop is open, both sources encounter a random shift in repetition rate and timing jitter with respect to each other.

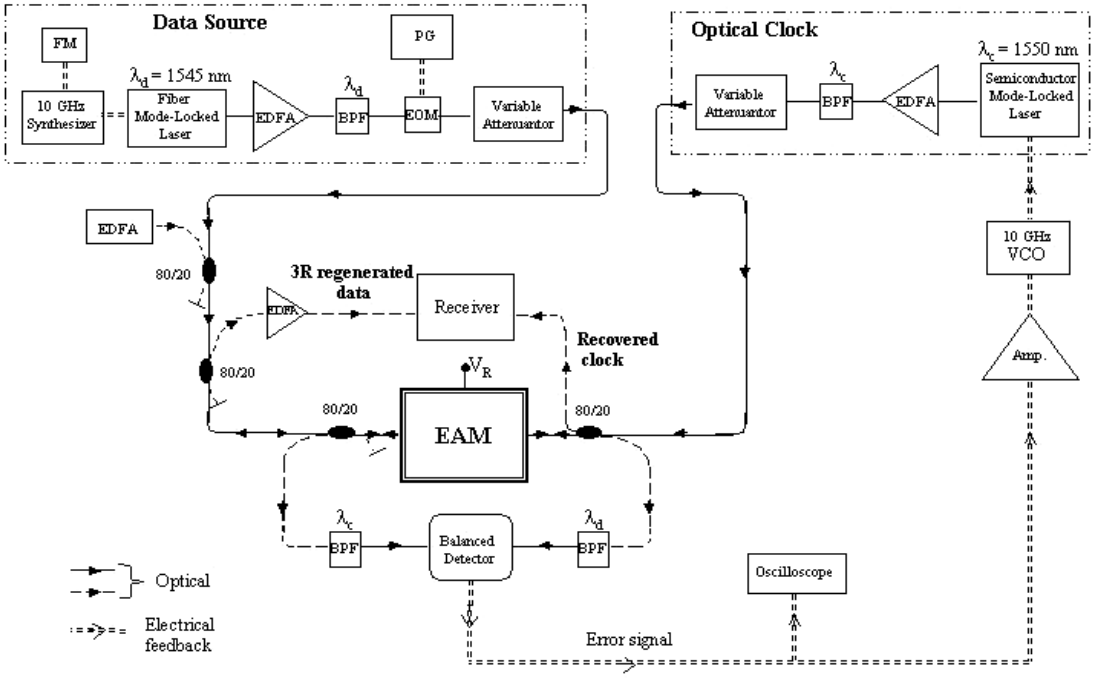

Fig. 5.7: Experimental setup for 3R regeneration with simultaneous optical clock recovery and wavelength conversion. PG: Pattern generator, BPF: Band pass filter, Amp: Electrical Amplifier, EOM: Electro-optic Mach-Zehnder modulator.

The input data average power to the EAM is set to 13.5 dBm (transmission window ≅ 30 ps, at –2v), while the clock average power is set to 3 dBm. The EAM reverse bias (V_R) is -2.3 volts. Each of the two outputs of the EAM was split off using an 80/20 coupler and then applied to the balanced detector inputs. The recovered clock

was split off using an 80/20 coupler before the EAM, while the 3R regenerated data was split off after the EAM using another 80/20 coupler. The low pass filtering of the slow balance detector helps to eliminate the high frequency jitter (>100KHz) from being transferred to the clock pulses, while the PLL configuration tolerates the low frequency jitter (<100KHz), in order to maintain locking with the data. As mentioned earlier, The measured back reflection from the fiber pigtailed EAM is approximately -40dB, thus the back reflection does not disturb the propagating pulses, and the polarization sensitivity of the EAM is < 1 dB.

Fig. 5.8.a shows a histogram of the eye diagram for the degraded input data. The amplitude noise is introduced by adding a broadband ASE noise using an EDFA, while the timing jitter is introduced by applying a frequency modulation (FM) to the input data, with a frequency of 500KHz (arbitrary chosen >100KHz) and an amplitude equals approximately to a half pulse width. The optical SNR of the degraded data was measured to be 18 dB on an OSA with a 0.1 nm RB. This optical SNR is close to the minimum requirement for 10 Gbit/s transmission, and it was obtained by injecting the maximum available ASE noise power. Fig. 5.8.b shows a histogram of the eye diagram for the 3R-regenerated data. The suppression of the amplitude noise and timing jitter results in a clear eye opening similar to that of the clean data with a 38 dB optical SNR. The r.m.s timing jitter calculated for the recovered clock using the clock RF spectrum is ≤ 230 fs. Fig. 5.9 shows the 3R-regenerated data (upper trace) with simultaneously recovered optical clock (lower trace) at 10 GHz.

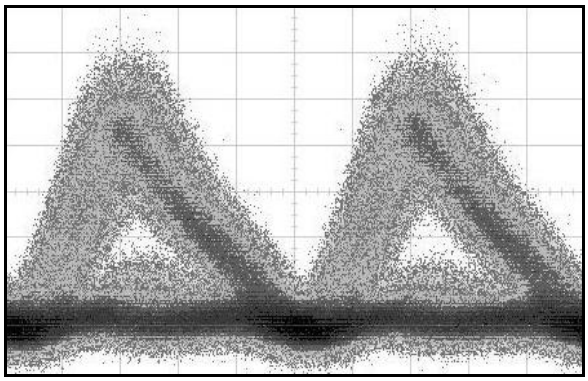

20 ps/div. **(a)**

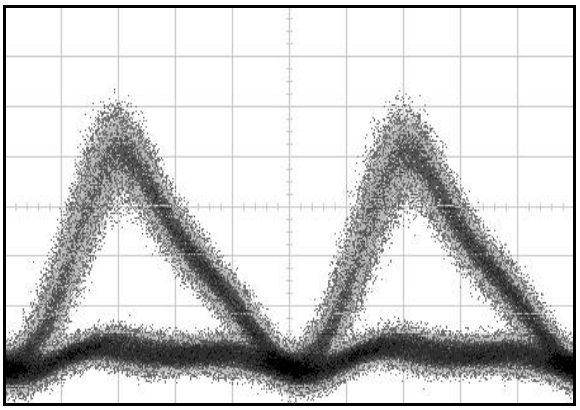

20 ps/div. **(b)**

Fig. 5.8: (a) The eye diagram of the degraded input 2^{31}-1 PRBS data, 10 Gbit/s. (b) The eye diagram of 3R-regenerated data. The eye diagrams were measured using an optical communication analyzer with a built-in SONET/SDH electronic low-pass filter with a cut-off frequency of 7.465 GHz.

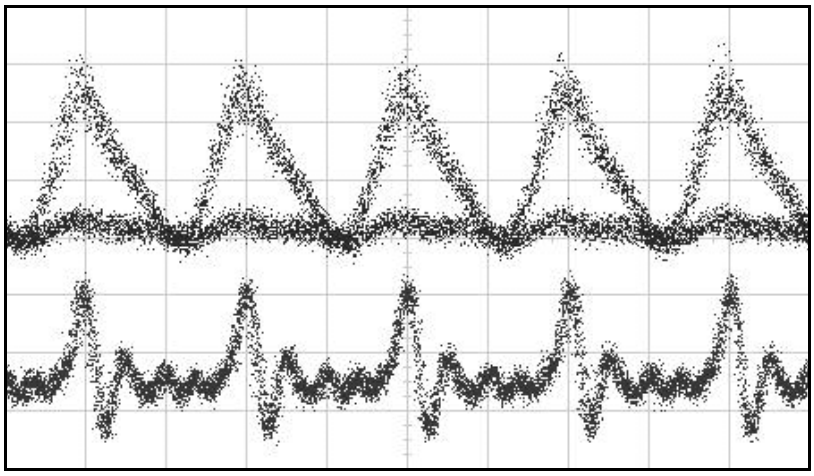

Fig. 5.9: The 3R-regenerated 2^{31}-1 PRBS data (upper trace), simultaneously optical recovered clock at 10 GHz (lower trace).

Measurements of the BER, shown in Fig. 5.10, were performed to investigate the system performance. The input data is a 2^{31}-1 PRBS, running at 10 Gbit/s. The receiver is a PIN photo-receiver with optical pre-amplifier. The measured receiver sensitivity is –19.4 dBm at 10^{-9} BER. The power penalty of the degraded data is + 6.4 dB with respect to the back-to-back case. The BER of the 3R-regenerated data was measured using the recovered clock to drive the error detector. The 3R-regenerated data showed an error-free operation with a negative power penalty of 4.7 dB with respect to the degraded data and a positive power penalty of 1.7 dB with respect to the back-to-back case. No error floor has been observed up to the maximum available output power at the receiver.

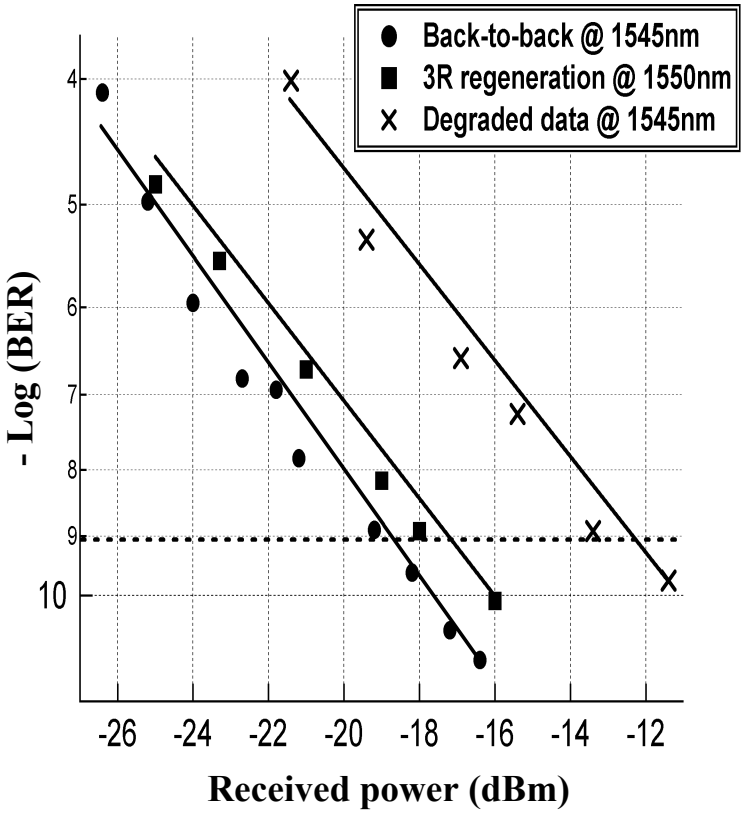

Fig. 5.10: The bit-error- ratio measurement using a 2^{31}-1 PRBS data running at 10 Gbit/s.

In summary, we have developed a technique for performing simultaneous all-optical timing extraction, re-shaping and wavelength conversion using a single EAM. The technique is used to perform 3R regeneration. The system performance was tested using 2^{31}-1 PRBS data running at 10Gbit/s with a 3.3 ps pulse width. The input data was degraded by adding a 500 KHz timing jitter and reducing the optical SNR to 18 dB. The system showed a 4.7 dB improvement in the power penalty, and less than 230 fs of timing jitter for the recovered clock. The same performance is expected for longer

pulses given that they have sufficient peak power to saturate the loss inside the EAM. For example, 10 ps pulses require about 4.8dB increase in the input average power to obtain the same peak power as that used in this experiment. Also, this technique has the potential to operate at higher bit rates, 40 Gbit/s, because of the small EAM transmission window that can be achieved. However, more input power is needed to achieve the required EAM nonlinear transmission characteristic for reshaping at higher bit rates, which might be above the damage threshold of the device.

Chapter 6

Four-wave mixing in EAM and SOA

6.1. Four-wave mixing process in semiconductors

In the Four-wave mixing (FWM) process, an optical pump input at ω_o is launched into a semiconductor wave-guide together with a probe signal at ω_1. The two signals (pulses or CW) are co-polarized and co-propagating along the waveguide. The electric fields of the two signals interfere and modulate at the beat frequency $\Omega = \omega_1 - \omega_o$. This modulation creates dynamic index and gain/absorption (SOA/EAM) gratings moving inside the active region of the wave-guide, which scatter some of the pump power at a new optical frequency $\omega_2 = \omega_o - \Omega = 2\omega_o - \omega_1$. This new generated signal is called FWM signal or conjugate signal. In SOAs the carrier dynamics includes carrier population modulation, spectral-hole burning, and carrier heating. The first process involves inter-band transitions between the conduction and valence bands, and the associated carrier lifetime is in the order of few hundreds of picoseconds. While the two latter processes are intra-band and has a lifetime in the order of few hundreds of femto seconds [44]. In EAMs the processes resulting in FWM are not well understood, but as it will be shown in this section, there are also fast and slow processes.

FWM is one of the important nonlinear optical operations for high-speed optical

signal processing due to its ultra-fast response. The FWM switching window is typically on the order of a pulse width and depends on the temporal overlap between the pump and probe pulses inside the medium. Also, FWM is modulation format independent; it applies to any data modulation format including amplitude, phase, and frequency modulation.

In this section we will describe the nondegenerate ($\omega_o \neq \omega_1$) FWM process in semiconductor wave-guides using analytical equations. The following equations describe the FWM process in SOAs [45] or EAMs. In case of EAM, it can be treated as a saturable absorber with a negative gain coefficient, and in case of SOA the gain coefficient is positive. The electric field describing the co-propagating waves along 'z' direction can be described by:

$$E_j(z,t) = E_j(z)\exp[i(k_j z - w_j t)]$$

Where j = p, b, s indicates pump, probe, and FWM signal respectively. Following procedures similar to those in [46], the coupled-amplitude equations can be derived [45].

$$\frac{dE_{p,b}(z)}{dz} = \frac{1}{2}\left(\frac{g_o}{1+P(z)/P_{sat}}(1-i\alpha)-\alpha_1\right)E_{p,b}(z)$$

$$\frac{dE_s(z)}{dz} = \frac{1}{2}\left(\frac{g_o}{1 + P(z)/P_{sat}} (1 - i\alpha) - \alpha_l \right) E_s(z) - \kappa(z) E_p^2(z) E_q^*(z) \exp(i\Delta z z)$$

Where $\Delta k = 2k_p - k_b - k_s$ is the wave-number mismatch, g_o is the unsaturated optical gain/loss per unit length, P_{sat} is the saturation power, α is the line-width enhancement factor, α_l is the SOA internal loss per unit length, and $\kappa(z)$ is the FWM coupling coefficient given by:

$$\kappa(z) = \frac{1}{2} \frac{g_o}{1 + P(z)/P_{sat}} \sum_{m=1}^{3} \frac{1 - i\alpha_m}{1 - i\, 2\pi f \tau_m} \cdot \frac{1}{P_m}$$

Where m=1,2, or 3 represents the process of carrier density modulation, dynamic carrier heating, and spectral hole burning, respectively, in case of SOA. For the EAM case, it will represent each of the processes above that are responsible for the FWM process. Unfortunately, due to the complex interactions of the electro-absorption effect (bandgap shift), carrier dynamics, and the dynamics of the local electric field (field screening and recovering), we do not yet have a complete physical model of the FWM process in EAM. Detail understanding of the physics involved in the FWM process in EAM will be considered in the future work. Returning to the equation for $\kappa(z)$, '*f*' is the detuning frequency, τ_m is the life time of each mechanism, P_m is the saturation power, α_m is the ratio between real and imaginary parts of refractive index change.

Solving the coupled wave equations using the boundary condition $E_s(0)=0$, we get:

$$E_s(l) = -\frac{\kappa(l) l \exp[i\Delta k l]}{i\Delta k + \int_0^l \left(\frac{g_o}{1+P(z)/P_{sat}} - \alpha_1\right) dz} \cdot E_p^2(l) E_b^*$$

Hence, the FWM conversion efficiency is:

$$\eta = \frac{P_s(l)}{P_b(0)} = G^3 P_p^2 \cdot R(\Delta\lambda) \qquad (17)$$

Where $G = \int_0^l \left(\frac{g_o}{1+P(z)/P_{sat}} - \alpha_1\right) dz$ is the SOA saturated gain

And $R(\Delta\lambda) = \left| \sum_{m=1}^{3} \frac{g_o l}{2G(1+P(z)/P_{sat})} \cdot \frac{1-i\alpha_m}{1-i2\pi f\tau_m} \cdot \frac{1}{P_m} \right|^2$ is the wavelength detuning factor.

Typical values of SOA parameters are: τ_1 =100 ps, τ_2 =650 fs, τ_3 =50 fs, α =12 cm^{-1}, α_m= 4, g_o= 5000 cm^{-1}, P_{sat} =5 dBm, G =15 dB. Typical values of EAM parameters are: $|\alpha_m| < 1$, τ_1 can be interpreted as the phenomenological carrier decay time which relates to the absorption recovery time that depends on the reverse bias and the input

optical power as mentioned earlier, and it can vary from 10ps up to 100ps, g_o can vary from -115 to –575 cm^{-1} depending on the reverse bias.

In the following section, we describe experimental results on four-wave mixing in EAM under reverse bias and with wavelength detuning, and compare it with SOA. This will be followed by discussion on experiment of optical demultiplexing using FWM in EAM with simultaneous clock recovery at 80 Gbit/s.

6.2. Characterization of four-wave mixing in electroabsorption modulator and its application to ultra-fast optical signal processing

The FWM in SOAs and optical fibers have been already demonstrated. For example, optical demultiplexing from 160 Gbit/s [15], 160 Gbit/s optical sampling by gain-transparent FWM in SOA [47], and optical demultiplexing from 40 Gbit/s using FWM in dispersion-shifted fiber [48].

Although SOA usually has higher FWM conversion efficiency than EAM due to its internal gain, we observed that the FWM in EAM has a wider wavelength detuning range and the reverse bias of EAM enhances the FWM efficiency. Using picosecond optical pulses as pump and probe, the FWM conversion efficiency in EAM was characterized. It was observed that the efficiency is relatively low at small wavelength detuning of the pump and probe but increases at large detuning until it becomes almost

constant. This behavior is completely different from that of SOA, in which the efficiency reduces with more detuning and always increases with higher forward current.

Fig. 6.1.a shows the optical spectrum of the pump, probe, blue-shifted (1540.2 nm) and red-shifted (1568.9 nm) conjugate signals. The pump and probe are co-propagating along the EAM waveguide. A polarization controller was used to co-polarize the pump and probe signals and an optical delay line is used to adjust the delay between the pump and probe at the EAM input in order to maximize the FWM conversion efficiency. The pump wavelength is 1559.3 nm with a 10 dBm average input power at 10 GHz repetition rate and a 3.3 ps pulse width. The pulsed probe is a 10-GHz pulse train with a fixed wavelength at 1549.5 nm (4 ps pulse width) and 10dBm average input power. The EAM reverse bias is set to zero volts. The measured OSNR of the blue-shifted and red-shifted FWM signals are 16.5 and 14.5 dB respectively. The two conjugate signals have approximately same conversion efficiency (≈ 0.05%), unlike FWM in SOA where the blue-shifted conjugate usually has a higher efficiency than the red-shifted one [45]. We also note that reverse bias introduces more loss to the blue-shifted signal than the red-shifted one due to the EAM absorption-edge shift toward longer wavelength, which introduces higher absorption at shorter wavelengths. Fig. 6.1.b shows the wide detuning range in EAM, about 25 nm, for both the red-shifted and blue-shifted FWM signals. In this case, the input average power for each of the pump

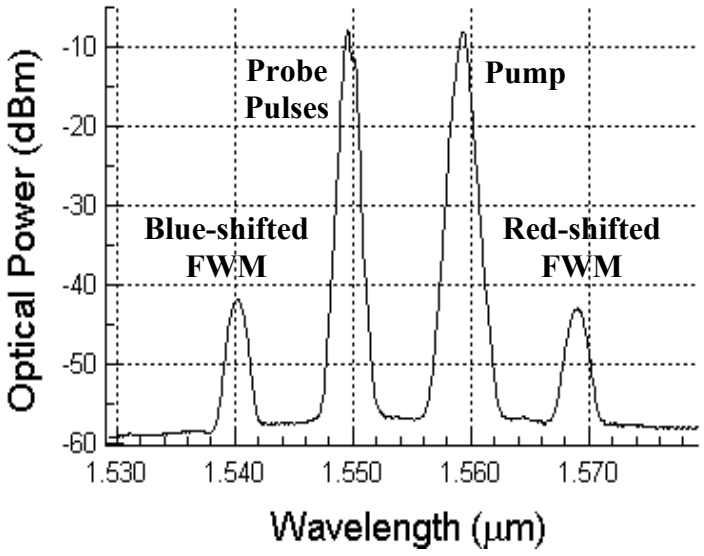

(a)

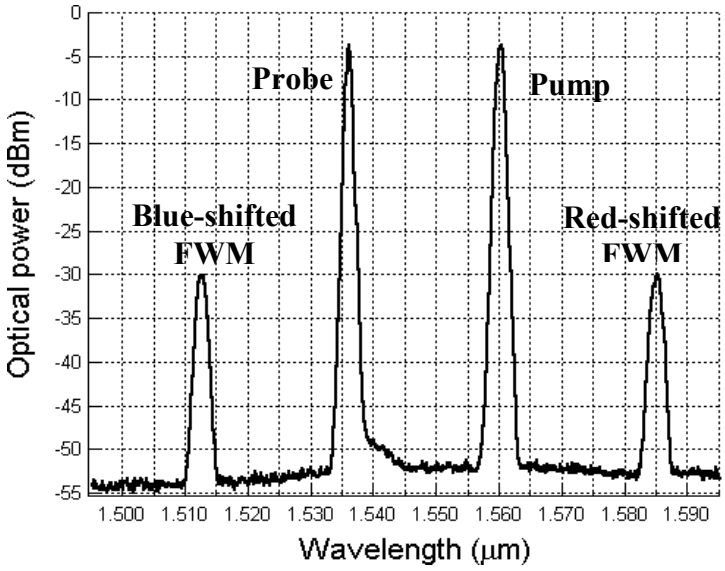

(b)

Fig. 6.1: The measured optical spectrum of the pump, pulsed probe, and FWM signals. The resolution bandwidth is 0.1 nm, and the reverse bias is zero. (a) The wavelength detuning is 10 nm. (b) The wavelength detuning is 25 nm.

and probe is 14 dBm. The measured detuning-range of the EAM in this experiment is limited by the gain bandwidth of the EDFA used to amplify the pump and probe signals and the tuning range of the band-pass filter. We note that the two conjugate signals have the same optical power, and the measured OSNR of the FWM signals is about 23 dB.

Fig. 6.2 shows the output power of the pump, probe, and red-shifted FWM signals measured at different reverse bias on an optical spectrum analyzer (resolution bandwidth = 0.1 nm). The repetition rate of the pump is 10 GHz and has a wavelength of 1552.41 nm. The 10-GHz probe pulse train has a wavelength of 1547.58 nm. Each of the pump and probe signals has a 14 dBm average input power. The FWM signal wavelength is measured at 1557.03 nm (red-shifted) and 1542.89 nm (blue-shifted). The FWM power increases by 2 dB between zero and 0.7 volts reverse bias for the red-shifted FWM and then it levels off. While the blue-shifted FWM signal increases by 1.5 dB between zero and 0.4 volts, and then it starts to drop. This drop is due to the EAM bandgap-edge shift to longer wavelength with higher reverse bias. For the pump and probe, the output powers decreases with increasing reverse bias, as expected. We believe the reason for FWM power increase with reverse bias is the following: The reverse bias increases the absorption coefficient inside the EAM, which in turn enhances the nonlinear interaction between the pump and probe and also reduces the carrier sweep-out time; and consequently increases the FWM efficiency. However, beyond ≈ 0.7 volts the pump and probe powers start to attenuate significantly which counteract on the pump-probe nonlinear interaction enhancement and eventually

balances the increase in the FWM efficiency until it levels off, such as the case of the red-shifted FWM signal as can be seen in Fig. 6.2.

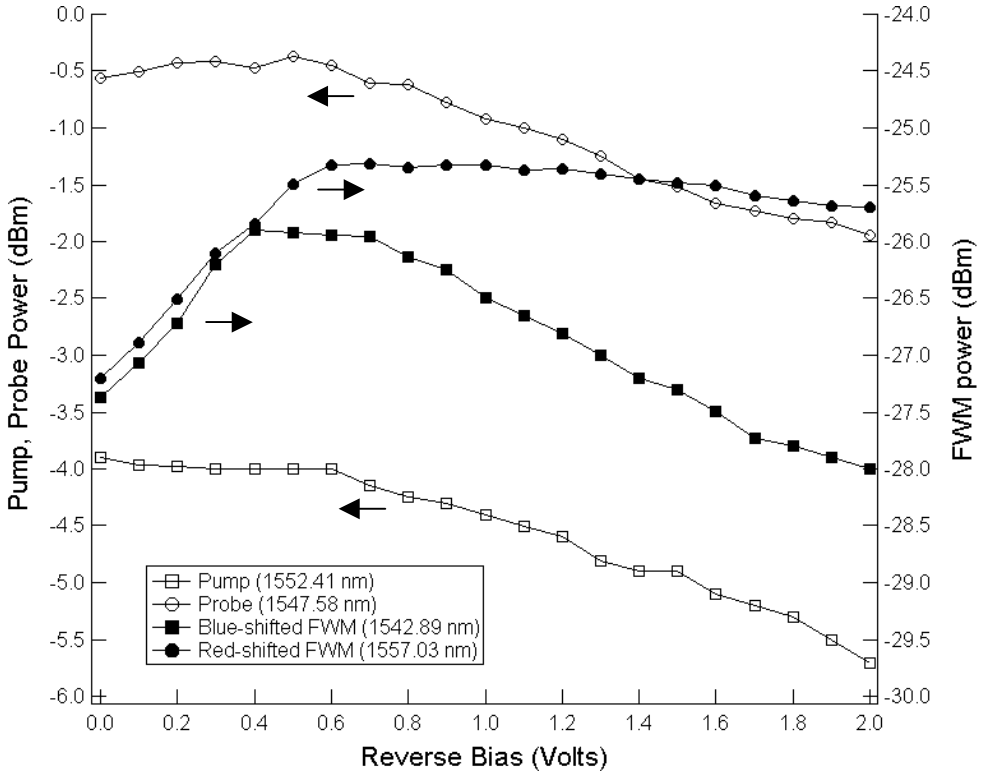

Fig. 6.2: The pump, probe, and red-shifted FWM output power at different reverse bias, using 10 GHz probe pulses.

Fig. 6.3.a shows the FWM efficiency of EAM at different reverse biases as a function of wavelength detuning. The pump wavelength is 1536.1 nm and the probe is detuned from 1540.23 nm up to 1560.38 nm. The efficiency here is defined as ratio of

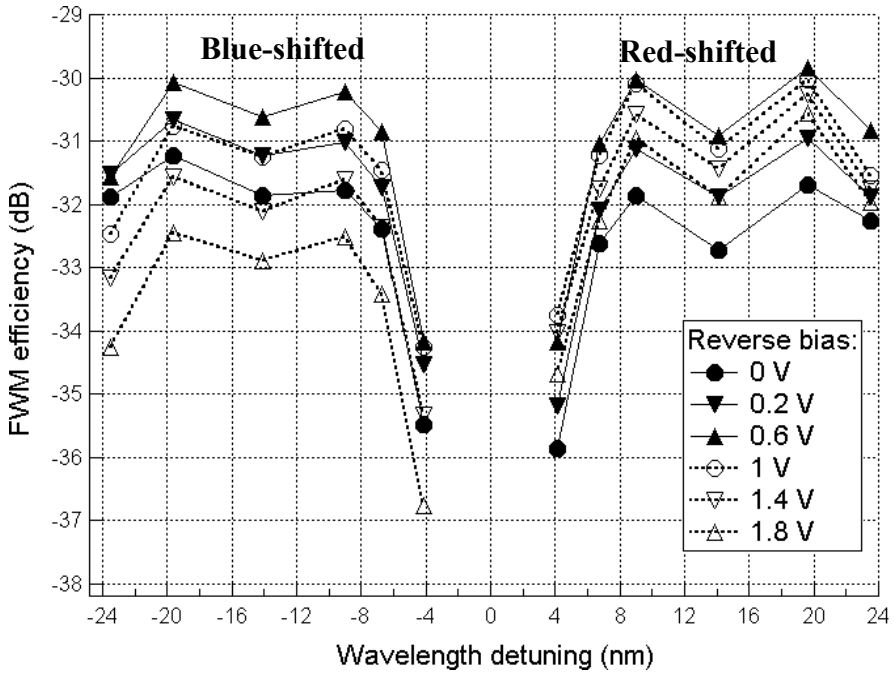

(a)

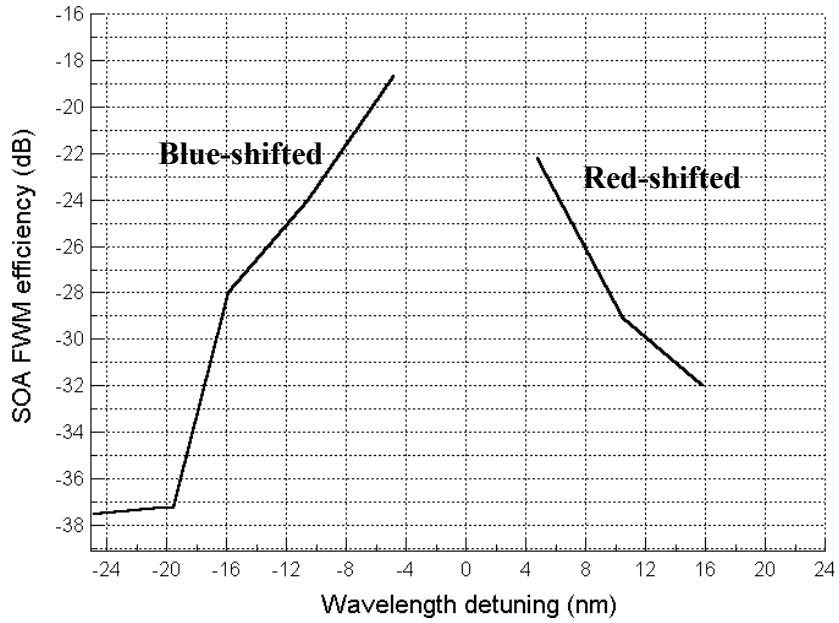

(b)

Fig. 6.3: (a) The FWM efficiency versus wavelength detuning at different reverse bias. (b) The measured FWM efficiency in SOA using 10 GHz pump and probe signals.

the output FWM power to the input probe power. The efficiency increases with detuning and becomes almost constant beyond 10 nm. The reverse bias between zero and 0.6V increases the efficiency by about 1.86 dB for the red-shifted conjugate, and 1.3 dB for blue-shifted one. Beyond 0.6V the blue-shifted FWM attenuates more than the red-shifted one because of EAM bandgap shifts to longer wavelength. Above 0.6V, the pump and probe powers start to attenuate significantly, as mentioned earlier in page '106', however in this case the attenuation overcomes the enhancement from the reverse bias and the FWM signal power starts to decrease.

Fig. 6.3.b shows the FWM efficiency for SOA at 120 mA forward current. The SOA utilized in this experiment is a InGaAsP-based device [21], it has a 20 dB small signal gain at 120 mA of forward bias current. The pump is at 1555.3 nm and the probe is detuned from 1550.3 nm down to 1535.5 nm. The blue-shifted FWM has higher efficiency and can be detuned by 24 nm, while the red-shifted FWM has a lower efficiency and can be detuned by 16 nm only. The efficiency always increases with higher forward current, as the internal SOA gain increases. The limited detuning range of the red-shifted FWM signal in case of SOA is due to the ASE noise that reduces the OSNR of the FWM signal and eventually masks it. Although, the EAM has always a lower FWM efficiency than SOA due to the SOA internal gain, the EAM shows a wider detuning range for both red-shifted and blue-shifted FWM signals. Even though the FWM signal in EAM is relatively weak, a high gain EDFA with low noise figure can be used to bring the FWM signal to a higher power level with reasonable OSNR, as demonstrated in the next section.

Fig. 6.4 (a & b) shows the FWM efficiency at different detuning wavelengths as a function of reverse bias for blue-shifted and red-shifted FWM signals, respectively. In Fig. 6.4.a, the enhancement in blue-shifted FWM signal is 1.74 dB measured at 1531.95 nm between zero and 0.8V, and it is 0.8 dB measured at 1512.6 nm between zero and 0.4V. In Fig. 6.4.b, the enhancement in the red-shifted FWM signal is 2.11 dB measured at 1544.66 nm between zero and 1V, and it is 1.5 dB measured at 1584.9 nm between zero and 0.8V. These results indicate that the enhancement in FWM efficiency with reverse bias reduces with higher detuning.

In order to qualititively explain the FWM variation with detuning in EAM, we can assume that there are a slow and fast processes which are interfering destructively, and they have opposite signs. Therefore, for small detunings where both processes are relevant the conversion efficiency is less than that for higher detunings where only the fast process is important.

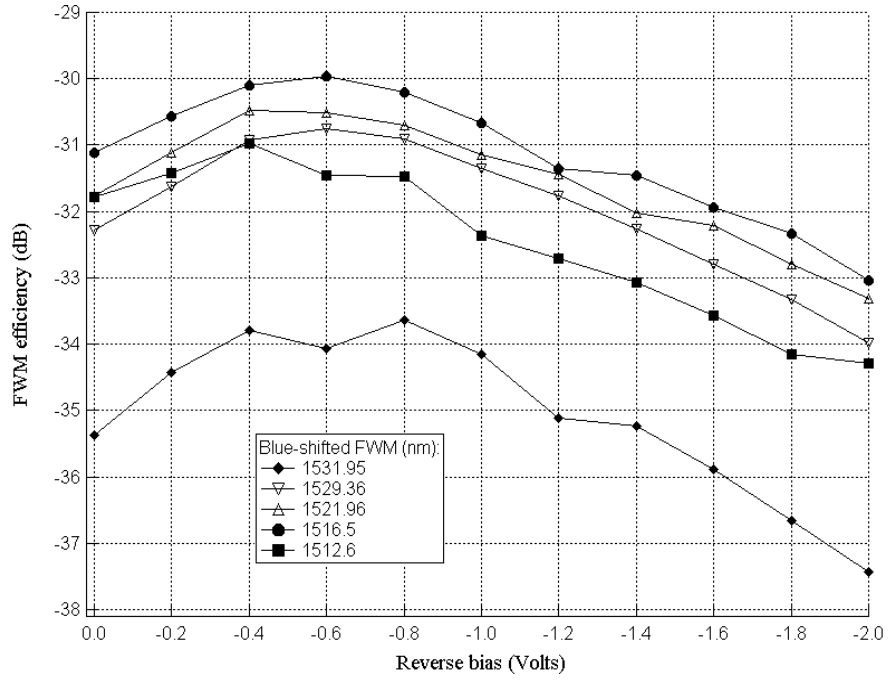

(a)

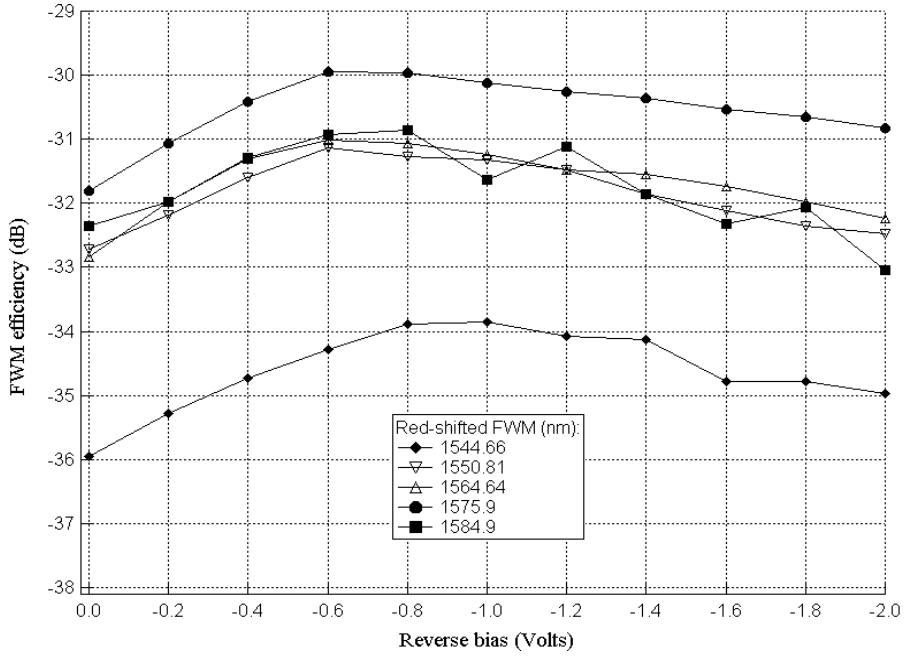

(b)

Fig. 6.4: The FWM efficiency at different wavelength detuning as a function of reverse bias: (a) The blue-shifted FWM signal, (b) The red-shifted FWM signal.

To measure the switching window of the FWM signal in the EAM, we offset the repetition rate between the pump (3.5 ps) and probe (4.5 ps) pulses by 10 KHz. A slow detector was used to measure the output FWM signal power. Fig. 6.5.a shows the measured switching window with ≈ 5.3 ps FWHM, which should be adequate for demultiplexing up to 160 Gbit/s (pulse separation: 6.25 ps). Fig. 6.5.b shows the simulation results for the switching window FWHM as a function of different pump and probe pulses widths. In this model we assumed a Gaussian pulse shape for the probe pulses and sech^2 for the pump pulses, and the FWM power is calculated from eq. (17) by using the following simple formula where phase matching was assumed:

$$P_s \quad \alpha \quad P_p^2 * P_b$$

'P_s' is the output FWM signal power, 'P_p' is the input pump power, and 'P_b' is the input probe signal power.

Assuming low input powers, the model is in a good agreement with the measured data. It shows that sufficiently short input optical pulses (≈ 1ps) can produce a short switching window ≈1.2 ps, which is appropriate for signal processing up to 640 Gbit/s.

Fig. 6.5.c illustrates the measured switching window width at different input pump power. We observed that the switching window width is constant (5.3 ps) up to

7dBm and then it starts to increase with higher input powers. It increases by about 700 fs between 7 and 10 dBm. We believe that this increase is mostly due to some pulse reshaping by EAM absorption saturation at high input powers, which affects the temporal overlap between the pump and probe pulses and thus the switching window width.

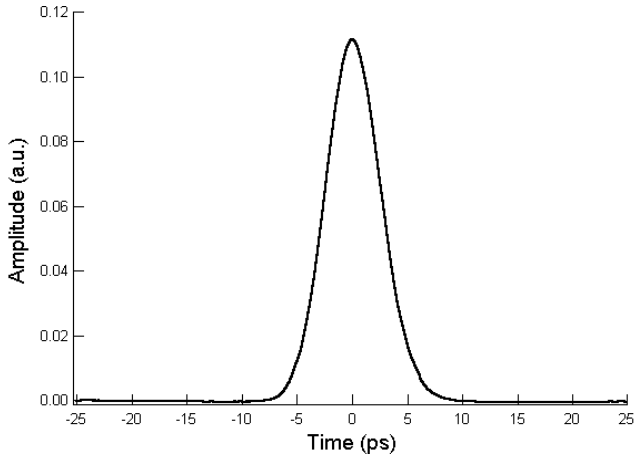

(a)

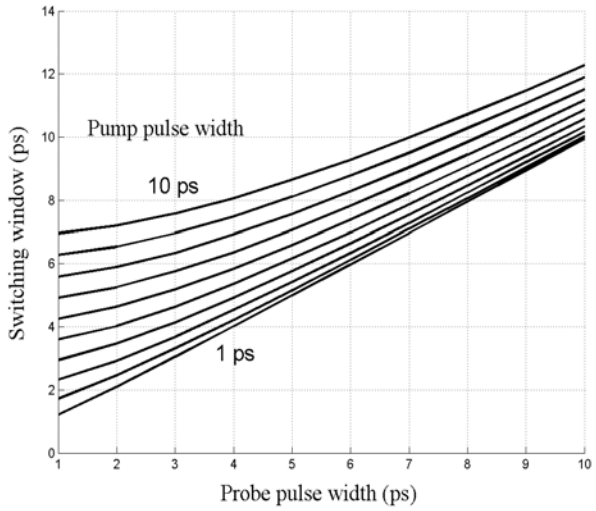

(b)

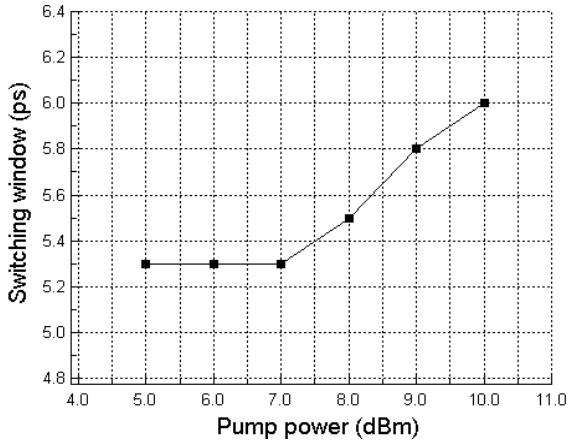

(c)

Fig. 6.5: (a) The measured FWM switching window at 7 dBm input pump power. (b) The simulated switching window as a function of pump and probe pulse-width. (c) The measured FWM switching window at different input pump power. The pulses width of pump and probe signals are 3.5 and 4.5 ps, respectively.

In summary, we have investigated FWM in EAM and compared it with SOA. We demonstrated that FWM has a wide tuning range of ≈25 nm limited by the EDFA gain bandwidth and band pass filters tuning range. We also demonstrated that the FWM efficiency curve as a function of wavelength detuning in EAM behaves very differently from that of the SOA. In addition, we showed that a ≈ 0.7-volt of reverse bias could improve the FWM efficiency in EAM by 2 dB.

6.3. Simultaneous 80 Gbit/s optical demultiplexing and clock recovery using four-wave mixing and co-propagation timing extraction inside a single electroabsorption modulator

In this section we describe a novel technique that uses a single EAM to perform two simultaneous operations: All-optical timing extraction using fast absorption-saturation, and optical demultiplexing using FWM. We use co-propagating data and clock pulses for timing extraction in the EAM, which provides clock recovery at 10 GHz. The optical demultiplexing and simultaneous clock recovery is performed at 80 Gbit/s.

As mentioned earlier, the high-speed optical timing extraction and signal processing are essential for ultra-high speed networks to perform synchronous operations such as demultiplexing and regeneration. Four-wave mixing is one of the promising nonlinear all-optical techniques for ultra-fast signal processing. In addition, fast time-dependent absorption-saturation inside EAM can be used for ultra-fast optical timing extraction. Different techniques have been already reported on ultra-fast clock recovery using interferometric switches based on SOA [5], or RF-driven EAMs in conjunction with electronic mixer [6]. In chapter 5, we have described simultaneous clock recovery and demultiplexing at 40 Gbit/s using absorption saturation and counter-propagating between data and clock pulses inside EAM. We also showed in chapter 4 that the counter-propagating clock and data pulses inside a single EAM could be used to perform ultra-fast optical clock recovery up to 160 Gbit/s.

Here, we demonstrate simultaneous FWM and timing extraction inside a single EAM using co-propagation between the data and clock pulses. A novel technique was developed that uses the EAM to achieve high-speed retiming and demultiplexing at the same time. The co-propagating configuration allows us to perform timing extraction and FWM between the data and clock pulses simultaneously. The extracted timing is capable of resolving sub-picosecond timing error between the data and clock pulses due to the fast absorption-saturation inside the EAM, while the FWM allows for small switching window (≈ 6ps) despite of the relatively slow absorption recovery time of the device (≈ 30ps in this experiment) that is limited by the carrier dynamics.

Fig. 6.6 shows the experimental setup for simultaneous optical clock recovery and demultiplexing from 80 Gbit/s. The optical return-to-zero data pulses (1547.93 nm) have a pulse width of 4.5 ps FWHM, and they are running at 10Gbit/s with 2^{31}-1 long PRBS. The 10 Gbit/s data pulses are multiplexed using a multi-stage passive fiber delay-and-add line, similar to that in Fig. 4.10, to obtain an aggregate bit rate of 80 Gbit/s. The optical delay line and the polarization controller are utilized to adjust the delay and polarization of the data to maximize the FWM efficiency. The RZ optical clock pulses (1553.86 nm) have a pulse width of 3.5 ps FWHM, and they are generated using a mode-locked semiconductor laser driven by a VCO running close to 10GHz. The data and clock were launched to co-propagate inside the EAM each with a 14dBm average input power. A 90/10 splitter is used to split 10% of the data and clock power after the first EDFA. Then the 10% power is split again using a 50/50 splitter into two

branches, each with a BPF (1547.93 nm, and 1553.86 nm). A balanced photo-detector (1 MHz bandwidth) detects the two optical signals (data & clock) and generates a low-pass filtered electrical error signal. This error signal is fed back to control the repetition rate of the semiconductor mode-locked laser (clock) until it locks to one of the incoming data channels. The other 90% of the output power is amplified and filtered using a 2nm BPF at 1559.78 nm to obtain the FWM signal output.

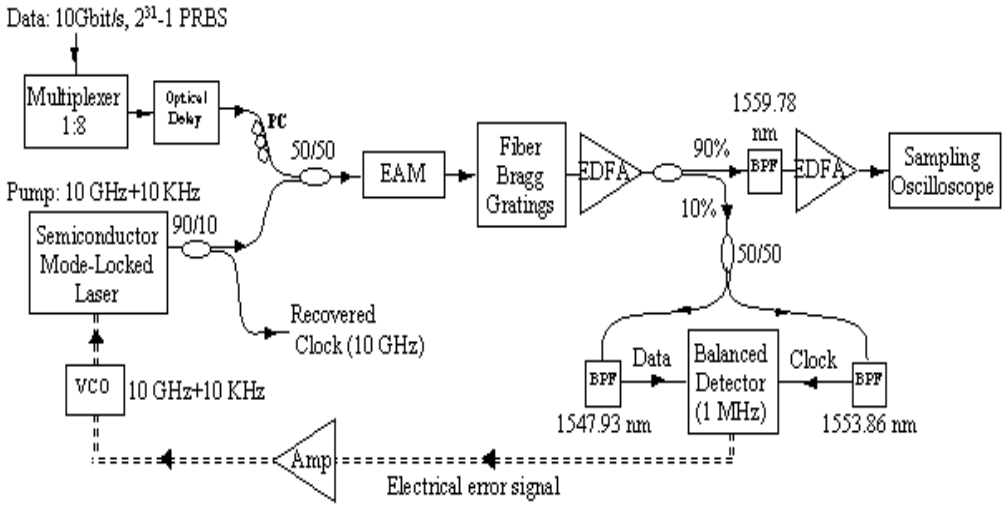

Fig. 6.6: The experimental setup for optical clock recovery and demultiplexing. PC: Polarization Controller, BPF: Band Pass Filter, EDFA: Erbium Doped Fiber Amplifier, Amp: Electrical Amplifier, VCO: Voltage-Controlled Oscillator.

Since increasing the reverse bias introduces higher attenuation to the blue-shifted FWM signal compared to the red-shifted one, we chose the red-shifted FWM

signal as the demultiplexed 10 Gbit/s data. Fig. 6.7 shows the output power of the pump, probe, and red-shifted FWM signals measured at different reverse biases on an optical spectrum analyzer (resolution bandwidth = 0.1 nm). In this case, the probe is 80 Gbit/s RZ pulses modulated with 2^{31} -1 long PRBS, and it has a wavelength of 1547.93 nm.

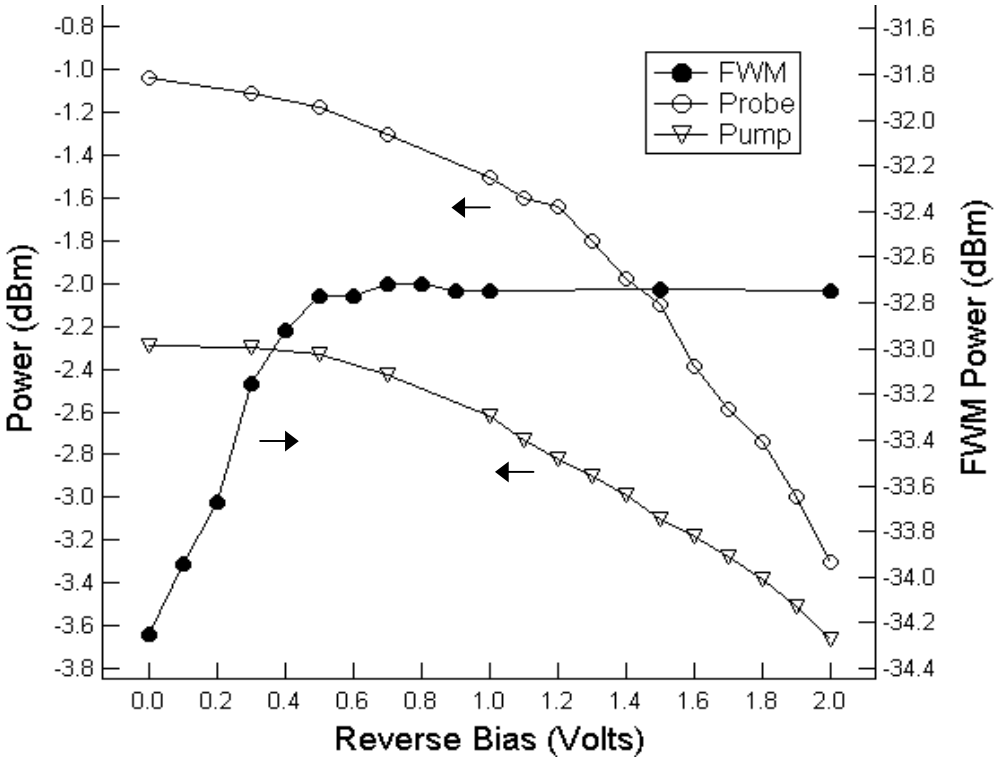

Fig. 6.7: The pump, probe, and red-shifted FWM output power at different reverse bias, using an 80 Gbit/s, 2^{31}-1 PRBS probe signal.

The pump is running at 10 GHz and it has a wavelength of 1553.86 nm. Each of the pump and probe has a 14 dBm average input power. The FWM signal wavelength is measured at 1559.78 nm (red-shifted). The FWM power increases by 1.5 dB between zero and 0.5 volts, and then it levels off. That corresponds to increase in conversion efficiency from 0.097% to 0.14%. The conversion efficiency is defined here as the ratio of the FWM output to input data peak power. For the pump and probe, the output powers attenuate with higher reverse bias, as expected.

Fig. 6.8 shows the output optical spectrum after the first EDFA, which is a low-noise pre-amplifier with a noise figure ≈ 3.5 dB. In order to extract more gain for the FWM signal, two fiber-Bragg gratings (0.1 nm bandwidth) were used to suppress some of the transmitted data and clock powers. The data grating has a 30 dB reflectivity at 1547.83 nm and the clock grating has a 26 dB reflectivity at 1553.59 nm. Unfortunately, the available gratings at that time had such small bandwidth. Using larger bandwidth gratings will supress more power from the transmitted data and clock and allow the FWM to extract more gain from the pre-amplifier. The output FWM signal here has a 15.8 dB optical signal-to-noise ratio. The FWM average power measured directly after the EAM output is about –34 dBm. The calculated conversion efficiency defined as the ratio of FWM output to input data peak power is about 0.1%.

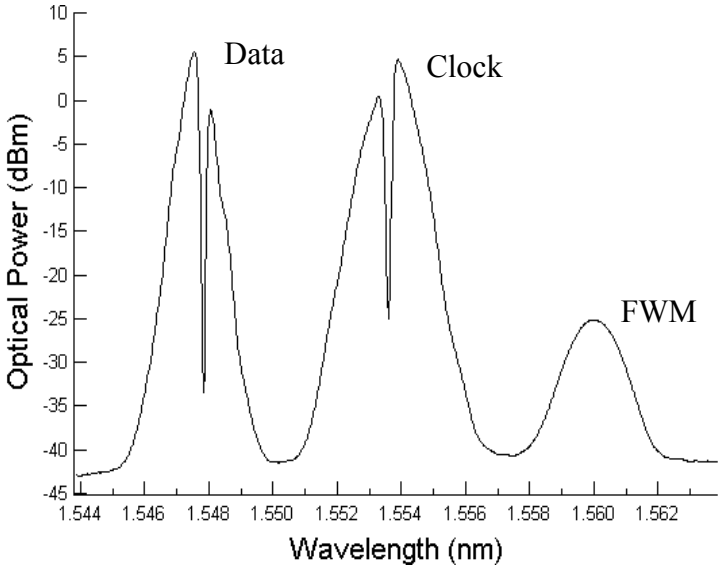

Fig. 6.8: The optical spectrum of the FWM and the filtered data and clock signals. Detuning between the data and clock wavelength is about 5.9 nm. Resolution bandwidth is 0.1 nm.

In the co-propagation scheme, each individual pulse (clock or data) causes fast absorption saturation inside the EAM followed by a slower absorption recovery, hence, affecting the transmitted power of the next incoming co-propagating pulse (data or clock) based on its delay in arrival. Fig. 6.9.a shows the error signal when the feedback loop is open (unlock) and the VCO frequency is set to (10GHz+10KHz). The repetition period of the error signal is (12.5 μsec) corresponding to (10x8 KHz) difference in repetition frequency between data (80Gbit/s) and clock (10GHz). The estimated sensitivity of the steep slope is about 30 mVolt/ps.

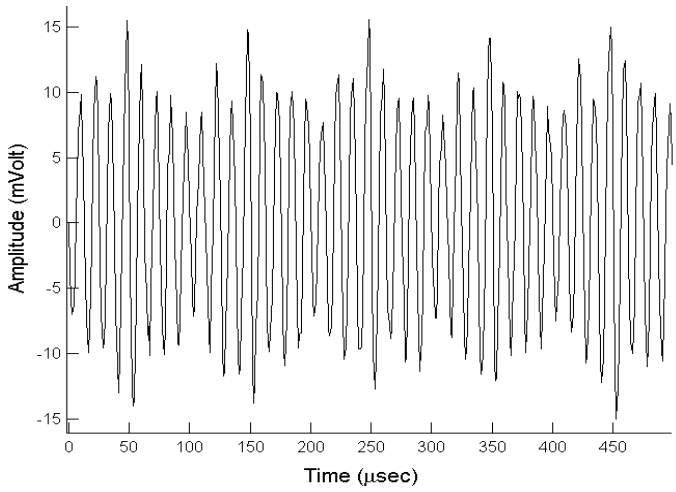

(a)

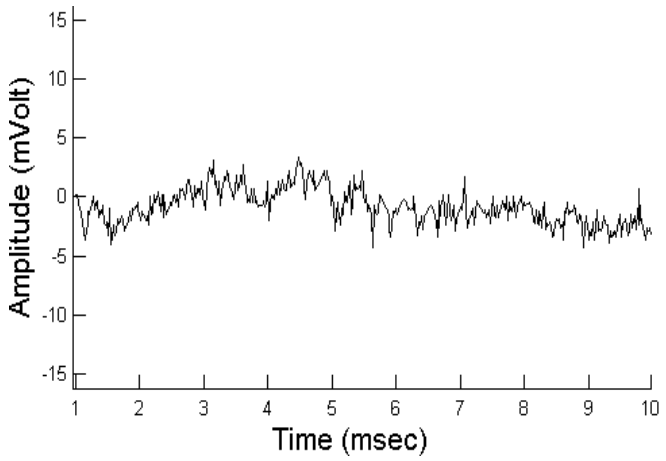

(b)

Fig. 6.9: (a) The measured error signal during unlock. (b) The error signal after locking.

Fig. 6.9.b shows the error signal after locking. Compared to the unlocked case, it is almost a DC voltage with some fluctuations corresponding to timing jitter between the data and clock pulses. Fig. 6.10.a shows the RF spectrum of the recovered clock

with a center frequency of 10 GHz. The timing jitter is calculated from the clock RF spectrum by integrating over the phase-noise pedestal. It yields an r.m.s. timing jitter ≤ 350 fs. Fig. 6.10.b shows the recovered 10GHz optical clock pulses on a sampling oscilloscope using a 45 GHz photo-detector. The ringings are due to the detector response.

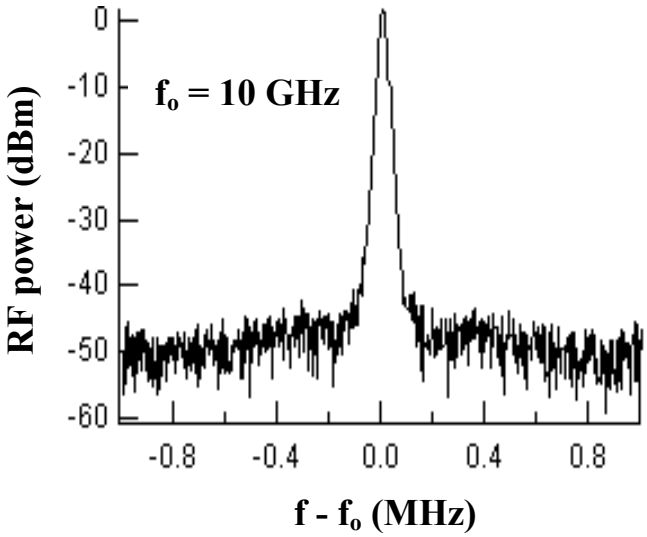

(a)

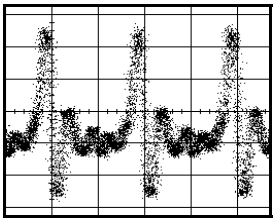

50 ps/div

(b)

Fig. 6.10: (a) The RF spectrum of the recovered clock. (b) The recovered clock as measured in the time domain.

Another amplifier stage with a BPF is used to display the 10 Gbit/s demultiplexed channel on a sampling oscilloscope. Fig. 6.11 shows the 10 Gbit/s FWM demultiplexed eye diagram from 80 Gbit/s. The eye is displayed on the optical channel of the oscilloscope with a built-in SONET/SDH low-pass electrical filter with a bandwidth of 7.465 GHz. The oscilloscope histogram statistics were used to estimate the quality factor (Q) of the demultiplexed channel. The Q^2 factor measured from the eye diagram is about 14.8 dB, and the calculated BER based on this Q factor, assuming a Gaussian noise distribution, is 1.8×10^{-8}.

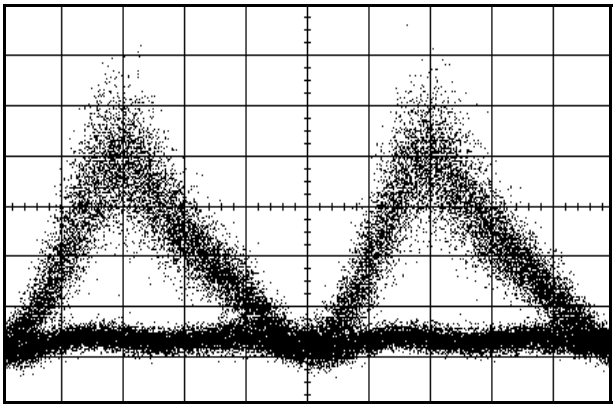

20 ps/div.

Fig. 6.11: The eye diagram of the 10 Gbit/s demultiplexed channel using 7.465 GHz optical channel of a sampling oscilloscope.

The simultaneous clock recovery and FWM in this experiment is achieved at 2 volts reverse bias of EAM. Fig. 6.12 shows the effect of reverse bias on the error signal steep slope. The reverse bias increases the slope sensitivity of the error signal as the

cross-absorption modulation enhances inside EAM. We noted also an increase in the FWM eye amplitude with reverse bias. Fig. 6.12 illustrates the increase in the eye amplitude normalized to the amplitude at zero bias. One reason for this amplitude increase is the EAM band-edge shift to longer wavelength with more reverse bias, resulting in more absorption of the clock and data power in EAM before the first EDFA input and thus allows more gain for the FWM signal. Another reason is the FWM power enhancement at the EAM output by 1.5 dB at 2-volt reverse bias, which improves the OSNR of the demultiplexed channel, as indicated in Fig. 6.7.

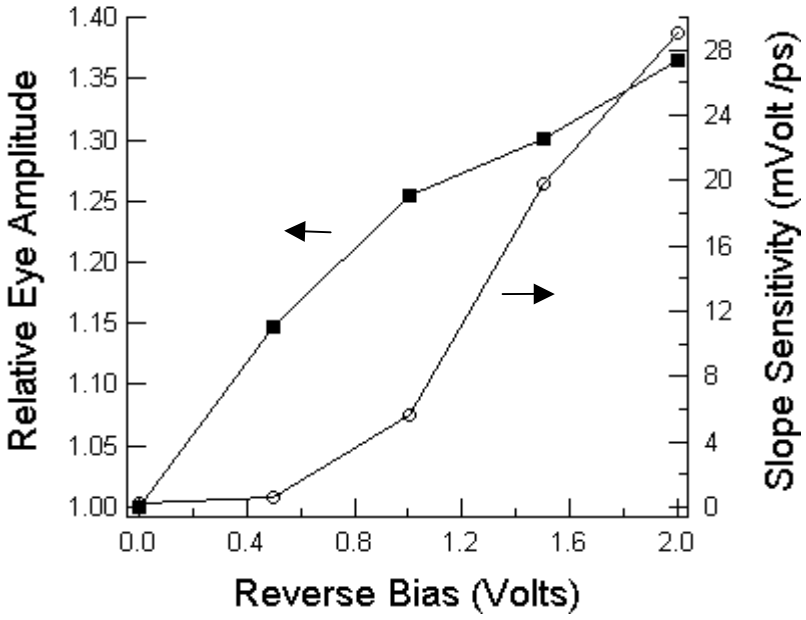

Fig. 6.12: The measured slope sensitivity of the error signal and the relative FWM eye diagram amplitude versus EAM reverse bias.

In summary, we have demonstrated a new ultra-fast technique using simultaneous FWM and timing extraction inside a single EAM, which allows high-speed optical demultiplexing and clock recovery at 80 Gbit/s. We also investigated the enhancement of the FWM signal and the error signal slope with higher reverse biases.

Chapter 7

Discussion & future work

We have discussed all-optical nonlinear effects inside semiconductor optical waveguides (EAM & SOA) and its applications for ultra-fast optical signal processing. We have also demonstrated all-optical cross-modulation technique in EAM and the wavelength dependence of its transmission. The switching window of the EAM depends on both the reverse bias and input power and it can be significantly shorter than that of the SOA. In addition, we have demonstrated how the nonlinear transmission of the EAM can be used as an all-optical logic AND gate and its capability to work at high-speeds with more than 10 dB of contrast ratio.

We have developed a new technique for optical digital signal processing using nonlinear optical semiconductor wave-guides. The technique is based on the nonlinear time-dependent transmission saturation. This technique has been used for all-optical timing extraction, which in turn is used to perform optical clock recovery. The all-optical extraction can resolve timing delay between clock and data pulses less than a picosecond. The clock recovery has been experimentally demonstrated up to 160 Gbit/s, using 2^{31}-1 long PRBS data. The simulation results show that our timing extraction technique using EAM for sub-clock recovery can be applied to data rates up to 640 Gbit/s. Unlike other techniques, this technique doesn't require high-speed photo-detectors [4], and it is bit-rate flexible.

We have demonstrated optical time demultiplexing with simultaneous clock recovery using a single EAM at 40 Gbit/s. The system showed an error free operation and a small timing jitter for the recovered clock, less than 200 fs. The bit-error-ratio measurement of the demultiplexed channel at 10 Gbit/s (2^{31}-1 PRBS) showed an error free operation with a 3.2 dB power penalty. The system was also tested as a receiver in a recirculating loop transmission experiment. The burst-mode data was running at 40 Gbit/s and it has a 2^{23}-1 long PRBS bit-pattern. The data propagates for 10,000 Km of transmission distance. The duration of a one data packet is about 500 μsec with about 100-μsec rise and fall time. The system shows a successful optical demultiplexing to 10 Gbit/s burst-mode data with a simultaneous optical clock recovery at 10 GHz. The estimated BER of the received data was about 10^{-7}.

The 3R regeneration has been demonstrated using a single EAM at 10 Gbit/s. The nonlinearity of the EAM transmission allows for re-shaping of the degraded input data stream. The recovered clock is amplified and used for re-timing. The optical 3R regeneration was performed using 2^{31}-1 long PRBS.

For future work, one of the critical issues in clock recovery scheme is the choice of low pass filter bandwidth. The low pass filter averages over the amplitude fluctuations of the data that could be due to pattern dependence, and the fluctuations in average power due to random distribution of ones and zeros along the bit pattern. The latter is a more significant problem and it places a limit on the low pass filter bandwidth

and the clock acquisition time. For example, in the experiment a 15 KHz bandwidth LPF gave 80 μsec transient time, while a 100 KHz bandwidth filter gave 40 μsec, and a 1 MHz bandwidth LPF gave about 10 μsec. Although, a low pass filter with small bandwidth may reduce the bit-pattern effects, choosing a larger bandwidth can reduce the acquisition time, and increases the ability of the system to track more phase noise in order to correct it. One solution to get short acquisition time while reducing the bit-pattern dependence is to use large bandwidth LPF and normalize the feedback error signal with the fluctuating input power of the data stream, which can be obtained by using an external photo-detector with an appropriate bandwidth. Because the photo-detected power of the input data depends on the pulses peak power and the bit pattern, we believe the normalized error signal will eliminate the dependence on the bit pattern, and at the same time the large bandwidth of the LPF will allow a faster transient time response.

For the 3R regeneration, considering higher bit rates such as 20Gbit/s and 40Gbit/s is important. The EAM has already shown to have a good performance for demultiplexing at 40 Gbit/s. Although at these bit rates it may require higher data input power to achieve the same nonlinear transmission characteristic as already shown in chapter 5.

As demonstrated in chapter 6, the FWM in EAM depends on the reverse bias and wavelength detuning between the pump and probe. The FWM efficiency behaves completely different from that of SOA. For future work, more experimental

investigation on the FWM effect in EAM will be needed in order to better understand the physical mechanisms involved and their interactions. Also, numerical modelling of the FWM effect in EAM in the future work will provide valuable insights to these different effects and provide predictions on the limitations of the FWM in EAM for ultra-fast optical signal processing.

APPENDIX A

Optical clock recovery model

The following is the Matlab simulation code for optical clock recovery system using EAM or SOA:

```
clear all;
pack
clk=clock
%---------------------------------Initialization of different variables--------------------------
N=1000000;                  % Simulation run time in ps
Points=round(4*0.2/0.3);    %(number of device sections = refractive index * device
                            length / light speed)
To1=100;                    % clock repetition period in ps
To2=6.25;                   % Data repetition period in ps
aa=0.01;                    %Data amplitude in watts
pulsewidth=2;               % Pulse FWHM in ps
Pplus=zeros(1,Points);      %Input clock forward propagation in space
Pminus=zeros(1,Points);     %Input data backward propagation in space
Poutplus=zeros(1,N+Points);  %Output data backward propagation in space
Poutminus=zeros(1,N+Points); %Output clock forward propagation in space
s1=zeros(1,N+Points);       % First low pass filter output
```

```
s2=zeros(1,N+Points);          % Second low pass filter output
dif=zeros(1,N+Points);         % Error signal
dT=zeros(1,N+Points);          %Difference between data and clock repetition periods
dt=zeros(1,N+Points);          %Delay between data and clock pulses in time in ps
taw=70000;                     %Low pass filter time constant
dT(2)=0.01;
dt(2)=1;
Ge=1e-3;                       % Feedback gain
v=-2;                          %EAM reverse bias voltage in volts

%--------------------------------------PRBS generation-------------------------------------------
m=7;                           % 2^m-1 PRBS
Tp=m*(2^m-1)*To2;              %PRBS repetition period
D=2^m-1;
switch m
case {7,15}
   bb=m-1;
case {10,20}
   bb=m-3;
case 23
   bb=18;
otherwise
   bb=28;   % m=31
```

```
end
y=bitget(D,m:-1:1);
for r=1:2^m-2
D=bitor(xor(bitget(D,m),bitget(D,bb)),bitshift(D,1,m));  %PRBS generation using XOR
y=[y bitget(D,1:1:m)];
end
clear r;
%-------------------------------------------------------------------------------------
%---------------------------------EAM calibration-----------------------------------
x=10*log10(0.2*1000)-14.815;   %Input average power
k0=[7.715e-008,1.5267e-007,-4.5688e-006,-1.7827e-005,5.7436e-006];
k1=[1.377e-005,0.00019336,0.0009887,0.0023412,0.0031067];
k2=[0.00034983,0.0057732,0.034654,0.090146,0.098493];
k3=[0.00088404,0.02165,0.17089,0.53528,0.64851];
k4=[-0.032769,-0.48843,-2.5801,-5.6382,-4.0244];
k5=[0.6273,10.431,63.412,169.69,184.92];
k=[k0;k1;k2;k3;k4;k5]*[v^4;v^3;v^2;v;1];
tau=k'*[x^5;x^4;x^3;x^2;x;1];          % EAM Recovery time from empirical data. In
                                              case of SOA it is set to 100ps.
g0=0.0086347*v^5+0.12429*v^4+0.57521*v^3+0.87699*v^2+1.5146*v-2.3103;
   %The loss coefficient of EAM from empirical data. In case of SOA it is set to 2.
g=(g0/Points)*ones(1,Points);          % Loss/gain per section
geq=g;                                 %Unsaturated loss/gain coefficient.
```

```
G=exp(g);                          %Initial  loss/gain distribution in space
%-------------------------------------------------------------------------------------------

for t=2:N+Points
        Poutplus(t)=0.2.*Pplus(Points);
        Poutminus(t)=0.2.*Pminus(1);
        GG=G-(G-1).*exp((-Pplus-Pminus)./0.9715);
        Gnew=G./(GG+eps);
        a=Pplus./(Pplus+Pminus+eps);
        b=Pminus./(Pplus+Pminus+eps);
        Pplus=Pplus+log(GG+eps).*a;
        Pminus=Pminus+log(GG+eps).*b;
        g=log(Gnew); g=g+(geq-g)/tau;        G=exp(g);
        Pplus(2:Points)=Pplus(1:Points-1);
        Pminus(1:Points-1)=Pminus(2:Points);
        Pminus(Points)=(0.2*3/1.1).*exp(-(1.68.*(rem(t,To1-dT(2))-(To1-
                        dt(t))/2)/pulsewidth).^2);  %Gaussian clock pulses generation
        Pplus(1)=(aa*3/1.1).*exp(-(1.68.*(rem(t,To2)-To2/2)/pulsewidth).^2).*y(ceil((t-
                fix((t-1)/(Tp-1))*(Tp-1))/To2)); %Gaussian data pulses generation
        s1(t)=s1(t-1)+Poutminus(t)-s1(t-1)/taw;
        s2(t)=s2(t-1)+Poutplus(t)-s2(t-1)/taw;
        dif(t)=s2(t)-s1(t);
        dt(t+1)=dt(t)+Ge*dif(t);        %Feedback signal to change the clock delay
```

```
end
plot(Poutminus,'r');     % clock
figure;
plot(Poutplus);          %Data
figure;
plot(s1);
figure;
plot(s2);
figure;
plot(dif);
figure;
plot(dt);
clk=etime(clock,clk)/60          %Model run time
```

APPENDIX B

Measuring the timing jitter

In this appendix we discuss a technique for measuring timing jitter of a pulse train using the RF power spectrum [32][49]. Timing jitter is defined as random fluctuations in the pulse repetition period. The pulse train spectrum consists of a δ-function like frequency components at integral multiples 'n' of the pulse repetition rate, with each peak resting on double-sided noise bands. These noise bands are due to amplitude noise and phase noise in the pulse train. The ratio of the area under a noise band to the area under the carrier peak increases by n^2 for phase noise case as we go to higher order harmonics [49].

The root mean square (r.m.s) timing jitter can be obtained from the ratio of the integrated power in the double-sided phase noise band 'P_{sb}' to the power in the carrier 'P_c' based on the following formula:

$$\text{R.M.S.} \quad \text{Timing jitter} = \frac{1}{2\pi\, n\, f_o} \sqrt{\frac{2}{P_c} \int_{nf_o+f_{low}}^{nf_o+f_{high}} \frac{P_{sb}(f)}{B} df} \qquad (18)$$

Where f_o is the pulse train repetition rate, 'B' is the spectrum resolution bandwidth, f_{low} is the starting frequency of the noise band, and f_{high} is the stop frequency of the noise band.

The following formula is a simple form of eq. (18) that can be used to estimate the r.m.s timing jitter from the RF spectrum:

$$\text{R.M.S.} \quad \text{Timing jitter} = \frac{1}{2\pi\, n\, f_o} \sqrt{\frac{P_{sb}}{P_c} \frac{\Delta f}{B}}$$

Where Δf is the full-width at half maximum of the double-sided noise band. Fig. B.1 shows an example of the RF spectrum for a 10 GHz pulse train.

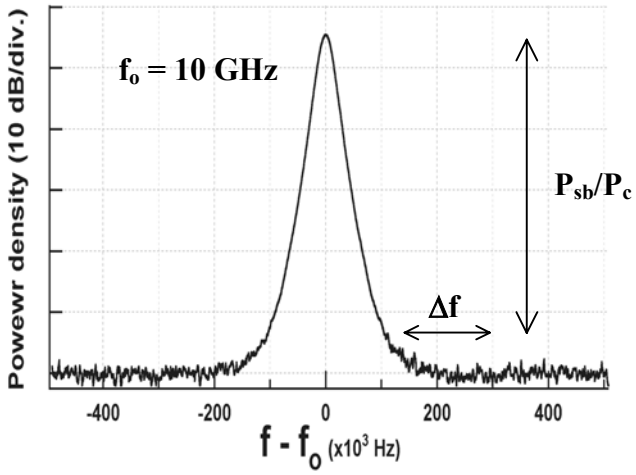

Fig. B.1: The RF spectrum of a 10 GHz pulse train.

REFERENCES

[1] G. Keiser, "Optical fiber communications," second edition, McGraw-Hill,Inc. 1989.

[2] M. Saruwatari, "All-optical signal processing for Terabit/Second optical transmission," IEEE J. Select. Topics Quantum Eelectron. , vol. 6, no. 6, pp. 1363-1374, Nov./Dec. 2000.

[3] B. Razavi, "Monolithic phase-locked loops and clock recovery circuits, theory and design," IEEE press, 1996.

[4] I. D. Phillips, A. D. Ellis, T. Widdowson, D. Nesset, A. E. Kelly, "80 Gbit/s optical clock recovery using an electrical phase locked loop, and commercially available components," OFC 2000,ThP4-1, pp. 229-231, 2000.

[5] T. Yamamoto, L. K. Oxenlowe, C. Schmidt, C. Schubert, E. Hilliger, U. Feiste, J. Berger, R. Ludwig, and H. G. Weber, "Clock recovery from 160Gbit/s data signals using phase-locked loop with interferometric optical switch based on semiconductor optical amplifier," Electron. Lett. 37, pp. 509 – 510, 2001.

[6] D.T.K. Tong, Kung-Li Deng, B. Mikkelsen, G. Raybon, K. F. Dreyer, and J. E. Johnson, "160Gbit/s clock recovery using electroabsorption modulator-based phase locked loop," Electron. Lett. 26, pp.1951 – 1952, 2000.

[7] J. Hansryd, P.A. Andrekson, and B. Bakhshi, "A simple, low timing jitter, sub-multiple clock recovery technique," ECOC'98, pp. 471-472, 1998.

[8] M. Jinno, and T. Mastsumoto, "Optical tank circuits used for all-optical timing recovery," IEEE J. Quantum Electron., vol. 28, pp. 895-900, Apr. 1992.

[9] B. Sartorius, C. Bornholdt, O. Brox, H. J. Ehrke, D. Hoffmann, R. Ludwig, and M. Mohrle, "All-optical clock recovery module based on self-pulsating DFB laser," Electron. Lett., vol. 34, pp. 1664-1665, 1998.

[10] Tong Wang, Zhihong Li, Caiyun Lou, Yue Wu, and Yizhi Gao, "Comb-like filter preprocessing to reduce the pattern effect in the clock recovery based on SOA," IEEE Photon. Technol. Lett. Vol. 14, no. 6, pp. 855-857, June 2002.

[11] K. J. Blow, N. J. Doran, and B. P. Nelson, "Demonstration of the non-linear fiber loop mirror as an ultrafast all-optical demultiplexer," Electron. Lett., vol. 26, pp. 962-964, 1990.

[12] M. Eiselt, W. Pieper, and H. G. Weber, "All-optical high speed demultiplexing with a semiconductor laser amplifier in a loop mirror configuration," Electron. Lett., vol. 29, pp. 1167-1168, 1993.

[13] M. Vaa, B. Mikkelsen, K.S. Jepsen, K.E. Stubkjaer, R. Hess, M. Duelk, W. Vogt, E. Gamper, E. Gini, P.A. Besse, H. Melchior, S. Bouchoule, "Bit error rate assessment of 80 Gbit/s all-optical demultiplexing by a monolithically integrated Mach-Zehnder interferometer with semiconductor optical amplifiers," Integrated Optics and Optical Fiber Communications, 11th International Conference on, and 23rd European Conference on Optical Communications, Vol. 3 , pp. 31 –34, 22-25 Sept. 1997.

[14] S. Hojfeldt, S. Bischoff, J. Mork, "All-optical demultiplexing using an electroabsorption modulator," Lasers and Electro-Optics, 2000. (CLEO 2000) , pp. 342 -343, 7-12 May 2000.

[15] S.L. Jansen, M. Heid, S. Spalter, E. Meissner, C.-J. Weiske, A. Schopflin, D. Khoe, H. De Waardt, "Demultiplexing 160 Gbit/s OTDM signal to 40 Gbit/s by FWM in SOA," Electron. Lett. 38, pp. 978-980, 2002.

[16] P. S. Cho, D. Mahgerefteh, J. Goldhar, "All-optical 2R regeneration and wavelength conversion at 20 Gbit/s using an electroabsorption modulator," IEEE Photon. Technol. Lett. 11, no. 12, pp. 1662-1664, 1999.

[17] T. Otani, M. Suzuki, and S. Yamamoto, "40 Gbit/s optical 3R regenerator for all-optical networks," ECOC 2001, We.F.2.1, pp. 278-281, 2001.

[18] B. Lavigne, O. Leclerc, P. Brindel, D. Chiaroni, B. Dany, P. Guerber, D. Rouvillain, A.J. Alcatel, "All-optical 3R regeneration," Lasers and Electro-Optics Society 2000 Annual Meeting. LEOS 2000. 13th Annual Meeting. IEEE, Vol. 2 , pp. 407-408, 3-16, Nov.2000.

[19] Hsiao-Yun Yu, " High-bit-rate optical signal processing using nonlinear effects in semiconductor optical amplifiers," Thesis dissertation, University of Maryland, College Park, 1999.

[20] Paul V. Petruzzi, " Optical pattern recognition using a segmented semiconductor optical amplifier," Thesis dissertation, University of Maryland, College Park, 2003.

[21] G. Pham, J. Felsemberg, L. Lievre, D. Mousseaux, A. Tournereau, J. N. Reygrobellet, D. Keller, C. Porcheron, P. Piatti, M. Renaud and J. L . Nicque, "High performance semiconductor optical amplifier industrial module," ECOC 2003, We4.P.87, 2003.

[22] M. Suzuki, H. Tanaka, N. Edagawa, K. Utaka, and Y. Matsushima, “Transform-limited optical pulse generation up to 20 GHz repetition rate by a sinusoidally driven InGaAsP electroabsorption modulator”, J. Lightwave Technol. 11, pp. 468-473, 1993.

[23] S. Kodama, T. Ito, N. Watanabe, S. Kondo, H. Takeuchi, H. Ito, T. Ishibashi,“200 Gbit/s monolithic photodiode-electroabsorption modulator (PD-EAM) optical gate,” Device Research Conference, 2001, pp. 25-27, June 2001.

[24] D.D. Marcenac, A.D. Ellis, D.G. Moodie,”80 Gbit/s using electroabsorption modulators,” Integrated Optics and Optical Fiber Communications, 11th International Conference on, and 23rd European Conference on Optical Communications (Conf. Publ. No.: 448) , Vol 3 , 22-25 Sept, pp. 23-26, 1997.

[25] T. Wood, J. Pastalan, A. Burrus, B. Johnson, B. Miller, J. DeMiguel, U. Koren, and M. Young, “ Electric field screening by photo-generated holes in multiple quantum wells: A new mechanism for absorption saturation”, Appl. Phys. Lett., vol. 57, no. 11, pp. 1081-1083, Sept. 1990.

[26] J.feldmann, K. Goossen, D. A. B. Miller, A. Fox, J. Cunningham, and W. Yan, “ Fast escape of photocreated carriers out of shallow quantum well”, Appl. Phys. Lett., vol.59, no. 1, pp. 66-68, July 1991.

[27] Sune Hojfeldt, Svend Bischoff, and jesper Mork, “All-optical wavelength conversion and signal regeneration using an electroabsorption modulator”, J. Light Wave Tech., vol. 18, no. 8, pp. 1121-1127, Aug. 2000.

[28] K. Shimomura, K. Shimizu, K. Ishida, T. Sugihara, and Y. Kobayashi, “A simple optical demultiplexing method using saturable absorption of EA

modulator", presented at ECOC 2000 conference, Munich, Germeny, Sept. 3-7, 2000.

[29] T. Otani, T. Miyazaki, and S. Yamamoto, "40 Gbit/s optical 3R regenerator using electroabsorption modulators for high-speed optical networks", presented at NFOEC 2000 conference, Denver, Colorado, August 27-31, 2000.

[30] N. Edagawa, M. Suzuki, and S. Yamamoto, "Novel wavelength converter using an electroabsorption modulator: Conversion experiments at up to 40 Gbit/s", in Proc. Tech. Dig. OFC '97, vol. 6, pp. 77-78, 1997.

[31] Masaki Kato, and Yoshiaki Nakano, " Proposal of a novel wavelength converter using photo-induced refractive index change in multiple-quantum-well electro-absorption modulators", presented at optical amplifiers and their applications and integrated photonics research conference, Quebec, Canada, July 2000.

[32] U. Keller, K. D. Li, M. Rodwell, D. M. Bloom, "Noise characterization of femtosecond fiber Raman soliton lasers," IEEE J. Quantum Electron. , vol. 25, no. 3, pp. 280-288, March 1989.

[33] A.E. Siegman, "Lasers," University Science Books, 1986.

[34] R. E. Best, "Phase-locked loops," McGraw-Hill, Fifth edition, 2003.

[35] I. D. Phillips, A. Gloag, D. G. Moodie, N. J. Doran, I. Bennion, A. D. Ellis, "Simultaneous demultiplexing and clock recovery using a single electroabsorption modulator in a novel bi-directional configuration," optics communications (150), pp.101-105, May 1998.

[36] A. D. Ellis, D. M. Spirit, "Compact 40 Gbit/s optical demultiplexer using a GaInAsP optical amplifier," Electron. Lett. 29, no. 24, pp. 2115-2116, 1993.

[37] G. Aubin, T. Montalant, J. Moulu, F. Pirio, J. B. Thomine, F. Devaux, "40 Gbit/s OTDM soliton transmission over transoceanic distances," Electron. Lett. 32, no. 24, pp. 2188-2189, 1996.

[38] E. Jahn, N. Agrawal, H. J. Ehrke, R. Ludwig, W. Pieper, H. G. Weber, "Monolithically integrated asymmetric Mach-Zehnder interferometer as a 20 Gbit/s all-optical add/drop multiplexer for OTDM systems," Electron. Lett. 32, no. 3, pp. 216-217, 1996.

[39] B. Lavigne, P. Guerber, P. Brindel, E. Balmefrezol, B. Dagens, "Cascade of 100 optical 3R regenerators at 40Gbit/s based on all-active Mach Zehnder interferometer," ECOC'01, We.F.2.6, pp. 290-291, 2001.

[40] T. Otani, T. Miyazaki, and S. Yamamoto, "20 Gbit/s optical regenerator using electroabsorption modulators for all-optical network application," ECOC'99, I 250-251, 1999.

[41] J. C. Simon, L. Billes, A. Dupas, L. Bramerie, "All optical regeneration techniques," ECOC'99, II 256 – 259, 1999.

[42] N. Edagawa, M. Suzuki, "Novel all optical limiter using electroabsorption modulators," OFC'00, ThP1, pp. 220-222, 2000.

[43] B. Sartorious, C. Bornholdt, O. Brox, U. Feiste, and M. Mohrle, "Towards the all-optical 3R regenerator: Performance of the optical clock," ECOC'99, II 264-265, 1999.

[44] S. Diez, C. Schmidt, R. Ludwig, H. G. Weber, K. Obermann, S. Kindt, I. Koltchanov, K. Petermann, "Four-Wave Mixing in Semiconductor Optical

Amplifiers for Frequency Conversion and Fast Optical Switching," IEEE J. Select. Topics Quantum Eelectron. , Vol. 3, no. 5, pp. 1131-1145, Oct. 1997.

[45] J. Zhou; N. Park, J.W. Dawson, K.J. Vahala, M.A. Newkirk, B.I. Miller, "Efficiency of broadband four-wave mixing wavelength conversion using semiconductor traveling-wave amplifiers," IEEE Photon. Technol. Lett. 6, pp. 50-52, 1994.

[46] G. P. Agrawal, "Population pulsations and nondegenerate four-wave mixing in semiconductor lasers and amplifiers," J. Opt. Soc. Am. B, vol. 5, pp. 147-158, 1988.

[47] S. Diez, R. Ludwig, C. Schmidt, U. Feiste, H.G. Weber,"160-Gb/s optical sampling by gain-transparent four-wave mixing in a semiconductor optical amplifier," IEEE Photon. Technol. Lett. 11, pp. 1402-1404, 1999.

[48] R. Calvani, F. Cistemino,R. Girardi,E.Riccardi, "Ultra-stable polarization independent all-optical demultiplexer using four wave mixing in a dispersion shifted fiber," OFC /IOOC'99 4, pp. 138-140, 1999.

[49] A.J. Taylor, J.M. Wiesenfeld, G. Eisenstein, R.S. Tucker, "Timing jitter in mode-locked and gain-switched InGaAsP injection lasers," Appl. Phys. Lett. 49 (12), pp. 681-683, Sept. 1986.